



**HAL**  
open science

# Quasi-in-situ detection of nanoparticles by laser-induced incandescence during chemical vapor deposition synthesis of carbon nanotubes

Yiguo Xu

► **To cite this version:**

Yiguo Xu. Quasi-in-situ detection of nanoparticles by laser-induced incandescence during chemical vapor deposition synthesis of carbon nanotubes. Other. Université Paris Saclay (COMUE), 2018. English. NNT: 2018SACL070 . tel-02021233

**HAL Id: tel-02021233**

**<https://theses.hal.science/tel-02021233v1>**

Submitted on 15 Feb 2019

**HAL** is a multi-disciplinary open access archive for the deposit and dissemination of scientific research documents, whether they are published or not. The documents may come from teaching and research institutions in France or abroad, or from public or private research centers.

L'archive ouverte pluridisciplinaire **HAL**, est destinée au dépôt et à la diffusion de documents scientifiques de niveau recherche, publiés ou non, émanant des établissements d'enseignement et de recherche français ou étrangers, des laboratoires publics ou privés.

# *Quasi-in-situ* detection of nanoparticles by laser-induced incandescence during the chemical vapor deposition synthesis of carbon nanotubes

Thèse de doctorat de l'Université Paris-Saclay  
préparée à CentraleSupélec

Ecole doctorale n°579 SMEMAG  
Spécialité de doctorat: Science des Matériaux

Thèse présentée et soutenue à Gif-sur-Yvette, le 13 Nov. 2018, par

**YIGUO XU**

Composition du Jury :

Brigitte TRETOUT Professeur, Office National d'Études et de Recherches Aérospatiales	Président
Christophe BICHARA Professeur, Aix-Marseille University	Rapporteur
Pascale DESGROUX Professeur, Université Lille	Rapporteur
Laurent ZIMMER Professeur, CentraleSupélec	Examineur
Anthony DICHIARA Professeur, University of Washington	Examineur
Delong HE Professeur, CentraleSupélec	Invité
Jinbo BAI Professeur, CentraleSupélec	Directeur de thèse

*Quasi-in-situ* detection of nanoparticles by  
laser-induced incandescence during chemical  
vapor deposition synthesis of carbon nanotubes

by

Yiguo Xu

Laboratoire de Mécanique des Sols, Structures et Matériaux  
CentraleSupélec, Université Paris-Saclay

Dissertation in partial fulfillment of the requirements submitted for  
the degree of Doctor of Philosophy  
in CentraleSupélec, Université Paris-Saclay  
2018

Copyright © 2018 by Yiguo Xu  
All rights reserved

# Acknowledgements

First, I would like to express my sincere gratitude to my supervisors Prof. Jinbo Bai and Prof. Laurent Zimmer for giving me the opportunity to carry out my doctoral research, and their continuous support of my PhD study. I am deeply impressed by their hard-working spirit, serious attitude towards research, which are invaluable in my future life. It is a great challenge for me to complete my thesis. I learned a lot from their constant encouragement, guidance and suggestions. It would not have been possible to finish my thesis without their support. Special gratitude is also extended to Delong He, Anthony Dichiara and Yang Ma. I was completely unfamiliar with my doctoral project three years ago. They always had the patience to teach me to use different equipments and solve the numerous issues. Every discussion with them was of benefit to me.

Then I would also like to thank the members of the jury: Christophe Bichara, Pascale Desgroux, Brigitte Tretout, Laurent Zimmer, and Anthony Dichiara. It was my honor and a great pleasure to receive their valuable comments and suggestions, which are very helpful for me to improve my thesis.

Meanwhile, I would like to acknowledge the financial support from China Scholarship Council (CSC), the MATMECA consortium and the ANR under contract number ANR-10-EQPX-37 in the past three years.

I would also like to thank the engineers who have helped me to do the measurements: Mr. Gilbert Le Gal for fabricating the special-designed CVD

reactor, Mr. Thomas Reiss and Ms. Nathalie Ruscassier for SEM observations, Mr. Paul Haghi-Ashtiani for TEM observations, and Ms. Pascale Gemeiner for Raman analyse. I am also indebted to Ms. Farida Djebbari, Ms. Sokona Konate, Mr. Eric Perrin et al. for their assistances.

I also owe my sincere gratitude to my colleagues and friends. It was a pleasure working with you. Studying in CentraleSupélec is a precious experience in my life.

Last but not the least, I would like to thank my beloved parents for giving birth to me and for supporting me spiritually all the times. I hope that I can spend more time with them in the future.

# Abstract

Controlling the formation of iron-based catalyst nanoparticles is highly desired to synthesize carbon nanotubes (CNTs) with well-defined structures and properties at a large scale. However, it remains a big challenge. This work contributes to the *quasi-in-situ* detection of nanoparticles by laser induced incandescence (LII) technique during the floating catalytic chemical vapor deposition (FCCVD) synthesis of CNTs.

First, high resolution transmission electron microscopy (TEM) was used to characterize the nanoparticle nature and size. The theoretical LII signal was simulated by considering the nanoparticle density, heat capacity and size distribution, etc. A detailed sensitivity and uncertainty of the key parameters on the evaluated particle size for this model was estimated. The LII model was validated by a comparison of the evaluated results with the ones obtained by TEM measurements. Then, the developed LII technique combined with TEM was applied to investigate the evolution of nanoparticles in the gas phase along the reactor axis. The influence of the temperature, ferrocene concentration, carbon source and hydrogen ratio on the nanoparticle size was also demonstrated. Finally, the roles of nanoparticles in the gas phase during CNT synthesis process were discussed by correlating information on the axial nanoparticle evolution and the morphology of CNTs synthesized on the substrate along the reactor axis. And a model based on the thermodynamics of the nanoparticle nucle-

ation was proposed to describe the nanoparticle formation process during the FCCVD process. It is found that the as-formed nanoparticles in the gas phase exhibit core-shell structures with an  $\alpha$ -Fe core and a carbon shell. Hence iron nanoparticles in the gas phase could not contribute to the CNT growth on the substrate because of the carbon encapsulation. Meanwhile the evaluated size of nanoparticles by LII is in good agreement with the TEM determined one. This study, showing potential relations between the floating nanoparticles and the CNTs on the substrate, reveals the important LII application prospect to understand and to improve the FCCVD process.

# Résumé

Le contrôle de la formation de catalyseur de nanoparticules à base de fer est hautement souhaitait synthétiser des nanotubes de carbone (NTCs) avec des structures bien définies et propriétés à grande échelle. Cependant, cela reste un grand défi. Ce travail contribue à la *quasi-in-situ* détection des nanoparticules par la technique d'incandescence induite par laser (LII) pendant le dépôt chimique en phase vapeur avec catalyseur flottant (FCCVD) de NTCs.

Premièrement, la microscopie électronique en transmission (MET) à haute résolution était utilisé pour caractériser la nature et la taille des nanoparticules. Le signal théorique de LII a été simulé en considérant la densité des nanoparticules, la capacité thermique et la distribution de taille, etc. La sensibilité et l'incertitude concrètes des paramètres clés sur la taille évaluée des particules pour ce modèle ont été estimées. Le modèle LII a été validé par la comparaison des résultats évalués avec ceux obtenus par la MET. Ensuite, la technique mature LII combinée avec MET a été appliquée pour étudier l'évolution des nanoparticules dans la phase gazeuse le long de l'axe du réacteur. L'influence de la température, de la concentration de ferrocène, de la source de carbone et de la proportion hydrogène sur la taille des nanoparticules a également été démontrée. Enfin, les rôles des nanoparticules dans la phase gazeuse au cours du processus de synthèse des NTC ont été discutés en corrélant les informations sur l'évolution axiale des nanoparticules et la morphologie des NTC synthétisés

sur le substrat le long de l'axe du réacteur. Un modèle basé sur la thermodynamique de la nucléation des nanoparticules a été proposé pour décrire le processus de formation des nanoparticules au cours du processus DCVCF. Il est constaté que les nanoparticules as-formé en phase gazeuse présentent des structures coeur-coquille avec un noyau de  $\alpha$ -Fe et la coque de carbone. Ainsi, les nanoparticules de fer en phase gazeuse ne pourraient pas contribuer à la croissance de NTC sur le substrat à cause de l'encapsulation de carbone. En même temps, la taille des nanoparticules évaluée par LII est en bon accord avec celle-ci déterminée par MET. Cette étude, montrant les relations potentielles entre les nanoparticules flottantes et les NTCs sur le substrat, révèle une perspective importante de l'application de LII pour comprendre et améliorer le processus DCVCF.

# Abbreviations and Symbols

## ABBREVIATIONS

<b>AFM</b>	Atomic Force Microscope
<b>ANOVA</b>	Analysis of Variance
<b>CFD</b>	Computational Fluid Dynamics
<b>CNTs</b>	Carbon Nanotubes
<b>CVD</b>	Chemical Vapor Deposition
<b>DFT</b>	Density Functional Theory
<b>DTG</b>	Differential Thermal Analysis
<b>DWNTs</b>	Double-walled Carbon Nanotubes
<b>EDS</b>	Energy-dispersive X-ray spectroscopy
<b>FCCVD</b>	Floating Catalyst Chemical Vapor Deposition
<b>HAADF</b>	High Angle Annular Dark Field
<b>HiPCO</b>	High Pressure CO Disproportionation
<b>LII</b>	Laser Induced Incandescence
<b>LIF</b>	Laser Induced Fluorescence
<b>MD</b>	Molecular Dynamics
<b>MWNTs</b>	Multi-walled Carbon Nanotubes
<b>PECVD</b>	Plasma-enhanced Chemical Vapor Deposition
<b>PMT</b>	Photomultiplier
<b>SAED</b>	Selective Area Electron Diffraction

<b>SWNTs</b>	Single-walled Carbon Nanotubes
<b>SEM</b>	Scanning Electron Microscopy
<b>STEM</b>	Scanning Transmission Electron Microscope
<b>TAC</b>	Thermal Accommodation Coefficient
<b>TEM</b>	Transmission Electron Microscopy
<b>TGA</b>	Thermogravimetric Analysis
<b>TRLII</b>	Time Resolved Laser Induced Incandescence
<b>VdW</b>	Van der Waals
<b>VLS</b>	Vapor-Liquid-Solid
<b>VSS</b>	Vapor-Solid-Solid
<b>XPS</b>	X-ray Photoelectron Spectroscopy

## SYMBOLS

$c$	Speed of light ( $2.998 \times 10^{10}$ cm/s)
$CMD$	Count Median Diameter (nm)
$c_p$	Heat capacity of nanoparticle ( $\text{kg/m}^3$ )
$c_{p_g}$	Molecular heat capacity of gas (J/gK)
$d$	CNTs diameter
$d_p$	Diameter of nanoparticle (nm)
$E(m)$	Dimensionless refractive index
$F_{\text{gas}}$	Total gas flow rate (L/min )
$h$	Planck constant ( $6.626 \times 10^{-34}$ Js)
$\Delta H_v$	Average enthalpy of formation of sublimed species (J/mol)
$k_B$	Boltzmann constant ( $1.381 \times 10^{-23}$ J/K)
$m_p$	Mass of nanoparticle(g)

$\mu_g$	Average gas molecular weight (g/mol)
$\rho_p$	Density of the nanoparticle (g/cm <sup>3</sup> )
$p_v$	Average partial pressure of sublimed carbon species (bar)
$p_g$	Gas pressure (Pa)
$p_{\text{ref}}$	Reference pressure in Antoine and Clausius-Clapeyron equations (Pa)
$q(t)$	Laser temporal intensity (J/cm <sup>2</sup> )
$q_{\text{abs}}$	Laser energy flux absorbed by nanoparticles (J/s)
$q_{\text{cond}}$	Energy flux during convective heat transfer (J/s)
$q_{\text{rad}}$	Radiation energy flux from the surface of nanoparticles (J/s)
$q_{\text{evap}}$	energy flux from the surface of the nanoparticle during evaporation (J/s)
$J_{\text{evap}}$	mass loss rate form the particle surface in evaporation process (g/s)
$R$	Gas constant (8.3145J/molK)
$R_m$	Gas constant in effective mass units (8.3145×10 <sup>7</sup> gcm <sup>2</sup> molKs <sup>2</sup> )
$R_p$	Gas constant in effective pressure units (83.145barcm <sup>3</sup> /molK)
$S_{\text{LII}}$	LII signal intensity (J/cm <sup>2</sup> )
$S_{\text{BB}}$	LII signal intensity form a blackbody source (J/cm <sup>2</sup> )
$t$	Time (s)
$T_p$	Particle temperature (K)
$T_p^0$	Particle heat-up temperature (K)
$K$	Calibration constant
$Kn$	Knudsen number
$T_{\text{ref}}$	Reference temperature used in Clausius-Clapeyron equation (K)
$T_{\text{BB}}$	Temperature of a blackbody source (K)
$W_v$	Average molecular weight of sublimed carbon species (g/mol)

$\alpha_T$	Thermal accommodation coefficient (TAC)
$\alpha_M$	Mass accommodation coefficient of vaporized carbon clusters
$\gamma$	Heat capacity ratio of the gas
$\varepsilon$	Emission coefficient of nanoparticle
$\lambda_{\text{laser}}$	Laser wavelength (nm)
$\lambda$	Detection wavelength (nm)
$\sigma_{SB}$	Stefan-Boltzmann constant ( $5.6704 \times 10^{-12} \text{W/cm}^2 \text{K}^4$ )
$c_t$	Average thermal velocity of gas molecules (m/s)
$\sigma_g$	Standard deviation in the log-normal function

# Contents

ACKNOWLEDGEMENTS	iii
ABSTRACT	v
RÉSUMÉ	vii
ABBREVIATIONS AND SYMBOLS	ix
1 INTRODUCTION	1
1.1 Motivation . . . . .	1
1.2 CNT synthesis by FCCVD . . . . .	3
1.2.1 CNT history . . . . .	3
1.2.2 CNT properties . . . . .	11
1.2.3 CNT synthesis routes . . . . .	16
1.2.4 CNT growth mechanism in FCCVD . . . . .	20
1.3 Laser-Induced Incandescence . . . . .	33
1.3.1 LII history . . . . .	33
1.3.2 LII model description . . . . .	34
1.4 Conclusion . . . . .	41
2 EXPERIMENTAL PROCEDURE	43
2.1 CNT growth by FCCVD . . . . .	43

2.1.1	Materials . . . . .	43
2.1.2	FCCVD processes . . . . .	44
2.2	Characterization methods . . . . .	48
2.2.1	Electron microscopy . . . . .	49
2.2.2	Thermogravimetric analysis . . . . .	50
2.2.3	Raman spectroscopy . . . . .	51
2.2.4	LII . . . . .	52
2.3	Conclusion . . . . .	55
<b>3</b>	<b>NANOPARTICLES IN THE GAS PHASE</b>	<b>57</b>
3.1	Implementation of LII . . . . .	57
3.1.1	Material properties and key parameters . . . . .	57
3.1.2	Sensitivity and uncertainty analysis . . . . .	63
3.1.3	Comparison of LII and TEM particle-sizing . . . . .	68
3.2	Nanoparticle evolution in the gas phase . . . . .	71
3.2.1	Nanoparticles along the reactor . . . . .	71
3.2.2	Nanoparticles at different CVD conditions . . . . .	78
3.3	Conclusion . . . . .	83
<b>4</b>	<b>CNTs ON THE SUBSTRATE</b>	<b>85</b>
4.1	CNT evolution on the substrate . . . . .	85
4.2	Two kinds of nanoparticle formation mechanisms . . . . .	94
4.3	Conclusion . . . . .	97
<b>5</b>	<b>CONCLUSIONS</b>	<b>100</b>
5.1	General conclusions . . . . .	100
5.2	Perspectives . . . . .	102



# List of Figures

1.1	Schematics of $sp$ , $sp^2$ and $sp^3$ hybrid orbital. . . . .	5
1.2	Crystal structures of (a) graphite and (b) diamond. . . . .	6
1.3	Structure of buckminsterfullerene ( $C_{60}$ ). . . . .	7
1.4	TEM images of CNTs observed by Iijima [12]. . . . .	8
1.5	Structures of (a) SWNT and (b) MWNT. . . . .	9
1.6	(a) Schematic diagram showing how the graphene sheet is rolled up to form a CNT [45]. The result CNT structures with different chiralities (b) zigzag, (c) armchair and (d) chiral. . . . .	10
1.7	(a) Three-dimensional plot of the graphene energy bands and (b) a 2D projection. (c) Allowed 1D wavevectors for a metallic (9,0) SWNT. (d) Allowed 1D wavevectors for a semiconducting (10,0) tube [48]. . . . .	12
1.8	Schematic of the CNT growth by arc discharge [85]. . . . .	18
1.9	Schematic of the CNT growth by laser ablation [86]. . . . .	19
1.10	Schematic of the CNT growth by CVD [97]. . . . .	20
1.11	Schematics of the root-growth and tip-growth modes for carbon filament growth [111]. . . . .	21
1.12	Electron micrographs of the Ni catalyst and carbon nanofibres [141]. . . . .	24

1.13	<i>In-situ</i> high resolution TEM image sequence of a growing carbon nanofiber. Images (a-h) illustrate one cycle in the elongation/contraction process [141]. . . . .	26
1.14	Energy (top) and the corresponding configurations (bottom) as a function of the distance of carbon to the Ni(100) and Ni(111) surfaces. a1 and b1 show the adsorbed configurations, a2 and b2 are the transition states, and a3 and b3 are the systems with subsurface carbon [149]. . . . .	27
1.15	Schematic views of crawling and flying SWNTs with the relevant forces acting upon them: van-der-Waals attraction (vdW), growth extrusion (G), alignment forces (A), thermal fluctuations (T) and buoyant lift (B) [156]. . . . .	28
1.16	SEM images of the six-branch hybrid structure consisting of CNTs and heat-treated $\mu\text{Al}_2\text{O}_3$ [158]. . . . .	29
1.17	Schematic representation of the Ostwald ripening mechanism of catalyst during CNT growth by thermal CVD [159]. . . . .	30
1.18	Sketch map of catalyst landing status for the growth of MWNT arrays and SWNT films via FCCVD process [177]. . . . .	32
1.19	Heat exchange diagram during laser pulse heating. . . . .	36
2.1	Schematic of the CVD system used in this research. . . . .	45
2.2	Schematic of the solution spray in the CVD system. . . . .	45
2.3	Schematic of the stainless steel CVD reactor with seven small open-ended tubes at different positions labeled as P1, P2, P3, P4, P5, P6 and P7 along the reactor. . . . .	47
2.4	Temperature profiles along the reactor of the stainless steel tube at different set temperatures. . . . .	47

2.5	Simulation for the gas stabilization time [218]. . . . .	49
2.6	Typical (a) SEM and (b) TEM images of CNTs grown on $\mu\text{Al}_2\text{O}_3$ . . . . .	50
2.7	Example of the TGA/DTG curves for CNTs grown on the $\mu\text{Al}_2\text{O}_3$ substrate. . . . .	51
2.8	Example of the Raman spectrum for CNT samples growth on the quartz substrate. . . . .	52
2.9	Experimental setup for LII measurements. 1. Nd:YAG pulsed laser (10 Hz, 1064 nm). 2. The stainless steel CVD reactor. 3. Small open-ended tubes installed at different positions along the reactor (P1-P7). 4. Area containing NPs (outlet of the small tube). 5. Laser energy meter. 6. 550 nm Dichroic shortpass filter. (7,8). Bandpass filter 492 and 694 nm. (9,10) Two PMTs. 11. Oscilloscope. (12,13). Reflection mirror. 14. Optic fiber. . . . .	54
2.10	Typical view of incandescence signals. 1. 694 nm. 2. 492 nm. . . . .	56
3.1	(a) High resolution TEM image of nanoparticles the center of heated zone (P5). (b) STEM image shows the lattice fringes of the iron core of nanoparticles at P5. (Selected area electron diffraction patterns (EDP) in the iron core region is shown in inset.) . . . . .	58
3.2	(a) Spectrum, (b) STEM image and (c,d) map distribution of chemical elements in the sample of nanoparticles obtained at the center of the heated zone (P5). . . . .	60
3.3	Nanoparticle size distribution in the gas phase at the center of the heated zone in the CVD reactor P5 at 850 °C. . . . .	61
3.4	Particle heat-up temperature $T_p^0$ of laser heated particles obtained at different laser fluences. . . . .	62

3.5	(a) Least-squares error $\chi^2$ as a function of thermal accommodation coefficient $\alpha_T$ and <i>CMD</i> . (b) Least-squares error $\chi^2$ as a function of thermal accommodation coefficient $\alpha_T$ (The <i>CMD</i> values associated to $\alpha_T$ are not presented in the graph). . . . .	64
3.6	Least-squares error $\chi^2$ as a function of thermal accommodation coefficient $\alpha_T$ with <i>CMD</i> fixed at 11.7 nm (TEM measurement). . . . .	65
3.7	Measured LII signal of nanoparticles in the gas phase and the best fit curve of calculated LII signals for $\alpha_T=0.01$ , $\alpha_T=0.09$ and $\alpha_T=0.5$ with <i>CMD</i> fixed at 11.7 nm (TEM measurement). . . . .	65
3.8	The first-order $S_i$ and the total-order $S_{T_i}$ Sobol sensitivity index of the main parameters in the LII model at the Fe/C mass ratio (a) 1:1 and (b) 5:1. . . . .	68
3.9	Uncertainties in particle sizing by LII at the Fe/C mass ratio (a) 1:1 and (b) 5:1. . . . .	69
3.10	Measured LII signals of nanoparticles in the gas phase and the best fit curves of calculated LII signal for (a) case 1 (750 °C, P5 ) and (b) case 2 (850 °C, P7 ). The corresponding size distribution of nanoparticles in (c) case 1 and (d) case 2. . . . .	70
3.11	Nanoparticle size evolution in the gas phase at different positions in the CVD reactor at 850 °C. . . . .	72
3.12	Typical TEM images of nanoparticles with low resolution obtained in the gas phase at the different positions (a) P2, (b) P3, (c) P4, (d) P5 (e) P6 and (f) P7. . . . .	73
3.13	High resolution TEM image of nanoparticles at the front of the heated zone P3. . . . .	74

3.14	(a) Spectrum, (b) STEM image and (c-e) map distribution of chemical elements in the sample of nanoparticles obtained at the front of the heated zone P3. . . . .	75
3.15	Nanoparticle size evolution in the gas phase at different positions in the CVD reactor at 850 °C. . . . .	76
3.16	Comparison between MOMIC simulation and analytical solutions. The reaction temperature is 1000 K and the initial ferrocene concentration is 280 ppm [172]. . . . .	78
3.17	Nanoparticle size evolution in the gas phase at the center of the reactor as a function of CVD duration. . . . .	80
3.18	Nanoparticle size distribution at different ferrocene concentrations. . . . .	81
3.19	Nanoparticle size distribution at different H <sub>2</sub> flow rates. . . . .	82
3.20	Nanoparticle size distribution at different C <sub>2</sub> H <sub>2</sub> flow rates. . . . .	83
4.1	SEM images of CNTs grown on quartz plate in the reactor at different axial locations (a) P1, (b) P2, (c) P3 and (d) P4. . . . .	87
4.2	(a) Raman spectra and (b) the corresponding intensity ratio between D band and G band ( $I_G/I_D$ ) of CNTs grown on quartz plate in the reactor at different axial locations (from P1 to P4). . . . .	88
4.3	TEM image of CNTs grown on quartz plate at the front of the reactor (P3). . . . .	89
4.4	Schematic of CNT deposition on quartz plate at 650 °C. The typical SEM images of CNTs grown at (a) 5-20 cm, (b) 20-35 cm, (c) 35-45 cm and (d) 45-60 cm. Note: P1 is put at the position of 0 cm, P5 is at 30 cm. . . . .	90

---

4.5	(a) Raman spectra and (b) the corresponding intensity ratio between D band and G band ( $I_G/I_D$ ) of CNTs grown on quartz plate in the isothermal area at 650 °C. . . . .	91
4.6	Typical TEM images of CNTs obtained on the quartz plate at (a) P4, (b) P5 and (c) P6. . . . .	91
4.7	CNT diameter distribution on quartz plate in the isothermal area.	92
4.8	SEM images of CNTs grown on $\mu\text{Al}_2\text{O}_3$ at the center of the heated zone (P5) at (a) 650 °C , (b) 750 °C and (c) 850 °C. . . .	93
4.9	TGA curves of CNTs synthesized on $\mu\text{Al}_2\text{O}_3$ at different temperatures. . . . .	94
4.10	Proposed models for nanoparticle formation in the gas phase and on the substrate under FCCVD condition. . . . .	96
4.11	TEM images of products collected directly in the gas phase under FCCVD condition at a C/Fe molar ratio of 132. . . . .	96
4.12	(a) SEM and (b) TEM image of the products collected on the quartz substrate under FCCVD condition at C/Fe molar ratio of 4356. . . . .	98
4.13	(a) Spectrum, (b) STEM image and (c) map distribution of chemical elements in the sample of the power. . . . .	98

# 1

## Introduction

### 1.1 MOTIVATION

Carbon nanotubes (CNTs) have been extensively investigated in the last decades for their outstanding properties and a wide range of potential applications, such as electronics [1–3], photonics [4, 5], energy storage [6, 7], water and air purification [8, 9], structural composites [10, 11]. Different techniques have been employed for the CNT growth, including arc discharge [12], laser ablation [13] and chemical vapor deposition (CVD) [14, 15] etc. Among all the different synthesis methods, floating catalyst CVD (FCCVD) approach, where both carbon feedstock(s) and catalyst precursor(s) are simultaneously fed into the reactor, allows low cost, high quality and continuous production for industrial purposes [16, 17]. It has been believed that thermal decomposition of ferrocene leads to the nucleation of iron particles, where decomposed carbon can diffuse, precipitate and assemble into tubular structures. The diameter of CNTs is directly proportional to the size of catalyst particles [18, 19] and the length of CNT is also affected by catalyst morphology and activity [20]. Therefore, the

control of the size and morphology of iron catalytic nanoparticles is critical for synthesizing large amount of CNTs with well-defined structures and properties [21, 22]. However, It remains an unsolved challenge. Since the catalytic nanoparticles originate from decomposition of ferrocene in the gas phase, homogeneous nucleation is proposed as one possible mechanism for iron nanoparticles formation. Therefore, a quantitative understanding of iron nanoparticle formation process in the gas phase during FCCVD is desired for large scale production. In order to study iron-based nanoparticles suspended in the gas phase, it is critical to provide real time information on the nanoparticle size and distribution. Traditional techniques like transmission electron microscopy analysis (TEM) etc. are capable of measuring the nanoparticle size and distribution. However, it is often difficult to apply to practical CVD conditions with its limitations. TEM sample holder can not bear the high temperature (commonly 600-900 °C ) inside the CVD reactor. Moreover, nanoparticle information determined by TEM is given after the CNT synthesis. Samples are possibly damaged or contaminated and also this procedure is complex and time consuming. Therefore, it is reasonable to develop an *in-situ* diagnostic technique.

Laser-induced incandescence (LII) has been recognised as one of the most promising techniques for *in-situ* quantitative measurements of particle size and distribution and has been used extensively during the last three decades. In this technique, a laser pulse heats a volume containing nanoparticles to temperatures high enough to emit thermal radiation, and the time-resolved incandescence of these particles is recorded. The particle size distribution can be obtained by fitting the simulated data to the experimentally observed data [23]. The early experiments about LII focus on soot size measurements [24–28]. Due

## 1.2. CNT SYNTHESIS BY FCCVD

---

to its non-intrusive, real-time and *in-situ* nature, it has recently been extended to a variety of a range of sources, such as Cu [29], Ti [30] and Fe [31, 32] and Fe-C nanoparticles [33, 34].

With its advantages, in this study LII technique was applied for nanoparticle sizing during the FCCVD synthesis of CNTs. High resolution Transmission electron microscopy (TEM) was used to characterize the nature and size of nanoparticles. The theoretical LII signal was simulated by taking into account the nanoparticle density, heat capacity and size distribution etc. A detailed sensitivity and uncertainty of the key parameters on the evaluated particle size for this model has also been estimated. Using the developed approach and high resolution TEM, the evolution of nanoparticles in the gas phase along the reactor axis was investigated. By correlating the information on axial nanoparticle evolution and the morphology of CNT synthesized on the substrate along the reactor axis, the roles of nanoparticles during FCCVD synthesis of CNTs were also discussed.

## 1.2 CNT SYNTHESIS BY FCCVD

### 1.2.1 CNT HISTORY

Carbon is known to be the most versatile element that exists on the earth. It is the fourth most abundant element in the universe by mass after hydrogen, helium, and oxygen. In addition, carbon is also a fundamental element of life. Carbon compounds form the basis of all life on the earth and the carbon-nitrogen cycle provides some of the energy produced by the sun and other stars. The element carbon occurs in all organic life and is the basis of organic chemistry. This nonmetal also has the interesting chemical property of being

able to bond with itself and a wide variety of other elements, forming nearly 10 million known compounds. Today, the majority of energy we used is based on the use of carbon-based fossil fuels, such as coal, natural gas and petroleum [35, 36].

Carbon is the sixth element in the element periodic table, with a ground-state electron configuration of  $(1s)^2(2s)^2(2p)^2$ , of which the four outer electrons are valence electrons. Due to its specific electronic structure, carbon atom has the ability to bond to themselves and to other atoms by mixing different orbitals, namely  $s$  and  $p$  orbital. Even a mixture of  $s$ ,  $p$  and  $d$  orbitals is possible. The  $sp$  hybridization is the result of the mixture of one  $2s$  orbital and one  $2p$  orbital, namely  $2p_x$ . The characteristic angle between the two hybrid orbitals is  $180^\circ$ . The two remaining  $2p$  orbitals are available for  $\pi$  bonding (see Fig. 1.1a). The  $sp^2$  hybridization is the combination of one  $s$  orbital and two  $p$  orbitals, namely  $2p_x$  and  $2p_y$ . They contribute together to a planar assembly with a characteristic angle of  $120^\circ$  between hybrid orbitals forming a  $\sigma$  bond. The additional  $p_z$  orbital is perpendicular to the  $sp^2$  hybrid orbitals and forms a  $\pi$  bond (see Fig. 1.1b). In the experiments a binding ability for four electrons in carbon atom is also detected. The reason is the combination of one  $s$  orbitals and three  $p$  orbitals,  $2p_x$ ,  $2p_y$  and  $2p_z$  (see Fig. 1.1c). The yield is  $sp^3$  hybridization. Since there are small energy difference between the  $2s$  and the  $2p$  state, so that it is easy to excite one electron from the  $2s$  state into the  $2p$  state. In the presence of a external perturbation, such as a nearby hydrogen, the energy difference is overcome to form four new hybrid orbitals. The direction of the orbitals and also the center of mass are determined by the specific contributions of the  $p$  orbitals and the  $s$  orbital. A combination of the hybrid orbitals produces a tetrahedral assembly with the center of mass in

the corners. The characteristic angle between the four hybrid orbitals in  $sp^3$  configuration is  $109.5^\circ$ . The bond nature finally determines the geometry and properties of carbon allotropes [37].

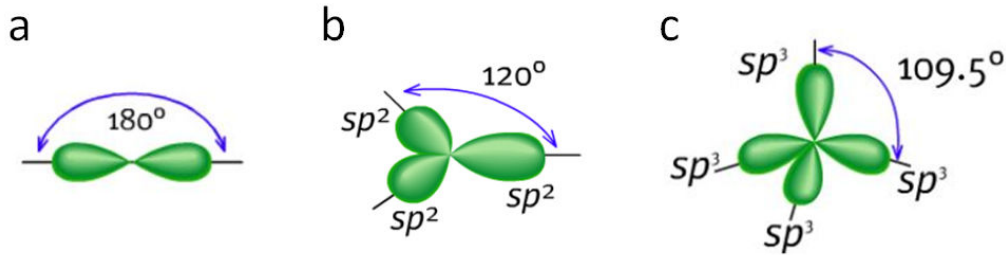


**Figure 1.1.** Schematics of  $sp$ ,  $sp^2$  and  $sp^3$  hybrid orbital.

Pure carbon is capable of forming many allotropes due to its valency, among which graphite and diamond are the two most commonly known ones. Their crystal structures shown in Fig. 1.2. Graphite is a typical example of  $sp^2$  hybridization crystal structure (see Fig. 1.2a). It consists of parallel carbon layers. In each sheet, carbon atoms are strongly connected through  $\sigma$  and  $\pi$  bonds to three nearest neighbors to form a hexagonal network. Between the layers the  $\pi$  orbitals give rise to weak Van-der-Waales (VdW) forces. As a result graphite is one of the softest materials known and it is commonly used in drawing pencil and as dry lubricants. In addition, graphite is a very good electrical conductor and opaque, and is widely used as electrodes. In contrary, diamond can be achieved by assembling many different  $sp^3$  hybridization carbon atoms to one crystal (see Fig. 1.2b). Due to the three dimensional  $sp^3$  structure the binding between neighboring carbon atoms is very strong. Therefore, diamond is one of the hardest materials known and can be used as cutting tools. Diamond has also been adapted for many other uses because of its extremely high melting temperature ( 5000 K) [38], marvelous thermal conductivity (900-2320

$\text{Wm}^{-1}\text{K}^{-1}$ ), which is 5 times as large as that of copper at room temperature [39], as well as wide bandgap and high optical dispersion [40].

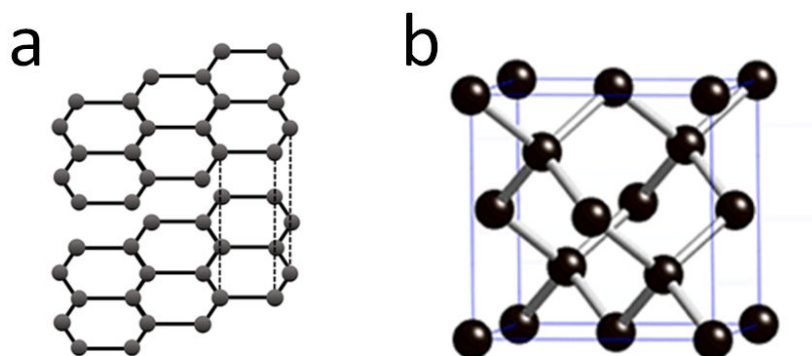


**Figure 1.2.** Crystal structures of (a) graphite and (b) diamond.

In 1985 the first fullerene molecule buckminsterfullerene ( $\text{C}_{60}$ ) was discovered by Kroto, Curl and Smalley et al [41].  $\text{C}_{60}$  molecule contains 60 carbon atoms arranged in closed shell. It exhibits the structure of a truncated icosahedron with twelve pentagonal rings and twenty hexagonal rings (see Fig. 1.3). By 1990 gram-sized samples of fullerene powder could be produced readily in a simple arc evaporation apparatus in all laboratories [42]. Since then, progress on fullerenes has evolved at a high pace. Consequently, numerous novel physical and chemical properties of  $\text{C}_{60}$  have been explored and a series of fullerene derivatives ( $\text{C}_{70}$ ,  $\text{C}_{76}$ ,  $\text{C}_{84}$  ...) with different shapes such as sphere, ellipsoid, ring or tube, also have been synthesized. The discovery of fullerenes greatly expanded the number of known carbon allotropes. Thus in 1996 the Nobel Prize in Chemistry was awarded to Kroto, Curl and Smalley.

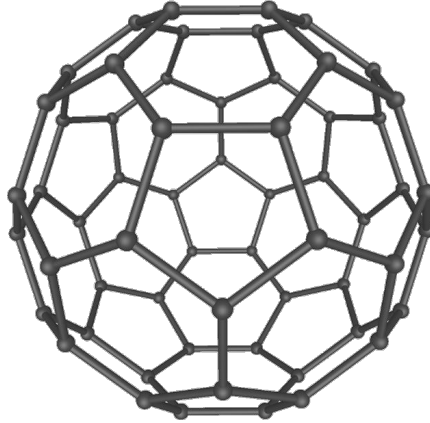


**Figure 1.3.** Structure of buckminsterfullerene ( $C_{60}$ ).

The huge interest in fullerenes synthesis directly results in the discovery of CNTs, which are also carbon allotropes and belong to the fullerene family. In 1991 Iijima et al. observed for the first time tubular carbon structures in the by-product of fullerenes synthesized by arc discharge [12]. The as-observed nanotubes consist of up to several tens of graphitic shells with adjacent shell separation of  $\sim 0.34$  nm, diameters of  $\sim 1$  nm and large length/diameter ratios (see Fig. 1.4). They are called multi-walled carbon nanotubes (MWNTs). Two years later, in 1993, single-walled carbon nanotubes (SWNTs) were also synthesized by arc discharge [43, 44]. The structure of a SWNT can be conceptualized by wrapping a one-atom-thick layer of graphite into a seamless cylinder. A significant progress is the success of synthesis of bundles of aligned SWNTs with small diameter distribution by laser-ablation [13]. Catalytic growth of nanotubes by the CVD method was first reported by Yacaman et al [14]. Inspired by these achievements, CNTs have always attracted the largest interest over the last two decades.

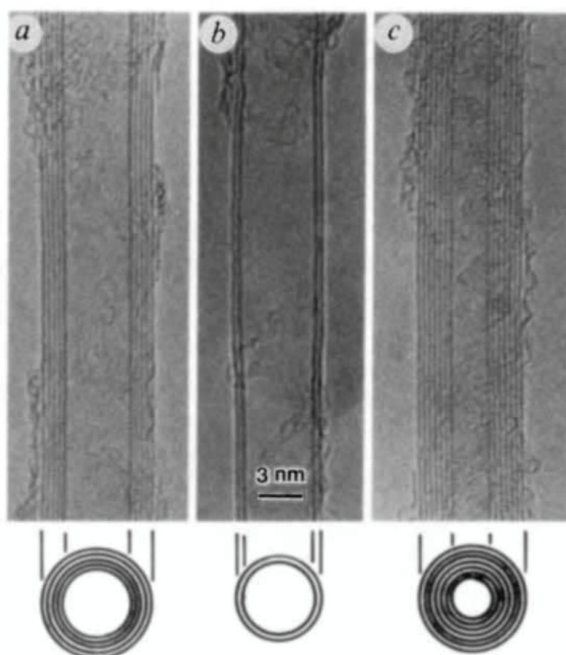


**Figure 1.4.** TEM images of CNTs observed by Iijima [12].

The two main structures of CNTs are SWNT and MWNT (see Fig. 1.5). An ideal SWNT can be visualized as a rolled-up sheet of a single layer of graphite (graphene layer) into a seamless cylinder. While an ideal MWNT is similar to a collection of concentric SWNTs with the interlayer distance of about  $3.4 \text{ \AA}$ , which is close to the distance between two graphene sheets in graphite. SWNTs are narrower in diameter than the thinnest line that can be obtained in electron beam lithography. Most SWNTs have a diameter of close to  $1 \text{ nm}$ , while MWNT diameter is larger than a few nm. But in both cases the CNT length can vary from several hundreds nm to a few mm. In general, both SWNTs and MWNTs have a length to diameter ratio of about 1000 and more, so they can be considered nearly as one-dimensional structures. Nowadays, SWNTs are still very expensive to produce, hence the development of cheaper means of synthesis techniques are highly desired. Double-walled carbon nanotubes (DWNTs) are

the special case of MWNTs. But their morphology and properties are similar to those of SWNTs.

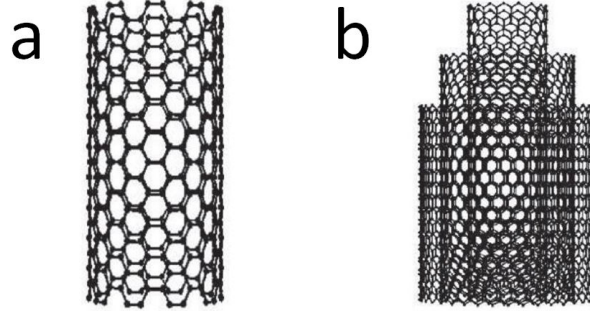


**Figure 1.5.** Structures of (a) SWNT and (b) MWNT.

As mentioned above, a graphene sheet can be rolled up more than one way (see Fig. 1.6a), producing different types of CNTs. The chiral vector  $\mathbf{C}$  is often used to describe how the graphene sheet is rolled up. It is defined by the following equation

$$\mathbf{C} = n\mathbf{a}_1 + m\mathbf{a}_2 \quad (1.1)$$

where  $n$  and  $m$  are integers. And  $\mathbf{a}_1$  and  $\mathbf{a}_2$  are two basis vectors of the graphene lattice. The translation vector  $\mathbf{T}$  is directed along the SWNT axis and perpendicular to  $\mathbf{C}$ . Moreover, the length of  $\mathbf{C}$ , namely  $L_c$ , is the circumference of the CNT and is given by

$$L_c = a\sqrt{n^2 + m^2 + nm} \quad (1.2)$$

where  $a$  is the length of unit vector  $\mathbf{a}_1$  or  $\mathbf{a}_2$ , 2.46 Å. The angle between the chiral vector and the zigzag direction in the honeycomb lattice of atoms, called chiral angle  $\theta$  ( $0^\circ \leq \theta \leq 30^\circ$ ), can be obtained by

$$\theta = \tan^{-1} \left( \frac{\sqrt{3}m}{2n + m} \right) \quad (1.3)$$

Therefore, a CNT is uniquely specified by the pair of integers  $(n, m)$  or the chiral angle. There are two limiting cases, corresponding to the achiral tubes, known as zig-zag tubes ( $m = 0$  or  $\theta = 30^\circ$ ) and armchair tubes ( $m = n$  or  $\theta = 0^\circ$ ). Otherwise, CNTs with  $n \neq m$  ( $0^\circ < \theta < 30^\circ$ ) are called chiral tubes. The three types of CNTs are presented in Fig. 1.6b-d.

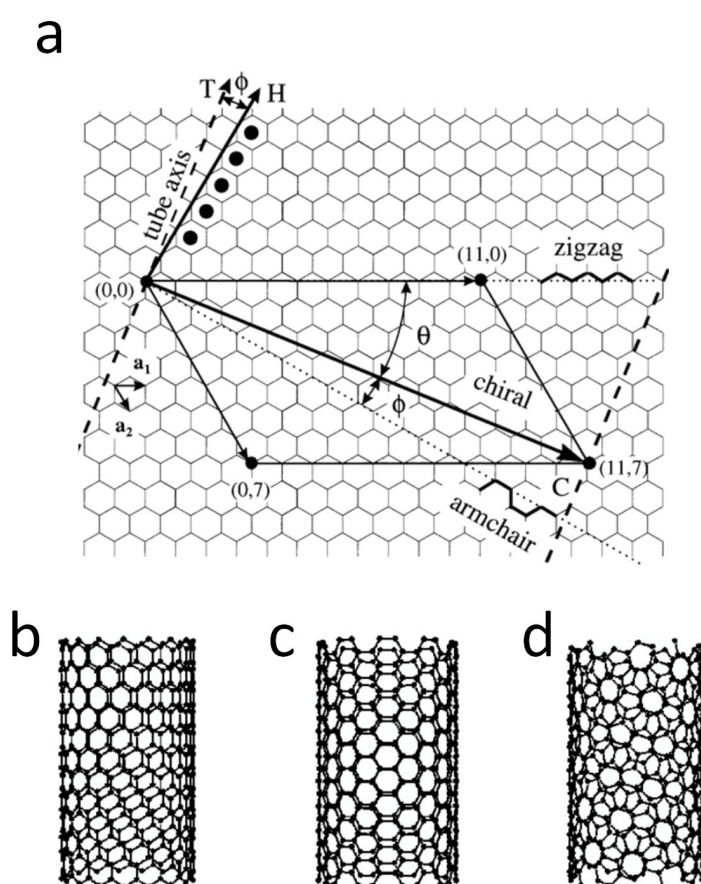


**Figure 1.6.** (a) Schematic diagram showing how the graphene sheet is rolled up to form a CNT [45]. The result CNT structures with different chiralities (b) zigzag, (c) armchair and (d) chiral.

## 1.2. CNT SYNTHESIS BY FCCVD

---

### 1.2.2 CNT PROPERTIES

CNTs have always attracted considerable interest in scientific community and in industry since their first observation by Iijima in the early 1990s [12]. CNTs exhibit extraordinary electronic, mechanical and thermal properties, which make them highly desirable in a variety of industrial applications, such as electronics [1, 2], photonics [4], energy storage [6, 7], water and air purification [8, 9], structural composites [10, 11]. In past two decades, a huge progress has been achieved in CNT applications. Some of them have been commercialized, such as polymers and lithium ion batteries [46].

### ELECTRICAL PROPERTIES OF CNTS

Since an SWNT can be regarded as a rolled-up sheet of a graphene layer, the band structure of the SWNT can be derived from the one of the graphene layer [47]. It is well known that graphene is a semimetal with valence and conduction bands degenerate at only six corners  $\mathbf{K}_B$  of the hexagonal first Brillouin zone. The Fermi surface of the graphene sheet is thus reduced to these six points [48], as presented in Fig. 1.7. When forming a tube, owing to the periodic boundary conditions imposed in the circumferential direction, only a certain set of  $k$  states of the planar graphite sheet is allowed. Whenever the allowed  $k$  includes the point  $K$ , the system is a metal with a non-zero density of states at the Fermi level, resulting in a 1D metal with two linear dispersing bands. When the point  $K$  is not included, the system is a semiconductor with different sized energy gaps. Therefore, CNTs with  $|n - m| = 3i$  are metallic tube, and those with  $|n - m| = 3i \pm 1$  are semiconducting tube, where  $i$  is an integer. It could be concluded that all armchair SWNTs should be

metallic, while one-third of zigzag and all chiral SWNTs are semiconducting. However, the electrical properties of MWNTs are quite complex as their inter-wall interactions non-uniformly distribute the current over individual tubes. They are often investigated by First-principles calculations and experiments.

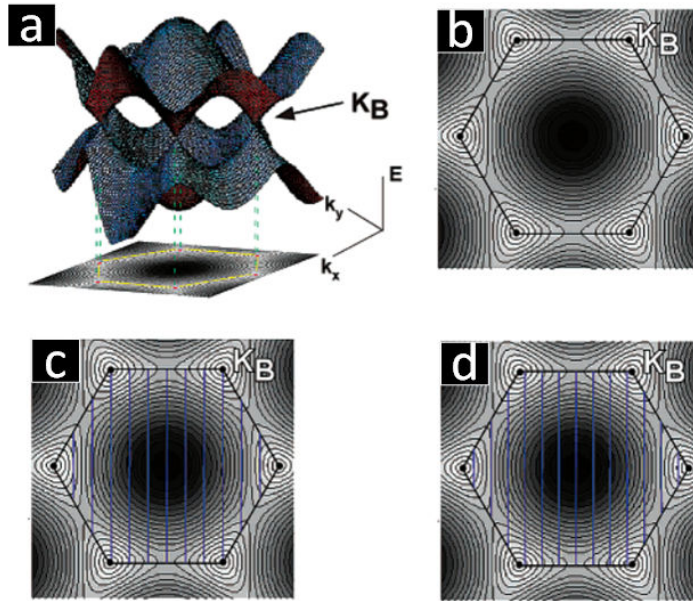


**Figure 1.7.** (a) Three-dimensional plot of the graphene energy bands and (b) a 2D projection. (c) Allowed 1D wavevectors for a metallic (9,0) SWNT. (d) Allowed 1D wavevectors for a semiconducting (10,0) tube [48].

In 1997 a big breakthrough on SWNT electrical conductivity was achieved by Smalley et al [49]. It was found that CNTs could act as quantum wires. Due to the confinement of conduction electrons in the transverse direction of the wire, their transverse energy is quantized into a series of discrete values  $E_0$ ,  $E_1$  and so on, where  $E_0$  refers to the lowest energy level. Because of the quantization of electron energy, the resistance is also quantized. One year later the quantized conductance in a SWNT was also observed by Frank et al.

$$G = nG_0 = 2ne^2/h \quad (1.4)$$

## 1.2. CNT SYNTHESIS BY FCCVD

---

where  $n$  is integer;  $e$  and  $h$  are charge of the electron and plank's constant. Different from SWNTs, MWNTs exhibit not only multiples of conductance quantum, but also non-integer quantum conductance values such as  $G = 0.5G_0$  [50]. Heer et al. measured the intrinsic resistance of WNNTs. The value reaches to at most  $200 \text{ } \Omega/\mu\text{m}$  [51]. Hence the momentum mean free path is greater than  $30 \text{ } \mu\text{m}$ , much larger than the tube length. It implies that these tubes are ballistic.

### MECHANICAL PROPERTIES OF CNTs

Due to the strong C-C  $sp^2$  bonding, CNTs are expected to have outstanding mechanical properties including high strength, high stiffness and high flexibility [52].

In 1996 Treacy et al. obtained the Young's modulus of an individual MWCNT by measuring the amplitude of its intrinsic vibration in TEM [53]. The obtained average value is 1.8 TPa, which is much higher than that of typical carbon fibers, 680 GPa [54]. This technique was also applied to measure the Young's modulus of isolated SWNTs and the average value is about 1.25 TPa [55]. However, this method has drawbacks. Firstly, the measured values of the Young's modulus by this technique have a considerable spread due to the inevitable uncertainty in estimation of CNT length. In addition, it can not evaluate the strength and toughness of CNTs, since the tubes can not be strained at will.

Wong et al. explored another method to measure the mechanical properties of MWNTs by the use of atomic force microscopy (AFM) [56]. In this method, MWNTs were pinned at one end to molybdenum disulfide surfaces. This method allows us to measure not only the Young's modulus, but also the

strength and toughness. The estimated Young's modulus is 1.26 TPa. CNTs buckle elastically at large deflection angles of  $10^\circ$  for the length of 1 m. The average bending strength is 14.2 GPa. The toughness is estimated to be 100 keV for a 30 nm diameter CNT, Therefore, CNTs show remarkable ability to elastically sustain loads at large deflection angles, by which CNTs can store considerable energy. Yu et al. measured the tensile strength of SWNT ropes and MWNTs with a "nanostressing stage" located inside a LEO 1530 scanning electron microscope (SEM). The estimated Young's modulus of SWNT is from 320 to 1470 GPa [57] and The estimated Young's modulus of MWNT is between 270 and 950 GPa [58].

Theoretical evaluation of the Young's and shear modulus could be obtained by calculating the second derivative of the strain energy with respect to the nanotube elongation [59]. In the force-constant model the average value of Young's modulus is 0.97 TPa and of shear modulus is 0.45 TPa, respectively [60]. Molecular dynamics (MD) simulations were also implemented to investigate the mechanical properties of CNTs. The C-C interactions were described by Tersoff-Brenner potentials [52, 61, 62]. For tubes in diameter of 1 nm, the values of Young's modulus and shear modulus are 5.5 TPa and 0.8 TPa, respectively. The average value of the Young's modulus for SWNTs is predicted to be 1.24 TPa by a non-orthogonal tight-binding model [63]. Pseudopotential density-functional theory (DFT) calculations were also applied to study the Young's modulus SWNTs. It was found that the obtained value for Young's modulus significantly depends on the choice of the nanotube volume and the average value is found to be 56 eV (times nanotube volume) [64]. Table 1.1 shows the main mechanical properties of SWNTs, MWNTs, stainless steel and Kevlar (an exceptionally strong, light, man-made fibre). As can be seen that

**Table 1.1.** Main mechanical properties of CNTs, stainless steel and Kevlar.

Materials	Young's modulus (TPa)	Tensile strength (GPa)	Elongation at break (%)
SWNTs	~1	13-53	16
MWNTs	0.8-0.9	11-150	-
Stainless Steel	~0.2	0.65-3	15-50
Kevlar	~0.15	~3.5	~2

CNTs are the strongest and stiffest material in term of tensile strength and elastic modulus.

#### THERMAL PROPERTIES OF CNTS

The specific heat and thermal conductivity of CNTs are determined primarily by phonons. The measurements of the specific heat of MWNTs or SWNTs from 1 K to 300 K reveal the linear dependence of the specific heat over the entire temperature interval [65–70]. The linear temperature dependence can be explained by the linear  $\mathbf{k}$ -vector dependence of the frequency of the longitudinal and twist acoustic phonons [71]. While a  $T^{0.62}$  behavior of the specific heat was observed below 1 K [68]. It is attributed to the transverse to the transverse acoustic phonons with quadratic  $\mathbf{k}$  dependence [72].

CNTs display the very high thermal conductivity. The MD simulations predicted an unusual high thermal conductivity of about  $6600 \text{ Wm}^{-1}\text{K}^{-1}$  for an isolated (10, 10) nanotube at room temperature [73], comparable to the thermal conductivity of an isolated graphene layer or diamond. These high values are attributed to the large phonon mean free path. Direct measurement of the thermal conductivity of an individual MWNT was performed by using a micro-fabricated suspended device in 2001 [70]. The observed thermal conductivity is more than  $3000 \text{ Wm}^{-1}\text{K}^{-1}$  at room temperature, which is  $\sim 7$  times higher than

that of copper,  $385 \text{ Wm}^{-1}\text{K}^{-1}$ . Furthermore, the temperature dependent behavior of thermal conductivity was observed. The thermal conductivity varies as  $T^{2.5}$  at temperature range from 8 K to 50 K. At temperature from 50 K to 150 K the thermal conductivity increases quadratically in  $T$ . A peak at 320 K will appear with further increase in the temperature.

Due to their high thermal conductivity and large in-plane expansion, CNTs exhibit exciting prospects in nanoscale molecular electronics, sensing and actuating devices, reinforcing additive fibers in functional composite materials.

### 1.2.3 CNT SYNTHESIS ROUTES

In 1991 CNTs were first produced by the arc-discharge method [12]. From then on, a variety of techniques have been explored for CNT production, such as laser ablation [13], CVD [14, 15], diffusion flame [74–76], electrolysis [77, 78], use of solar energy [79], heat treatment of a polymer [80], and low temperature solid pyrolysis [81]. Among them, arc-discharge, laser-ablation and CVD are the three most popular ones.

#### ARC DISCHARGE

Iijima first observed nanotubes synthesized from the electric arc discharge technique. This method has been used long before that for carbon fiber and fullerene synthesis. A schematic of the apparatus of arc discharge is depicted in Fig. 1.8. The synthesis is performed in a chamber filled with an inert gas (He or Ar). A voltage, approximately 20 V, is applied to the two rods to achieve a stable discharge arc. The current is typically 50 to 100 A. The temperature in the inter electrode plasma region can reach about 6000 K. So the discharge vapor-

## 1.2. CNT SYNTHESIS BY FCCVD

---

izes the surface of one electrode and forms deposit on the other one. The final product depends crucially upon the composition of the anode. To synthesize high purity MWNTs, graphite electrodes are required. To synthesize SWNTs, we can add some amount of metallic catalyst particles into the electrodes, such as Fe, Co, Ni [44]. The final products can be controlled by the size of the graphite rods, the gap between the anode and cathode, the inlet gas and the voltage etc. A certain amount of hydrogen addition into the inert gas is more effective for MWNT production [82, 83]. It is explained by the high temperature and high activity of the hydrogen arc faces. And an angle of 30° inclination of graphite electrodes can accelerate CNT synthesis and yields SWNTs at a rate of 1 g/min. Large-scale synthesis of SWNTs by arc discharge was achieved by using a bimetallic Ni-Y catalyst in He ambient gas [84]. Arc discharge is one of easiest ways to produce CNTs in large scales. CNTs produced by this way have a good graphitization degree due to high synthesis temperatures. However, this technique produces a complex mixture of components. Purification procedure has to be followed after the synthesis to separate CNTs from the impurities in the products.

### LASER ABLATION

Laser ablation was first used for the fullerene synthesis. It is another popular method to grow CNTs. It was first demonstrated in 1995 by Smalley et al [86]. Laser ablation works through the same mechanism as arc discharge, but instead of producing heat through electrical discharge a laser is used. A focused and powerful laser is used to rapidly heat carbon and vaporize it. The general set-up for laser ablation is shown in Fig. 1.9. The synthesis is performed in a quartz tube as the reactor [87]. A pellet of graphite is put in the middle

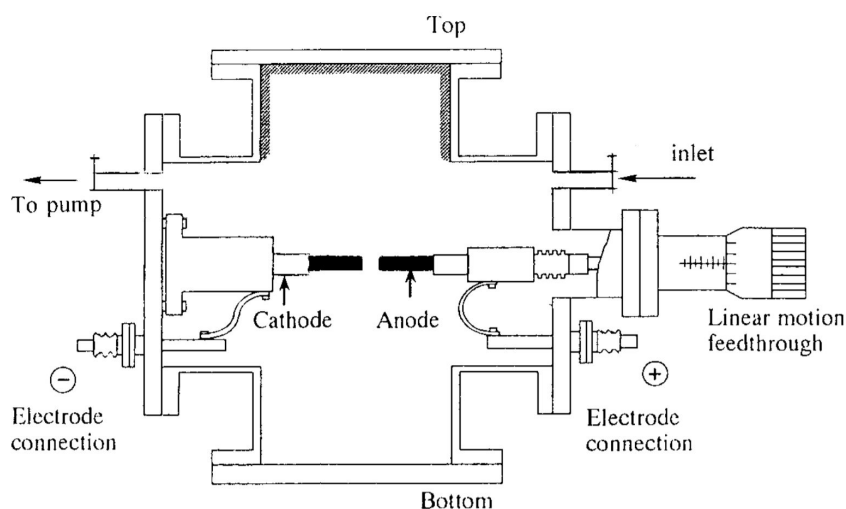


**Figure 1.8.** Schematic of the CNT growth by arc discharge [85].

of the quartz tube. And then the reactor is heated to 1000-1200 °C under an inert gas flow. The vaporization laser is the second harmonic (532 nm) of a Nd:YAG laser providing 10 ns, 250 mJ pulses at 10 Hz. The nearly Gaussian output beam is focused onto the target with a 3-mm or 6-mm beam spot. The laser beam scans across the target surface under computer control. Then, the CNTs nucleate in the vapor phase and are carried away by the gas flow, finally deposit on a collector outside the furnace in the cooling zone. In laser ablation the temperature and the pulse time can be precisely controlled. So by tuning the process parameters we can obtain high quality CNTs. However, it suffers from drawbacks. Firstly, it is difficult to scale up production to the industrial level using these approaches. In addition, this technique produces a complex mixture of components. It is quite difficult to purify, manipulate, and assemble CNTs for building nanotube device architectures for practical applications. CNTs are always damaged during the purification process.

## 1.2. CNT SYNTHESIS BY FCCVD

---

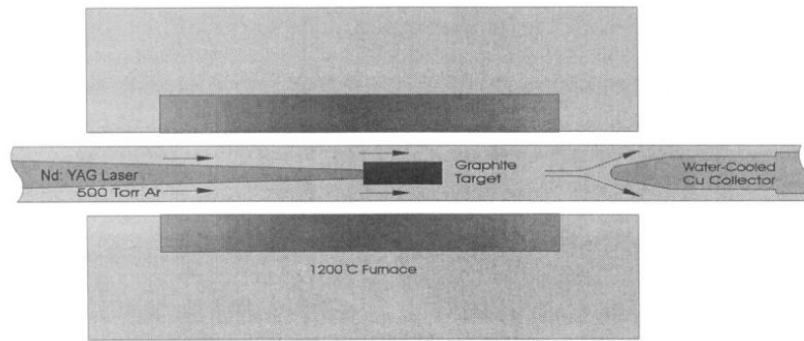


**Figure 1.9.** Schematic of the CNT growth by laser ablation [86].

### CHEMICAL VAPOR DEPOSITION

Besides arc-evaporation and laser ablation methods, CVD method is also popular and widely used for CNT synthesis. Catalytic growth of nanotubes by CVD method was first reported by Yacaman et al [14]. Since then many research groups in the world showed their great enthusiasm in CVD for CNT growth. It is technically easy to carry out as in its simplest version it only requires an oven, a tubular reactor and a set of mass flow controllers to feed the gas mixture. Therefore, CVD method is the most promising one for large-scale production at lower cost. [88–92].

CNT synthesis by CVD is based on the catalytic decomposition of hydrocarbons on catalysts at temperature about 600-1200 °C. Fig. 1.10 shows a schematic diagram of the experimental set-up used for CNT growth by CVD method. A wide range of metal catalysts and hydrocarbons can be used. The carbon sources are methane, acetylene, benzene, xylene [91, 93–95]. Catalysts can be usually transition metals (Fe, Co, Ni), alloys, in the form of thin films, as-deposited nanoparticles, liquid (catalytic precursors). A general CVD process includes several fundamental steps [96], including catalytic or pyrolytic decomposition of hydrocarbons on the catalyst surface or in the gas phase to release

reactive carbonaceous species, diffusion of these reactive species on/into the catalyst, nucleation of the graphitic nuclei on the catalyst surface, and further incorporation of carbon into the growing graphitic structure to elongate the tube.

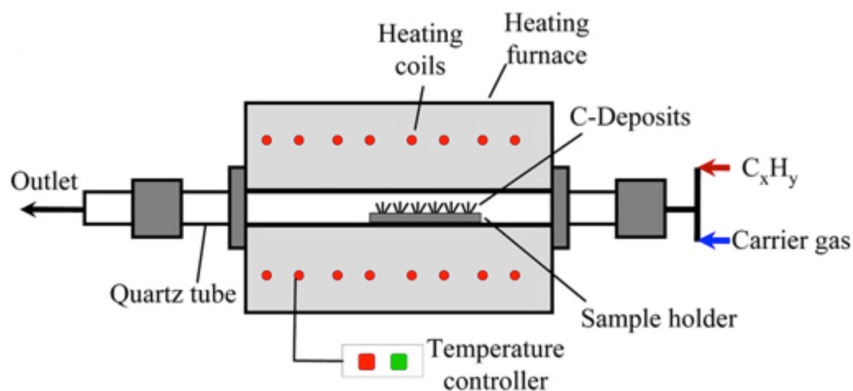


**Figure 1.10.** Schematic of the CNT growth by CVD [97].

Based on the general principle of CVD illustrated in Fig. 1.10, various types of variant were developed, such as plasma-enhanced chemical vapor deposition (PECVD) [98, 99], FCCVD [100] and HiPCO (high pressure CO disproportionation) process [101].

#### 1.2.4 CNT GROWTH MECHANISM IN FCCVD

Among the different synthesis methods, FCCVD is currently the most common technique to grow CNTs, where carbon sources and catalytic precursors are injected simultaneously into the reaction system [102, 103]. The organometallic compounds (ferrocene [104, 105], cobaltocene [106], nickelocene [107]) and iron pentacarbonyl [101] are the most commonly used catalytic precursors. The carbon sources can be methane, acetylene, benzene, xylene [91, 93–95]. Normally,

## 1.2. CNT SYNTHESIS BY FCCVD

---

the process is carried out under an mixture of hydrogen and inlet gas atmosphere. Despite of enormous experimental and theoretical studies, the growth mechanism of CNTs remains poorly understood [108].

### GENERAL MECHANISM

Vapor-Liquid-Solid (VLS) model is the first approach to understand the growth of CNTs which originally was suggested by Wagner and Ellis to explain the growth of Si whiskers [109]. Using VLS model, Baker explained the mechanism of carbon filament growth [110]. In this model, carbon atoms from the decomposition of the hydrocarbon dissolve into the catalyst, and then precipitate on the surface of the catalyst to form a carbon nanofilament. There are two general cases which distinguish from each other by the interactions between the metal and the support. The weak interactions yield tip-growth where nanofilament lifts the catalyst from the substrate during the growth, whereas the strong interactions result in base-growth where the catalyst is strongly attached to the substrate during the growth process, as presented in Fig. 1.11.

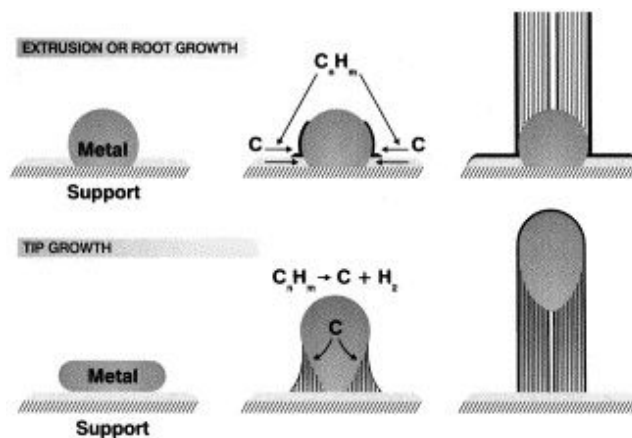


**Figure 1.11.** Schematics of the root-growth and tip-growth modes for carbon filament growth [111].

The growth model for carbon filaments has been widely used for CNT growth. The VLS mechanism is supported by some experiments, for example, in the case of carbon nanofibers and MWNTs growth on iron [112, 113]. It roughly describes the CNT growth process and proposes a possible way to control the CNT diameter by adjusting the catalyst particle size. However, this model is too simple to well describe the complex CNT nucleation and growth processes. Some details on the molecular aspects of CNT growth remain to be elucidated.

The driving force that pushes carbon atoms to diffuse in the catalyst has given rise to numerous debates. As the dissociation of many hydrocarbons on the surface of the metal is exothermic and the precipitation of solid carbon is endothermic, Baker et al. suggested that the driving force is the temperature gradient within the catalyst. This hypothesis can explain the growth of CNTs when the dissociation of the carbon precursor is exothermic. But it encounters difficulties in the case of dissociation of alkanes [114]. Tibbetts proposed that the gradient in chemical potential is the driving force [115]. But this hypothesis also suffers drawbacks. It fails to explain the growth when the particles remain solid.

Catalyst nanoparticle plays an important role in CNT synthesis. The chemical and physical states of the catalyst should also be addressed. They are strongly influenced by the catalytic activity, and the solubility and diffusivity of carbon. Metallic particles (such as Fe, Co, Ni) are commonly considered as the catalysts for CNT formation. In fact they are often observed during CNT growth [116–119]. Beside Fe, Co and Ni, CNT growth have been reported using a wide range of metallic particles, such as Pd, Pt, Au, Mn, W, Ti, Mg, Al, In, Na, K, Cr and Cs [120–127] and other mixed compounds, such as FeSi, SiC,

## 1.2. CNT SYNTHESIS BY FCCVD

---

SiO<sub>2</sub>, Al<sub>2</sub>O<sub>3</sub>, TiO<sub>2</sub>, ZnO, Er<sub>2</sub>O<sub>3</sub> [128–131]. The mixture of active catalysts, such as Fe, Co and Ni are also frequently used as the catalysts [132, 133]. According to the VLS model a metal carbide phase is expected to form during CNT growth. In fact, in the case of iron-based catalyst, iron carbide phase (Fe<sub>3</sub>C) is often detected by *ex-situ* post-experimental characterizations [134]. *In-situ* high resolution TEM observed that the transformation from Fe into Fe<sub>3</sub>C prior to CNT growth, indicating that Fe<sub>3</sub>C phase is active for CNT formation [135, 136]. Mazzucco et al. reported that the cementite (Fe<sub>3</sub>C) structure are active for CNT growth by combining *in-situ* TEM and DFT calculations [137]. However, CNT growth directly using Fe<sub>3</sub>C as the catalyst ended up in failure [138], implying that Fe<sub>3</sub>C can not catalyze CNT growth. Thence the chemical and physical states of the catalyst are still under debate.

VLS model suggests that catalytic particles might be liquid during CNT growth process, because during the growth, the particle exhibits a liquid-like morphology by *in-situ* high resolution TEM, which is similar to a melted metal droplet [110]. CVD processes are commonly conducted at temperatures 500–800 °C which is far below the melting temperature of iron 1534 °C and the iron carbon eutectic temperature 1147 °C. However, for nanosized metal particles, the melting temperature is dependent on their sizes. It could be estimated that metal particles with diameters less than 2–3.5 nm are expected to be in liquid state. After dissolving certain amounts of carbon, the above evaluated diameter values might be increased a little. However, the melting point of the particles is still much higher than the CNT synthesis temperature in some cases [139]. Oberlin et al. observed that catalyst metal particles may be solid by using high resolution TEM and selected area electron diffraction (SAED) analysis. They also found that there is a strong correlation between the crystalline structure

of the catalyst metal particle and the one of the graphene sheets [140]. In 2004 Helveg et al. for the first time recorded, in real time, MWNT growth from a Ni particle inside a high resolution TEM (Fig. 1.12) [141]. In the high resolution TEM image, the lattice fringes can be clearly seen. Hofmann et al. investigated SWNT growth on both Ni and Fe by using *in-situ* high resolution TEM and *in-situ* X-ray photoelectron spectroscopy (XPS) [142, 143]. They also found that SWNTs grow from solid particles. Based on these *in-situ* observations, vapor-solid-solid (VSS) model was also proposed for CNT growth.

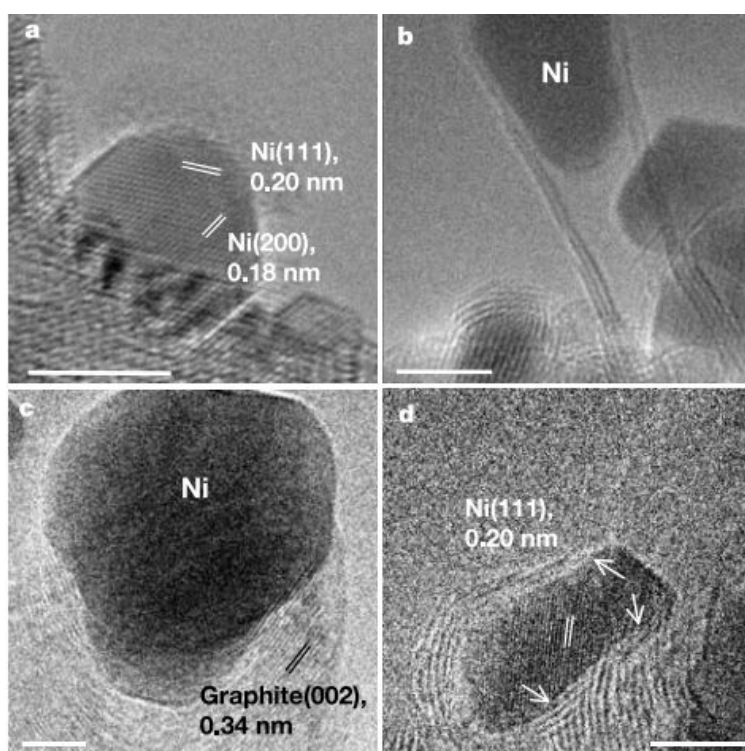


**Figure 1.12.** Electron micrographs of the Ni catalyst and carbon nanofibres [141].

The carbon diffusion pathway during CNT growth is still a highly debated issue. Since carbon diffusion pathway is largely influenced by the carbon solubility of catalyst nanoparticles. Baker et al. postulated that carbon diffusion should take place in the bulk of nanoparticles during CNT growth by measur-

ing the activation energy of carbon diffusion in catalyst nanoparticles. They also predicted that carbon diffusion is the rate-limiting step [112]. Besides bulk diffusion, several groups also reported that carbon diffusion should take place on the surface of the catalyst particle [141, 144–146]. In 2004 Helveg et al. observed the CNT growth process over Ni particles by an *in-situ* high resolution TEM, as shown in Fig. 1.13. They proposed that the nucleation and growth of graphene layers are found to be assisted by a dynamic formation and restructuring of mono-atomic step edged at the Ni surface. This observation reveals that the carbon diffusion precedes on the catalyst surface. DFT calculations found that the activation energy of carbon surface diffusion on Ni is about 0.4 eV, much lower than that for bulk diffusion [147]. *Ab-initio* MD simulations also showed that the surface diffusion of carbon atoms on a 1 nm Fe particle is significantly faster than carbon diffusion in the bulk of the particle [148]. In addition, Hofmann et al found that sub-surface diffusion is energetically more favorable than surface or bulk diffusion [147]. Rinaldi et al reported that carbon migration to the sub-surface is actually favored for both Ni(111) and Ni(100) (see Fig. 1.14) [149]. According to above studies, it seems that all bulk, surface and subsurface diffusion are possible during CNT growth. And the type of diffusion depends on the catalyst chemical composition and morphology. For Fe, bulk diffusion is more favorable due to the high activity. In contrast, for Ni and Cu, carbon diffusion proceeds either on the surface or in the subsurface.

The substrate plays an essential role in stabilizing catalyst nanoparticles. A variety of supports have been used to synthesize CNTs, including SiO<sub>2</sub> [150], Al<sub>2</sub>O<sub>3</sub> [150, 151], MgO [152], CaO [150], zeolite [151], anodic aluminum oxide (AAO) [153] and graphite [154] etc. The catalyst-substrate interactions can significantly alter the chemical and physical states of the catalyst and conse-

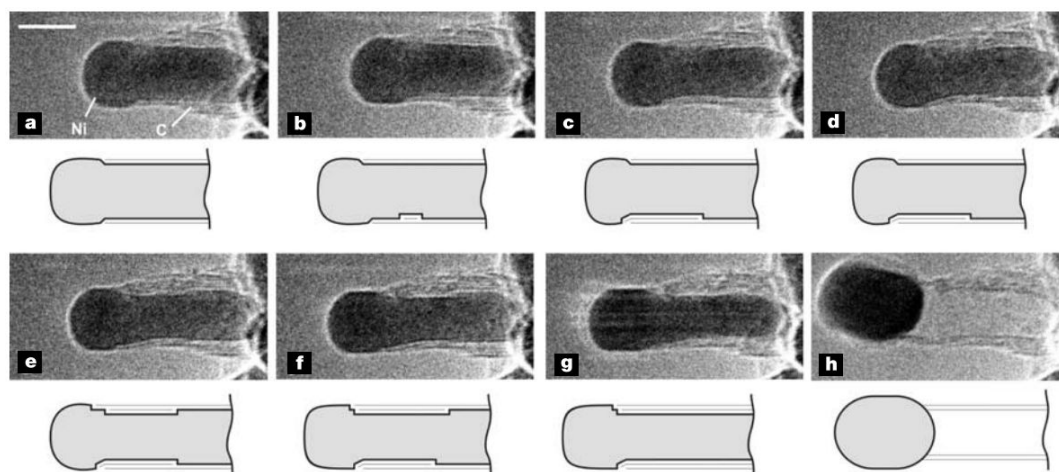


**Figure 1.13.** *In-situ* high resolution TEM image sequence of a growing carbon nanofiber. Images (a-h) illustrate one cycle in the elongation/contraction process [141].

quentially influence the CNT growth mechanism. As mentioned before, the growth model of CNTs (tip-growth or base-growth) strongly depends on the catalyst-substrate interactions. For example, CNT growth on  $\text{SiO}_2$  exhibits a tip growth mode with a slow growth rate of less than 100 nm/min. In contrast, the growth on Ta follows a base growth mode with a fast growth rate exceeding 1  $\mu\text{m}/\text{min}$  [155]. Two distinct kinds of CNTs, namely crawling and flying nanotubes (see Fig. 1.15), can be obtained by fabricating barriers and gaps on the substrate, due to either a continuous intimate contact with the substrate dominated by vdW forces or a mere substrate anchoring of nanotubes held afloat during growth [156]. CNT growth is also affected by the morphology of the substrate. The high magnification SEM images demonstrate that the growth of CNTs takes place at the crystal step sites, rather than in the flat regions. The direction of CNT branches is strongly dependant on the orientation of the crystal steps, as shown in Fig. 1.16. Moreover, the activity of catalyst is influenced by the substrate. Su and Colomer et al. observed that Fe exhibits higher activity on  $\text{Al}_2\text{O}_3$  than on  $\text{SiO}_2$  [104, 157]. Willems et al. observed that

## 1.2. CNT SYNTHESIS BY FCCVD

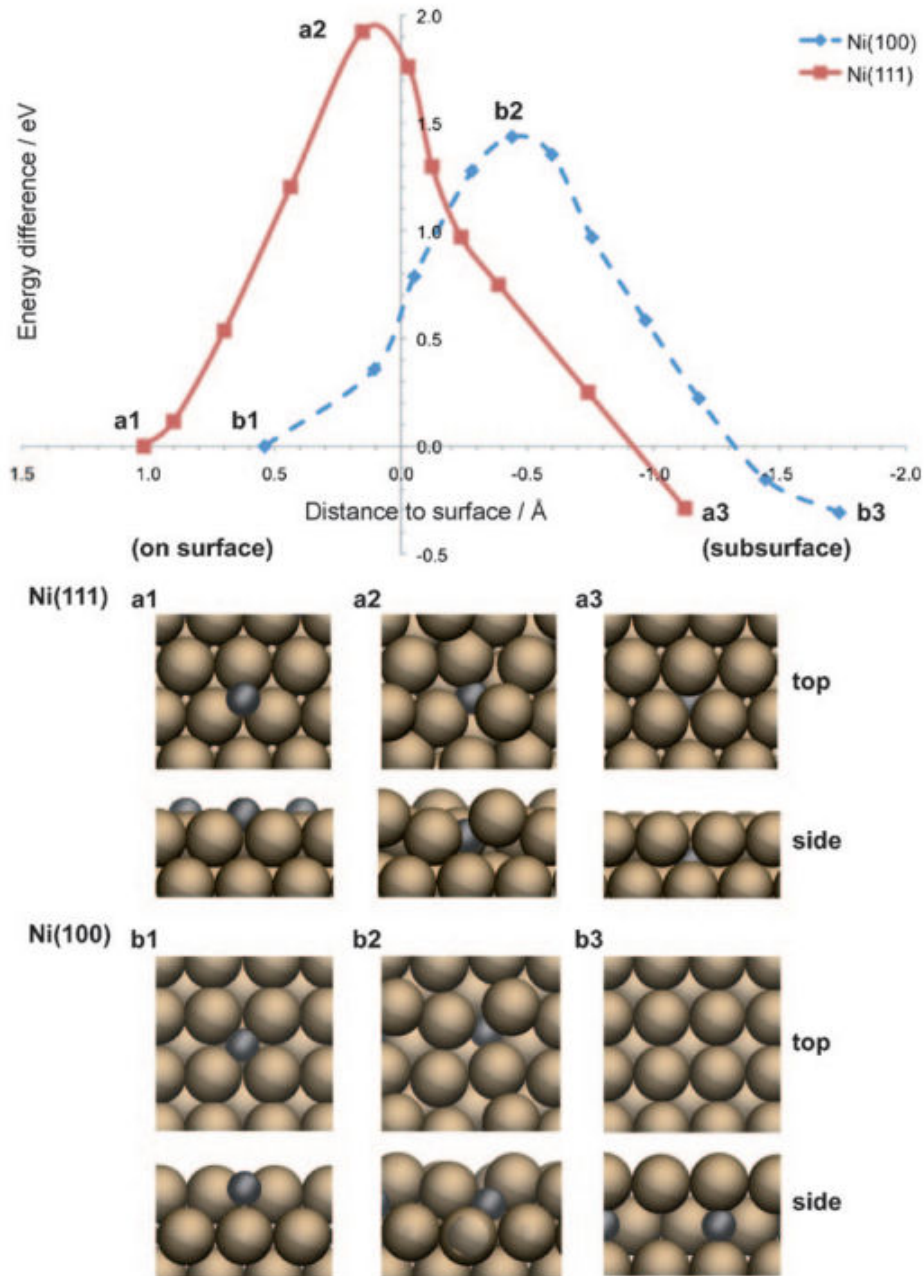


**Figure 1.14.** Energy (top) and the corresponding configurations (bottom) as a function of the distance of carbon to the Ni(100) and Ni(111) surfaces. a1 and b1 show the adsorbed configurations, a2 and b2 are the transition states, and a3 and b3 are the systems with subsurface carbon [149].

Co-Mo exhibit better results on alumina than on zeolite [151]. Vander Wal et al. found that Ni is more active on  $\text{TiO}_2$  than on  $\text{SiO}_2$ ,  $\text{Al}_2\text{O}_3$  and CaO. While Cu is more active when supported on CaO and  $\text{SiO}_2$  and less active on  $\text{TiO}_2$  and  $\text{Al}_2\text{O}_3$  [150].

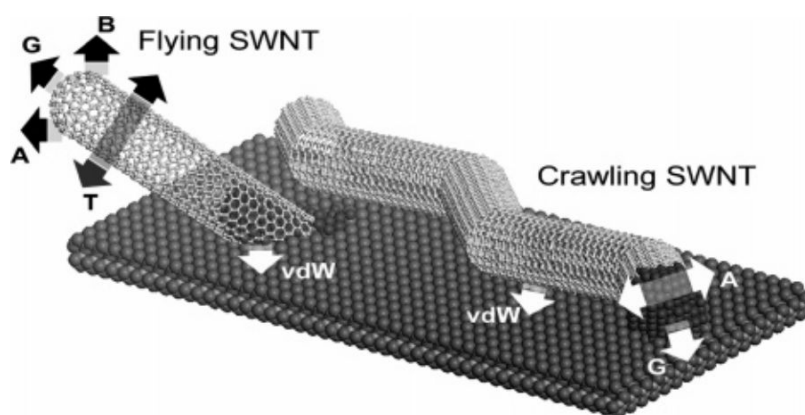


**Figure 1.15.** Schematic views of crawling and flying SWNTs with the relevant forces acting upon them: van-der-Waals attraction (vdW), growth extrusion (G), alignment forces (A), thermal fluctuations (T) and buoyant lift (B) [156].

Furthermore, the catalyst-substrate interactions can cause deactivation of the catalyst. Ostwald ripening of catalyst particles during the growth is a well-known cause of deactivation (see Fig. 1.17) [159]. It arises from Fe particle migration. The small particles will tend to shrink, since they are thermodynamically less stable than the large ones, thus leading to growth termination. A small amount of water addition can avoid Ostwald ripening by the formation of hydroxyl groups on the alumina surface. In addition, the diffusion of metal into the support can also result in the poisoning of catalysts [160, 161]. In the case of  $\text{SiO}_2$  as the catalyst, the growth termination is ascribed to the formation of the catalytically inactive silicide compounds which prevent the catalyst from reacting with the carbon feedstock for further CNT growth. This problem can be overcome by creating a diffusion barrier on the substrate using an oxide

## 1.2. CNT SYNTHESIS BY FCCVD

---

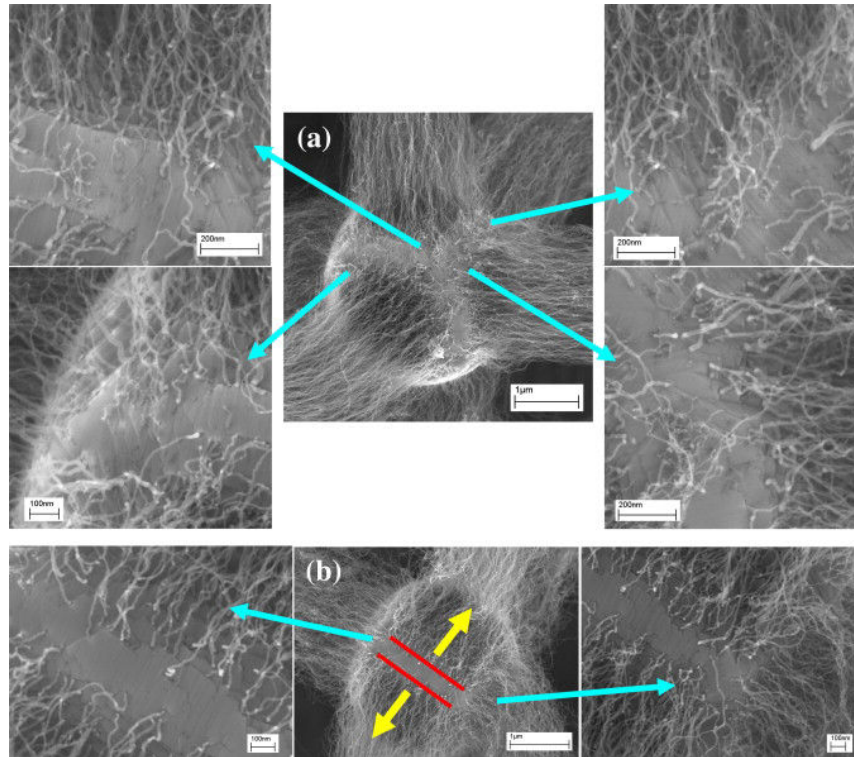


**Figure 1.16.** SEM images of the six-branch hybrid structure consisting of CNTs and heat-treated  $\mu\text{Al}_2\text{O}_3$  [158].

layer (like thermally oxidized  $\text{SiO}_2$ ,  $\text{MgO}$ ,  $\text{ZnO}$ ,  $\text{TiO}_2$  or  $\text{Al}_2\text{O}_3$ ).

Finally, the CNT growth direction is also related to the crystallographic orientation of the exposed substrate surface. Su et al. observed SWCNT growth horizontally on silicon support surface take preferred orientations depending on the lattice geometry of the support [162]. CNTs preferentially grow at  $90^\circ$  on Si (100) surface, but at  $60^\circ$  on Si (111) surface. Similar results were observed during the CNT growth on MgO. It was found that  $\text{MgO}(001)$  surface shows preferential growth of CNTs along (110) direction [163].

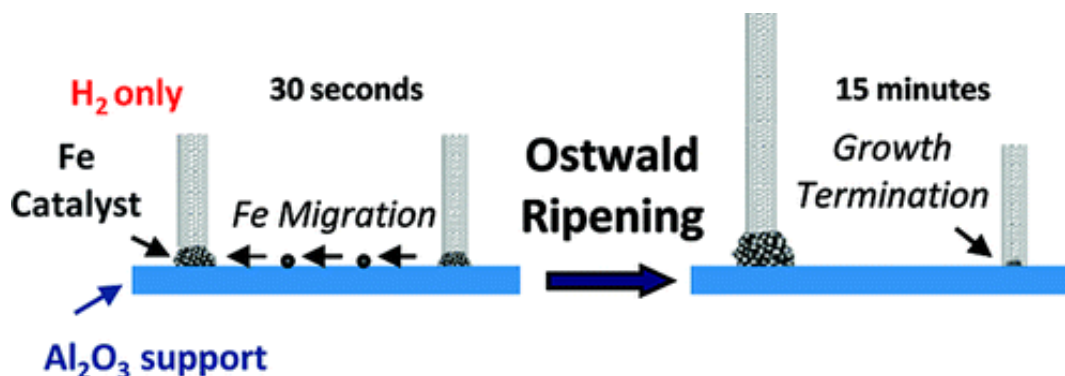


**Figure 1.17.** Schematic representation of the Ostwald ripening mechanism of catalyst during CNT growth by thermal CVD [159].

#### MECHANISM IN FCCVD

The growth mechanism of CNTs in FCCVD follows the general mechanism as a common CVD process. Both base growth and tip growth mechanisms of CNTs have been observed in FCCVD. Even the growth model that combine tip and base growth was reported by some groups [164–166]. But CNT growth in FCCVD is obviously more complex than the supported catalyst case where catalysts are pre-deposited. Although CNT growth in FCCVD always occurs on a substrate, the models developed for supported catalysts can not fully describe the CNT growth by FCCVD [167].

In FCCVD the catalyst precursor decomposition releases both metal atoms and reactive carbon species. It is difficult to trace catalyst evolution in experiments. Therefore, catalytic nanoparticles formation mechanism is highly debated. Two possible situations are frequently discussed. In the first case, the as-formed suspended catalyst nanoparticles in the gas phase being spherically shaped to minimize their surface energy would be gradually deposited on the substrate. And finally the CNT nucleation and growth will occur on the substrate. Whether further reactions like aggregation or coalescence will

occur or not on the substrate depends on their sizes and nature. Since the catalytic nanoparticles originate from decomposition of ferrocene in the gas phase, homogeneous nucleation was proposed as one possible mechanism for iron nanoparticle formation. Moysala et al demonstrated that thermal decomposition of ferrocene will result in formation of supersaturated metal vapour in the reactor, enabling nucleation and growth of iron nanoparticles via condensation and coagulation in the gas phase due to the very low iron saturated vapour pressure [168]. Castro et al. found that the change in iron vapor pressure has a great influence on CNT growth efficiency and diameter. They further deduced that homogeneous nucleation is the dominant mechanism for iron-based particle formation in gas phase [169]. Zhang et al. successfully modulated the diameter of CNTs by controlling the concentration of the iron atom at the initial rate. It reinforces the hypothesis of homogeneous nucleation of iron nanoparticles in the gas phase [170]. Castro et al. also found the strong correlation between the size and the number density of nanoparticles can be well explained by the homogenous nucleation hypothesis, which further underlines the importance of controlling the homogeneous nucleation of catalytic particles [171]. Based on the homogeneous nucleation hypothesis, the formation process and the growth rate of nanoparticles from thermal decomposition of ferrocene were simulated by computational fluid dynamics (CFD) methods [172–174]. These simulation results explained the experimental observations that the diameter of iron nanoparticles increases with the increase in the temperature and the ferrocene concentration. However, the above-mentioned results are based on speculations or indirect evidences. Furthermore, CFD simulatitons predicted that the size of catalytic iron nanoparticles will increase along the reactor axis, while, the results in the study on position-dependent growth of MWCNTs on alumina

microparticle contradict this prediction [175]. In addition, all the nanoparticles are considered as pure iron in the CFD models, but whether the nanoparticles in the gas phase are pure iron or not is still needed to be confirmed. In the second case, the *in-situ* formed CNT 'embryos' in the gas phase would reach to the substrate and elongate following the tip or the root growth model. We should find the longer CNTs on the substrate while the shorter CNTs in the gas phase. A recent study reported the simultaneous growth and separation of both SWNTs and MWNTs during the same CVD synthesis. The MWNTs formed on the substrate, whereas the SWNTs spontaneously originated in the gas phase [176]. Chen et al. also reported that CNT morphology can transfer from large-diameter MWNT arrays to SWNT films by adjusting the temperature. They postulated that MWNT arrays should grow by the catalysts nucleation on the surface of the substrate, while SWNT films grew by the catalyst particles directly nucleated in the gas flow (see Fig. 1.18) [177]. Therefore, the early stages of CNT growth are still under debate. [177]

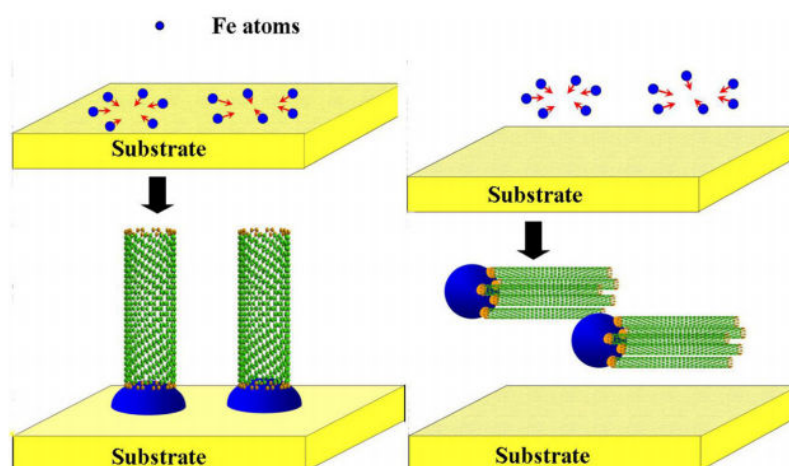


**Figure 1.18.** Sketch map of catalyst landing status for the growth of MWNT arrays and SWNT films via FCCVD process [177].

## 1.3. LASER-INDUCED INCANDESCENCE

---

### 1.3 LASER-INDUCED INCANDESCENCE

#### 1.3.1 LII HISTORY

LII phenomenon occurs when a high-energy pulsed laser beam encounters particular particles like soot or carbon black. When particles are heated up by a short laser pulse of a few nanoseconds duration, their temperature increases immediately ( $\sim 4000$  K). Meanwhile, the particles lose energy by heat transfer mechanisms. The thermal radiation leads to the LII phenomenon. LII could produce 50 ns to 1  $\mu$ s long light pulses. The research on LII was first outlined by Weeks and Duley in 1974 [178]. It was found that the aerosol particles generated from sub-micron powders of carbon black and alumina released a momentary emission of light when heated by TEA CO<sub>2</sub> laser pulses. And the spectrum of this emission related to the particle size. In 1977 Eckbreth found several interferences during the Raman scattering experiments, which were identified to be laser modulated particulate incandescence [179]. They proposed an analytical model to describe this process, which displays fair agreement with experimental results. Triggered by these results, a series of works had been made on LII. The real pioneer of LII technique is Melton. In 1984 Melton improved the equations governing the laser heating and vaporization of particles [24]. This work exploited the potentiality of LII as a powerful diagnostic tool for soot concentration measurement and particle sizing. A time-resolved variant of LII (TR-LII) was introduced to allow particle sizing by recording the time-dependent particle emissions during particle cooling after the laser heating by Roth [180, 181] and Will [25, 26]. These results have been validated by the TEM observations [182]. In the past decades LII had undergone significant developments. Following the earlier modeling work of Weeks and Duley [178], different detailed models were

developed to serve as means to extend this technique to a wider variety of conditions, including high pressures and low temperatures [183–189]. In 2002 R. Vander Wal et al. first applied LII to study the CNT flame synthesis [190]. Snelling and coworkers developed the auto-compensating LII. This technique can archive a quantitative measurement of volume fraction without further calibration process by using another soot measurement technique [191, 192]. The early experiments about LII focus on soot size measurements [24–27]. Due to its non-intrusive, real-time and *in-situ* nature, it has recently been spread to a variety of a range of sources, such as Cu [29], Ti [30], and Fe [31, 32], and Fe-C binary nanoparticles [33, 34]. Nowadays, LII has proven to be a powerful tool for particle concentration and primary particle size measurement and was used in a wide range of applications, such as combustion, particle synthesis and environment. However, this technique is rarely applied for the CNT growth. The mechanistic investigation of carbon nanotube formation was examined by Cau et al. within the framework of laser vaporization [193]. Recently Yatom et al. also conducted laser-induced incandescence measurements in the carbon arc discharge for synthesis of CNTs [194]. However, the synthesis of carbon nanotube by laser vaporization and carbon arc discharge are arguably different than CNT growth by floating catalyst CVD.

### 1.3.2 LII MODEL DESCRIPTION

The LII model is constructed based on the laws of conservation of energy and mass during heating by the laser pulse and subsequent cooling of a spherical nanoparticle, which is outlined in a number of publications [24, 27, 195–199]. The rates of heat and mass transfer are modeled by two time-dependent differential equations, one is the energy conservation equation and the other one is

### 1.3. LASER-INDUCED INCANDESCENCE

---

mass conservation equation. The energy conservation equation and the mass conservation equation for an individual spherical particle imposed to the absorption of light are written as

$$\frac{d(m_p c_p T_p)}{dt} = q_{\text{abs}} - q_{\text{rad}} - q_{\text{cond}} - q_{\text{evap}} \quad (1.5)$$

$$\frac{dm_p}{dt} = -J_{\text{evap}} \quad (1.6)$$

where  $m_p$  and  $c_p$  are the mass and the heat capacity of nanoparticles, respectively;  $T_p$  is the current temperature of nanoparticles;  $t$  is time;  $q_{\text{abs}}$  is the laser energy flux absorbed by nanoparticles;  $q_{\text{rad}}$  is the radiation energy flux from the surface of a nanoparticle;  $q_{\text{cond}}$  is the energy flux during convective heat transfer;  $q_{\text{evap}}$  is the energy flux from the surface of the nanoparticle during evaporation.  $J_{\text{evap}}$  is the mass loss rate from the particle surface in evaporation process. The main energy transfer processes are presented schematically in Fig. 1.19. The nanoparticle energy absorbed by laser pulse heating is consumed by thermal radiation as incandescence light, convective heat transfer with the molecules of surrounding gas, and evaporation of the substance on the surface of nanoparticles. In order to simplify the model, the nanoparticles are assumed to be spherically shaped, which do not result in significant deviations in describing radiation. Some other heat transfer processes, such as oxidation, molecular arrangement etc., have been neglected. Because these kinds of heat loss are relatively too weak in our experiment conditions [186, 200].

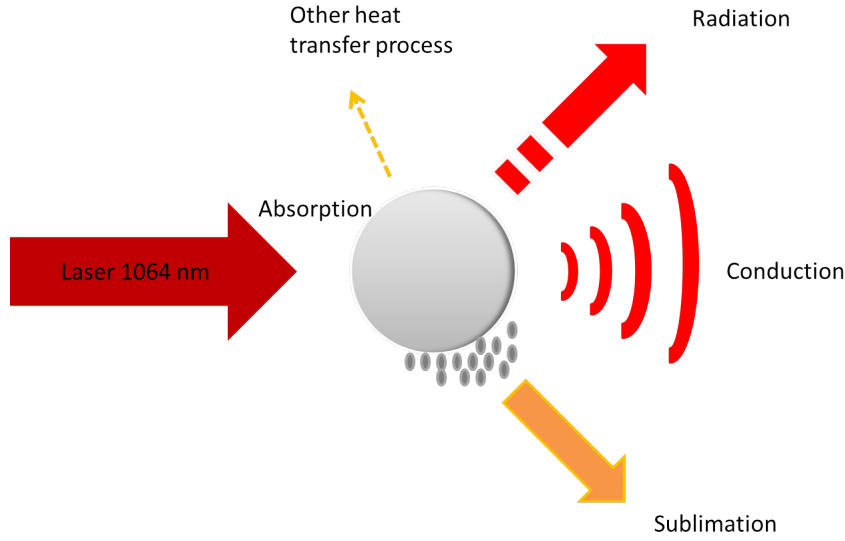


**Figure 1.19.** Heat exchange diagram during laser pulse heating.

The absorption of electromagnetic radiation by a particle in the Rayleigh limit is described by the equation

$$q_{\text{abs}} = E(m) \cdot q(t) \cdot \frac{\pi^2 d_p^3}{\lambda_{\text{laser}}} \quad (1.7)$$

where  $E(m)$  is the particle refractive index;  $q(t)$  refers to the laser profile (a gaussian temporal profile was used);  $d_p$  describes the particle diameter;  $\lambda_{\text{laser}}$  is the laser wavelength.

Different models for describing the heat fluxes due to heat conduction exist, which are classified according to the Knudsen number. The Knudsen number is the key system parameter, which is equal to the ratio of the free path of particles to the typical particle size

$$Kn = \frac{l}{d_p} \quad (1.8)$$

In the studied conditions, the Knudsen number is significantly higher than one, which indicates that the heat and mass transfer proceed in the free molec-

### 1.3. LASER-INDUCED INCANDESCENCE

---

ular regime. The heat flux from the nanoparticle surface can be expressed as [201]

$$q_{\text{cond}} = \alpha_T \pi \frac{d_p^2}{8} p_g c_t \frac{\gamma + 1}{\gamma - 1} \left( \frac{T_p}{T_g} - 1 \right) \quad (1.9)$$

where  $\alpha_T$  is the thermal accommodation coefficient (TAC) of the energy of ambient gas molecules at the surface of a nanoparticle;  $c_t = \sqrt{\frac{8RT_g}{\pi\mu_g}}$  is the average thermal velocity of gas molecules;  $p_g$  is the gas pressure;  $R=8.3145\text{J/molK}$  is the universal gas constant;  $\mu_g$  is the molecular weight of ambient gas molecules;  $\gamma = \frac{c_{pg}}{c_{pg}-R}$  is the ratio of the heat capacities of the gas;  $c_{pg}$  is molecular heat capacity of the gas;  $T_g$  is the temperature of the surrounding gas. The value of TAC is the main parameter for calculating convective heat exchange in the free molecular regime.

The Stefan-Boltzmann law is used to calculate the thermal radiation heat loss from the particle surface in all spectra range.

$$q_{\text{rad}} = \pi d_p^2 \cdot \varepsilon \cdot \sigma_{SB} (T_p^4 - T_g^4) \quad (1.10)$$

where  $\sigma_{SB} = 5.6704 \times 10^{-12} \text{W/cm}^2 \text{K}^4$  is the Stefan-Boltzmann constant.  $\varepsilon$  is the emission coefficient of nanoparticles. As the heat loss form radiation is usually relatively low comparing to the heat loss from conduction and sublimation [202].  $\varepsilon$  is assumed to be 1 in this study to simplification.

In the LII model heat losses by the particle evaporation becomes very important when heating proceeds to temperatures higher than the evaporation temperature, the evaporative cooling rate is represented as

$$q_{\text{evap}} = -\frac{\Delta H_v}{W_v} \frac{dm_p}{dt} \quad (1.11)$$

$$\frac{dm_p}{dt} = -\pi d_p^2 p_v \sqrt{\frac{W_v}{2\pi R T_p}} \quad (1.12)$$

where  $\Delta H_v$  is the average enthalpy of formation of sublimed species,  $W_v$  is the average molecular weight of sublimed species. The pressure of the vapor over the particle surface  $p_v$  is calculated by means of the Clapeyron-Clausius equation [203],

$$p_v = p_{\text{ref}} e^{-\frac{\Delta H_v}{R} \left( \frac{1}{T_p} - \frac{1}{T_{\text{ref}}} \right)} \quad (1.13)$$

where  $p_{\text{ref}}$  and  $T_{\text{ref}}$  are the the temperature and pressure at some point at the evaporation curve.

For carbon nanoparticles, the contribution of carbon clusters  $C_1$ - $C_{10}$  to the heat losses through evaporation has been analyzed by Michelsen et al. [187]. It is assumed that all clusters carried away from the carbon nanoparticle surface are  $C_3$  clusters ( $W_v = 36$  g/mol), since the contribution of  $C_3$  clusters to the flow of the substance carried away is dominant comparing to the contribution of the rest [204]. The evaporation enthalpy value in this model is taken as  $\Delta H_v = 7.78 \times 10^5$  J/mol. In order to determine the value of carbon vapor over the surface of carbon nanoparticles, data on graphite  $p_{\text{ref}} = 1$  atm and  $T_{\text{ref}} = 3915$  K are used in Clapeyron-Clausius equation. For iron particles, In simulating the heat exchange of iron particles with the ambient gas environment, it is assumed in this model that iron atoms are carried away from the surface of particles in evaporation. In order to determine the pressure over the nanoparticle surface, thermodynamic data on solid iron are used,  $p_{\text{ref}} = 3337$  Pa,  $T_{\text{ref}} = 2500$  K, and  $\Delta H_v = 3.76 \times 10^5$  J/mol.

Two-color Pyrometry was applied to determine the maximum heating temperature of nanoparticles by the laser pulse [27, 205, 206]. Under the assumption that the radiation density is governed by the Planck law with known emissivity values of nanoparticles at the chosen wavelengths, the exact maximum temperature value of nanoparticles can be determined. The following expression is

### 1.3. LASER-INDUCED INCANDESCENCE

---

used to determine nanoparticle emission coefficient in the Rayleigh limit

$$\varepsilon(\lambda) = \frac{4\pi d_p E(m)}{\lambda} \quad (1.14)$$

For simplification, we assume that the energy distribution along the diameter of the laser beam is homogeneous, all particles achieve the same temperature. Then the incandescence signal detected at wavelength  $\lambda$  is determined by the relation

$$S = K \frac{\pi^2 d_p^2 h c^2 \varepsilon(\lambda)}{2\lambda^5} \left( e^{\frac{hc}{\lambda k_B T_p}} - 1 \right)^{-1} \quad (1.15)$$

where  $h$  is Planck constant;  $c$  is the velocity of light in vacuum;  $k_B$  is the Boltzmann constant;  $K$  is the calibration constant characterizing the parameters of the recording system. Application of Eq. (1.15) to the relation of maximum radiation intensities at two different wavelengths  $\lambda_1$  and  $\lambda_2$  gives the relation for the maximum heating temperature of nanoparticles:

$$T_p^0 = \frac{hc}{k_B} \frac{\left( \frac{1}{\lambda_2} - \frac{1}{\lambda_1} \right)}{\ln \left[ \frac{S_1 \cdot K_2 \cdot \varepsilon(\lambda_2) \cdot \lambda_1^5}{S_2 \cdot K_1 \cdot \varepsilon(\lambda_1) \cdot \lambda_2^5} \right]} \quad (1.16)$$

where  $S_1$  and  $S_2$  are the LII signals.  $\lambda_1$  and  $\lambda_2$  are the two selected detection wavelengths (in this study they are 492 nm and 694 nm).  $\varepsilon(\lambda_1)$  and  $\varepsilon(\lambda_2)$  are the emission coefficients. For small particles in the Rayleigh limit, the ratio of emissivities of nanoparticle can be approximated by [207]

$$\frac{\varepsilon(\lambda_2)}{\varepsilon(\lambda_1)} \sim \frac{\lambda_1}{\lambda_2} \quad (1.17)$$

$K_1$  and  $K_2$  are the calibration constants for each of the two wavelengths, which can be experimentally determined.  $K_1/K_2$  represents the spectral sensitivity of the detection system at the two wavelengths 1 and 2. The  $K_1/K_2$

is known for a fixed detection system. Then the system can be calibrated using a blackbody source of the known temperature. So we have

$$T_p^0 = \frac{hc}{k_B} \frac{\left(\frac{1}{\lambda_2} - \frac{1}{\lambda_1}\right)}{\ln \left[ \frac{S_1 \cdot K_2 \cdot \varepsilon(\lambda_2) \cdot \lambda_1^5}{S_2 \cdot K_1 \cdot \varepsilon(\lambda_1) \cdot \lambda_2^5} \right] + \frac{hc}{k_B T_{BB}} \left(\frac{1}{\lambda_2} - \frac{1}{\lambda_1}\right)} \quad (1.18)$$

where  $S_{BB}$  is the signal from a blackbody source at the temperature  $T_{BB}$ .

In the present work, the particle temperature as a function of cooling time can be calculated by solving the differential Eqs. (1.5) and (1.6) with the heat-up temperature  $T_0^p$  as an initial value. A fourth order Runge-Kutta algorithm was implemented for this purpose. The intensity of incandescence on the detected wavelength from a single spherical particle with known temperature is determined by an expression based on the Planck law [180, 181].

$$S_d(t) = C \left[ \frac{d_p^3(t)}{\exp\left(\frac{\chi T_g}{T_p(t)}\right) - 1} - \frac{d_{p0}^3}{\exp(\chi) - 1} \right] \quad (1.19)$$

where  $\chi = \frac{hc}{\lambda k_B T_g}$ , and  $d_{p0}$  is the initial nanoparticle size before evaporation. Eq. (1.19) is relevant for a particle ensemble of uniform  $d_{p0}$ . It is known that nanoparticles from synthesis processes obey a certain size distribution. In the present work, a log-normal size distribution for the particles is assumed, which is most commonly satisfied for statistical process descriptions [208–210]. The expression for log-normal function is written as

$$df = \frac{1}{\sqrt{2\pi} d_p \ln \sigma_g} \exp \left[ -\frac{(\ln d_p - \ln CMD)^2}{2 (\ln \sigma_g)^2} \right] dd_p \quad (1.20)$$

where  $CMD$  is the count median diameter of nanoparticles.  $\sigma_g$  is the geometrical deviation from the mean size. Then the signal from an ensemble of

#### 1.4. CONCLUSION

---

nanoparticles with a size distribution obeying Eq. (1.20) is given by

$$S(t) = \int_{d_1}^{d_2} S_d(t) df \quad (1.21)$$

Finally, the measured LII signals were evaluated in terms of particle size by fitting calculated LII curves to the experimental profiles under variation of  $CMD$  and  $\sigma_g$  by a least-squares method [211]. For comparison purposes, the geometric standard deviation  $\sigma_g$  was also obtained by approximating the histograms of nanoparticles distribution measured by TEM micrographs using the log-normal function in some cases.

#### 1.4 CONCLUSION

In this Chapter, we reviewed some basic knowledges of CNTs, such as the history and their structures. And then various CNT synthesis routes were discussed. Among them, the detailed description of FCCVD were presented due to its large-scale production of well-controlled CNTs. The state of the art research of CNT growth mechanism was reported. The main questions in current research on CNT growth were listed. The importance of the study on nanoparticle formation in the gas phase during FCCVD were underlined. Moreover, an *in-situ* diagnostic technique LII was mentioned. LII has been recognised as one of the most promising techniques for *in-situ* quantitative measurements of particle size and distribution. The history, basic physical principle and mathematic model of LII were all discussed in details. It could be found that the LII technique could be a very useful tool to achieve a non-intrusive, real-time and *in-situ* diagnostic for the nanoparticle sizing during FCCVD process.

In the next part of this research, Chapter 2 will introduce the FCCVD process used in this research and present the different characterization techniques to study the CNT growth mechanism. Then, Chapter 3 will present the evolution of nanoparticles in the gas phase along the reactor axis at different CVD conditions by *in-situ* diagnostic technique LII. Chapter 4 will study the roles of the substrate and the influence of its features on the CNT morphology and yield. The roles of nanoparticles during FCCVD process will also be discussed. Finally, Chapter 5 will summarize this research and provide some perspectives for further investigations.

# 2

## Experimental procedure

In this Chapter, the FCCVD process for CNT growth, including the materials and equipments, are presented. Various diagnostic methods during/after FCCVD process are described. The *in-situ* characterization methods, including LII, thermocouple, etc., are used to obtain the information real-timely. After CNT synthesis samples are also analyzed by the *ex-situ* characterization methods, including microscope, Raman, Thermogravimetric Analysis (TGA) etc.

### 2.1 CNT GROWTH BY FCCVD

#### 2.1.1 MATERIALS

The main materials involved in this study are listed in Table 2.1. Argon (Ar, 99.8 % purity) was used as the protection gas. Ferrocene was also applied as the catalytic precursor due to its good stability, low cost and non-toxicity [212]. High purity hydrogen (99.99%) with levels of 0.1 ppm O<sub>2</sub> and 0.5 ppm H<sub>2</sub>O was utilized in this study. H<sub>2</sub> was also used since suitable content of H<sub>2</sub> leads to an

**Table 2.1.** Information of the main materials used in this research.

Materials	Formula	States	Origin
Argon	Ar	Gas	Air Liquide
Acetylene	C <sub>2</sub> H <sub>2</sub>	Gas	Air Liquide
Hydrogen	H <sub>2</sub>	Gas	Air Liquide
Ferrocene	Fe(C <sub>5</sub> H <sub>5</sub> ) <sub>2</sub>	Solid	Alfa Aesar
Xylene	C <sub>8</sub> H <sub>10</sub>	Liquid	Alfa Aesar
Alumina	μAl <sub>2</sub> O <sub>3</sub>	Solid (Size in 3-10 <i>um</i> )	Perf. Ceramics Comp.

augmentation in carbon supply by promoting the decomposition of hydrocarbon vapors into more reactive byproducts [213, 214]. Acetylene was also provided to the system to accelerate the synthesis of CNTs [215–217]. CNTs were synthesized onto two different substrates: quartz plates and micro-spherical alumina particles μAl<sub>2</sub>O<sub>3</sub>, size ranging in 3-10 μm, with 99.8 % purity including 800 ppm SiO<sub>2</sub>, 600 ppm Na<sub>2</sub>O. The μAl<sub>2</sub>O<sub>3</sub> particles exhibit a multiphase crystallographic structure, containing mostly the thermodynamically stable hexagonal αAl<sub>2</sub>O<sub>3</sub>, and to a lesser extent metastable tetragonal δ and monoclinic θ phases. It is also worth noting that no evident phase-transformation occurred when the μAl<sub>2</sub>O<sub>3</sub> particles were heated at temperatures up to 800 °C [158].

### 2.1.2 FCCVD PROCESSES

CNTs were synthesized by the FCCVD process. The schematic of the overall CVD system in our experiments is presented in Fig. 2.1. The solid-state catalyst precursor ferrocene was first dissolved into the carbon source solvent xylene. Then the solution was injected into the reactor by a spray, which contains two concentric tubes of 0.5 mm diameter, one for gas and the other for liquid, as depicted in Fig. 2.2. The liquid flow was controlled by an electronic syringe system (Razel Science, R99-E), while the gas flows were monitored by

## 2.1. CNT GROWTH BY FCCVD

---

thermal electronic gas flow meters (Brook Smart). During the spray process, the solution will be brought into the reaction zone by the production of small droplets. In order to achieve a good vaporization of the spray, the speed of gas flow should be rationally controlled. It should not be too low or too high, since too low gas flow will result in a bad dispersion of the liquid, while an excessive flow rate would induce a recirculation in the reactor. The total gas flow rate was kept to 1 L/min during the whole process, which can make sure a good dispersion of the liquid.

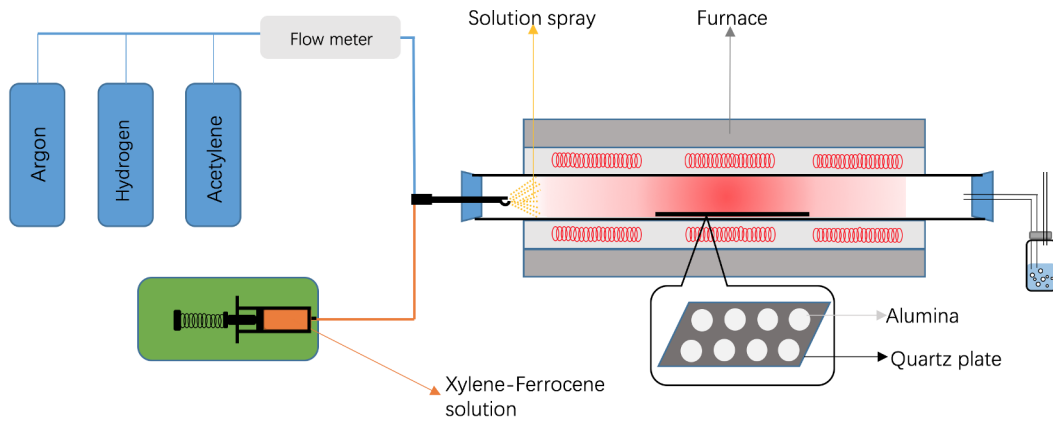


**Figure 2.1.** Schematic of the CVD system used in this research.

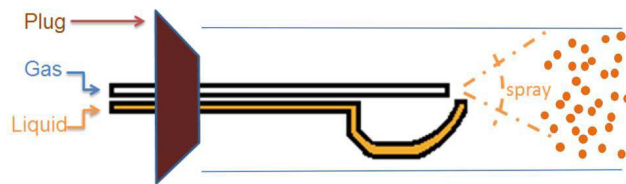


**Figure 2.2.** Schematic of the solution spray in the CVD system.

The CNT synthesis was carried out by FCCVD in a reactor. The equipment used in FCCVD is typically a horizontal quartz tube heated by an electric furnace. However, in this situation NPs inevitably deposited on the inner wall

of the quartz tube due to the high temperature, which disturbs LII signals from NPs floated in the gas phase. Therefore, a 'real' *in-situ* detection of NPs suspended in the gas phase was very difficult. Alternatively, a stainless steel reactor with seven 15-cm long stainless steel open-ended tubes (6.3 mm in diameter) welded perpendicular to the reactor axis was designed in our experiments and the gas exhaust was probed by laser-induced incandescence at the end of each 15-cm long tubes, as depicted in Fig. 2.3. And then we conducted a validation experiment inside the reactor, where a TEM grid was placed into the tube furnace. This comparative study revealed that there are no statistical differences in size and structure between the NPs inside the reactor and those collected at the location where the LII signal was probed. We further validated the accuracy of our LII method by comparing with TEM data. The good agreement between the LII and TEM sizing data demonstrate the validity of this approach in this case. In each CVD run, P5 was positioned in the center of the furnace. Quartz plates and micro-spherical alumina particles  $\mu\text{Al}_2\text{O}_3$  of 3-10  $\mu\text{m}$  in diameter were used as substrates for CNT synthesis. When  $\mu\text{Al}_2\text{O}_3$  particles was supported as the substrate, they were homogeneously dispersed on the surface of a quartz plate, which was put into the furnace. Then the furnace was heated up by an electrical resistance furnace (CARBOLITE) to a high temperature (from 650 to 850  $^\circ\text{C}$ ) under an argon atmosphere. The temperature at different positions along the CVD reactor were measured by the Testo-922 thermocouple. And the tube was kept well-sealed with 1 L/min argon flow during the measurements. The temperature profiles were measured along the wall of the tube at different set temperatures, as presented in Fig. 2.4 and in Table 2.2.

After the reactor was heated to the set temperature, hydrogen was intro-

## 2.1. CNT GROWTH BY FCCVD

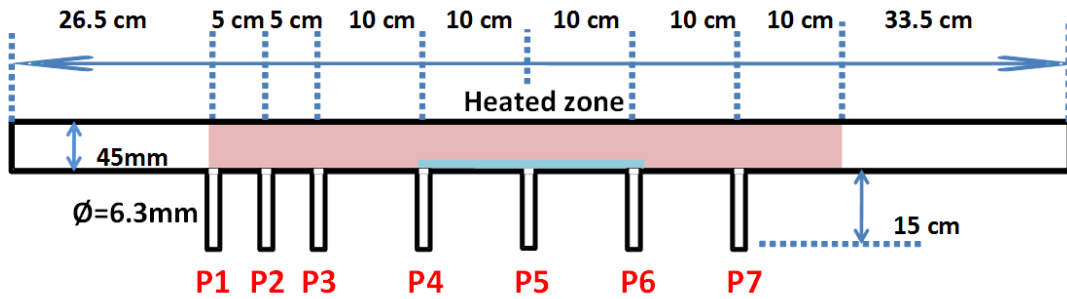


**Figure 2.3.** Schematic of the stainless steel CVD reactor with seven small open-ended tubes at different positions labeled as P1, P2, P3, P4, P5, P6 and P7 along the reactor.

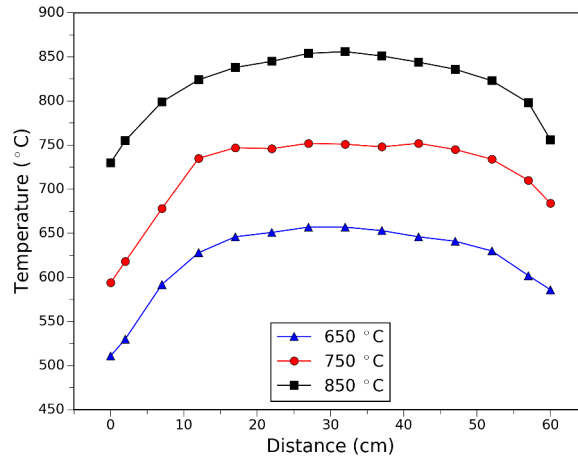


**Figure 2.4.** Temperature profiles along the reactor of the stainless steel tube at different set temperatures.

duced into the reactor. The total gas was composed of a mixture of argon and hydrogen with different ratios. And the total gas flow rate was kept at 1 L/min. This process lasted for about 20 min for equilibrium [218]. Yang et al. simulated the hydrogen percentage evolution as a function of time in the reactor. Results show that 20 min is enough to stabilize the system at a gas flow of 1.0 L/min, as shown in Fig. 2.5. The precursor solution consisted of a liquid feedstock of carbon source xylene with dissolved ferrocene (from 0.01 to 0.1 g/mL) was injected at 0.2 mL/min in the form of spray. Acetylene was

**Table 2.2.** Temperature values measured along the furnace at different set temperatures.

Distance (cm)	650 °C	750 °C	850 °C
0	501	584	682
2	511	618	755
7	592	678	799
12	628	735	824
17	646	747	838
22	651	746	845
27	657	752	854
32	657	751	856
37	653	748	851
42	646	752	844
47	641	745	836
52	630	734	823
57	602	710	798
60	556	638	720

also provided to the system at a rate of 0.02 L/min to accelerate the synthesis of CNTs [215, 216]. In general, the injection lasted for 12 min, except for some special situations. Nanoparticles at different positions were detected in order to investigate the evolution of nanoparticles in the gas phase. Finally, the injection of all carbon and catalytic sources was stopped and the reactor was cooled down to the room temperature under argon at 1.0 L/min. CNTs were collected on the substrate for characterizations.

## 2.2 CHARACTERIZATION METHODS

In this research, to investigate the evolution of nanoparticles in the gas phase and their roles during CNT growth. Different characterization techniques were used. They include the *ex-situ* characterization methods, such as microscope, Raman, TGA, et. al. Besides the *ex-situ* characterization methods, the *in-situ*

## 2.2. CHARACTERIZATION METHODS

---

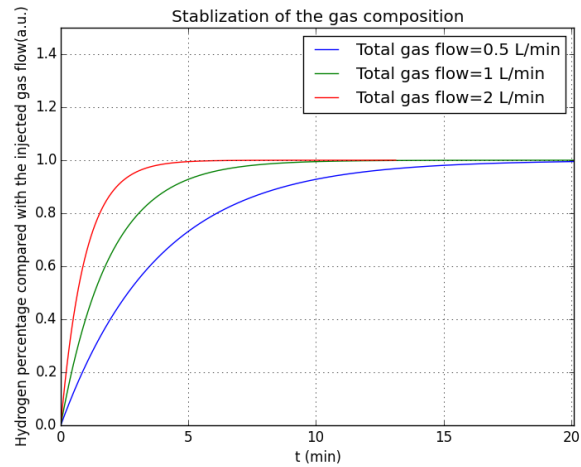


**Figure 2.5.** Simulation for the gas stabilization time [218].

characterization methods, such as LII, were also applied. These characterization methods, as well as their principles, are presented below.

### 2.2.1 ELECTRON MICROSCOPY

In this research, Scanning electron microscopy (SEM) was conducted on FEI Quanta 200 SEM instrument with an accelerating voltage of 5 kV. Transmission electron microscopy (TEM) was performed using a FEI Titan instrument equipped with an probe-corrected condenser operating at 200 kV. SEM was used to observe the CNT morphology. Samples were collected on the substrate after the CVD synthesis without any exaction. Due to the limited resolution of SEM, the diameter distribution should obtain by TEM observations. For CNTs synthesized on the substrate, TEM samples were prepared by dispersing a small number of as-synthesised nano-structures in ethanol. Brief ultrasonication was used to disperse CNTs, after which carbon-coated grids were immersed into the suspension and allowed to dry thoroughly. The typical SEM and TEM images of CNT structure are depicted in Fig. 2.6. For nanoparticles in the gas phase,

TEM grids were put directly at the outlet of the small open-ended tubes at the different positions along the reactor axis for about 5 s. For all the samples, a thorough statistical analysis of over 50 nanoparticles or tubes were conducted for each synthesis condition. The results were subjected to one-way analysis of variance (ANOVA). Statistical differences in CNT or tube diameter were determined with p-values smaller than 0.05. Our TEM system also was equipped with Energy-dispersive X-ray spectroscopy (EDS) analyse and selective area electron diffraction (SAED), which allow us to identify the structure, composition and crystallization of nanoparticles.

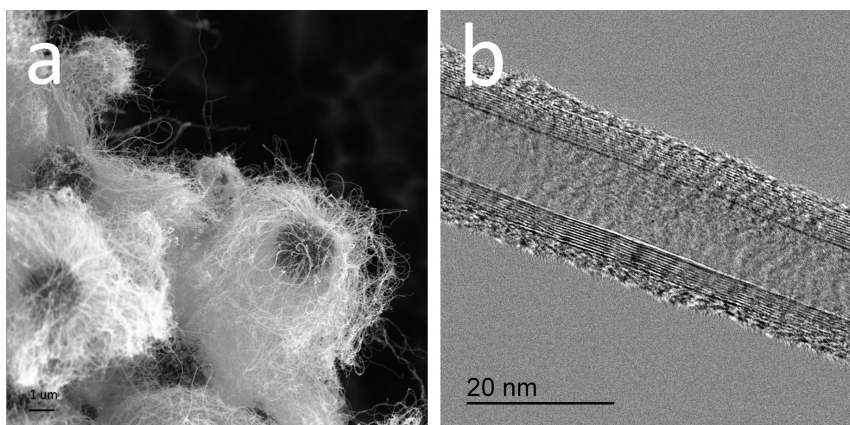


**Figure 2.6.** Typical (a) SEM and (b) TEM images of CNTs grown on  $\mu\text{Al}_2\text{O}_3$ .

### 2.2.2 THERMOGRAVIMETRIC ANALYSIS

Thermogravimetric analysis (TGA) was conducted using a Netzsch analyzer (STA449F3 Jupiter). During the analysis process, a thermogravimetric analyzer continuously measures the mass while the temperature of a sample increased from between 50 °C to 900 °C at a heating rate of 10 °C/min under an oxidizing atmosphere (flow rate of mixture of  $\text{N}_2$  and  $\text{O}_2$ , 20 ml/min: 20 ml/min). It can provide information about thermal the stability of products. Fig. 2.7 showed

## 2.2. CHARACTERIZATION METHODS

---

the typical TGA/DTG curves of CNTs- $\mu\text{Al}_2\text{O}_3$  hybrid samples. The main mass loss is attributed to the oxidation of carbon. The oxidation temperature for as-synthesized CNTs was in the range of 400-650 °C, while the weight loss at 350 °C was associated to the non-crystalline carbonaceous structures [79]. Therefore, TGA curve could be used to evaluate the ratio of carbon in the total production mass. The main reactions involved are presented below:

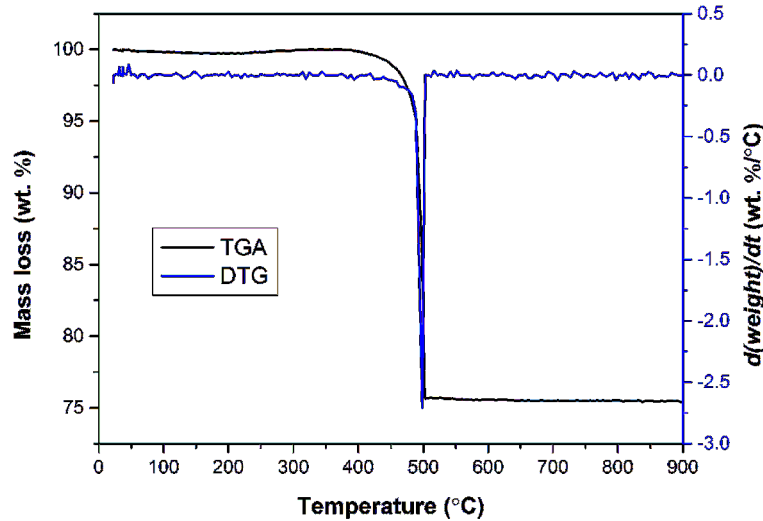
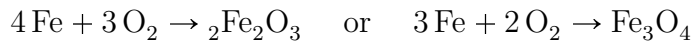
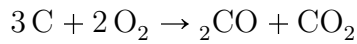


**Figure 2.7.** Example of the TGA/DTG curves for CNTs grown on the  $\mu\text{Al}_2\text{O}_3$  substrate.

### 2.2.3 RAMAN SPECTROSCOPY

The CNT-based samples were also characterized by Raman spectroscopy analysis, which was performed in the range of 1000-2000  $\text{cm}^{-1}$  by a Jobin Yvon LabRam spectrometer using the 632.8 nm emission of a He-Ne laser source. Fig. 2.8 shows the typical Raman spectrum of CNTs-based sample. CNT-based

samples display two first-order peaks near  $1330$  and  $1580\text{ cm}^{-1}$ , assigned to the D-bands and G-bands, respectively. The G-band is the characteristic peak for the stretching vibration of carbon  $sp^2$  bonds in a hexagonal lattice, and the D-band corresponds to the disordered  $sp^2$  phase plus possible contributions of the scattering of  $sp^3$ -bonded carbon [219]. For each sample, spectral noises and background broadband deformations are removed with the Savitzky-Golay smoothing procedure. The integrated intensity ratio of the G-band to the D-band ( $I_G/I_D$ ) is commonly invoked as a benchmark of the CNT crystallinity [220]. A lower  $I_G/I_D$  ratio thus suggests fewer structural defects in CNTs as well as higher purity.

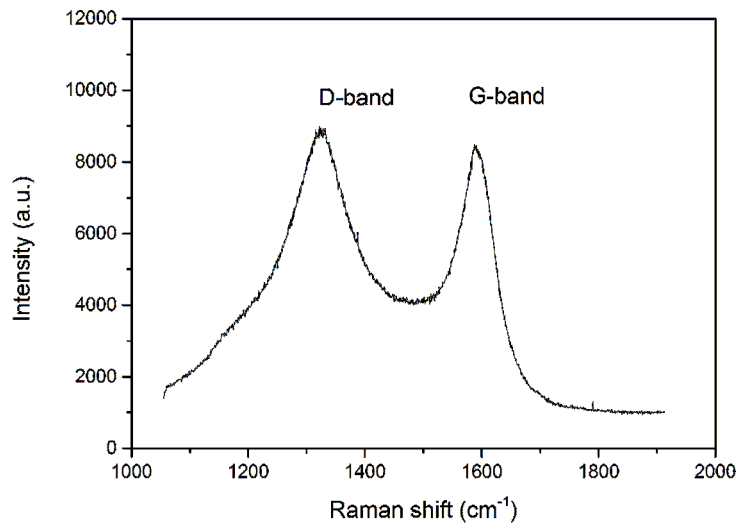


**Figure 2.8.** Example of the Raman spectrum for CNT samples growth on the quartz substrate.

#### 2.2.4 LII

During CNT growth, it is commonly recognized that the control of the size and morphology of iron catalytic nanoparticles is critical for high yield syn-

## 2.2. CHARACTERIZATION METHODS

---

thesis of CNTs with well-defined structures and properties [21, 22]. However, the catalyst formation mechanism is still not clear. Catalysts come from thermal decomposition of ferrocene in the gas phase. It is essential to monitor nanoparticle evolution in the gas atmosphere. So in this study a real-time diagnostic technique LII was applied for *in-situ* characterization of nanoparticles in the gas phase. The overall system for LII signal measurements is depicted in Fig. 2.9. Due to the difficulties of NP detection by LII sampling in the gas phase inside the reactor, the reactor was opened at seven positions using 15-cm long stainless steel tubes (6.3 mm in diameter) welded perpendicular to the reactor axis to provide optical access to the reactive atmosphere for LII analysis. And the gas exhaust was probed by laser-induced incandescence at the end of each 15-cm long stainless steel open-ended tubes. A pulsed 2 Hz Nd:YAG laser (Excel, Surelite II-10) generating at the wavelength of 1064 nm with a pulse duration of 7 ns and a beam diameter of about 7 mm is used as a source for heating nanoparticles. The laser energy has been measured by an energy meter (GENTEC-EO solo2 with a power detector UP19K-15S -VM-D0) at different Q-switch values. The laser pulsed 100 times, allowing the calculation of the average output laser energy. The energy fluence can be obtained by measuring the laser pulse interaction area with a flashpaper, reported in J/cm. The results of these measurements are summarized in Table 2.3.

In this research, Q-Switch Delay was fixed at 350 us, which makes sure a suitable LII signal in all CVD conditions. The pulse energy was measured to be 66.5 mJ per pulse, corresponding to a laser fluence of 0.19 J/cm<sup>2</sup>. Exposed to the laser pulse, the particle temperature increases sharply (nearly up to 3000 K within several ns) due to the energy absorption. Then the LII phenomenon occurs. In this process, the absorption is dominant for the particles heat trans-

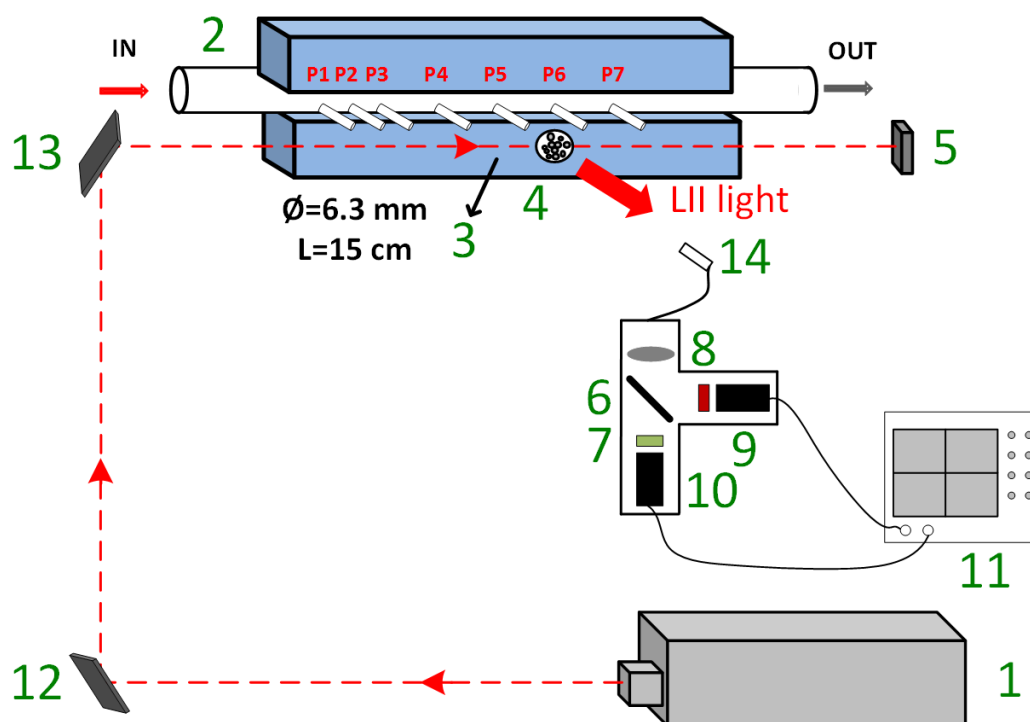


**Figure 2.9.** Experimental setup for LII measurements. 1. Nd:YAG pulsed laser (10 Hz, 1064 nm). 2. The stainless steel CVD reactor. 3. Small open-ended tubes installed at different positions along the reactor (P1-P7). 4. Area containing NPs (outlet of the small tube). 5. Laser energy meter. 6. 550 nm Dichroic shortpass filter. (7,8). Bandpass filter 492 and 694 nm. (9,10) Two PMTs. 11. Oscilloscope. (12,13). Reflection mirror. 14. Optic fiber.

**Table 2.3.** Laser Energy Measurements.

Q-Switch Delay ( $\mu\text{s}$ )	Laser Energy (mJ)	Fluence $\text{J}/\text{cm}^2$
260	295	0.84
270	238	0.68
280	227	0.65
290	179	0.51
300	154	0.44
310	145	0.41
320	123	0.35
330	94.7	0.27
340	78.4	0.22
350	66.5	0.19
360	55.2	0.16

## 2.3. CONCLUSION

---

fer. Once the laser pulse terminates, the particles will cool down due to the heat transfer such as conduction, radiation, evaporation. The optical detection system is composed of a 550 nm Dichroic Shortpass Filter, two Bandpass filters (492 and 694 nm) with 10nm FWHM (Edmund optics) and two high-speed photomultipliers (PMTs) (Hamamatsu, H10721-20) equipped with their amplifiers (Hamamatsu, C5594-44). The data then were written to a 2 GHz digital oscilloscope (Lecroy, Wavejet 354A). 5000 datum points were recoded for each LII event. Each LII curve was processed by the Savitzky-Golay smoothing procedure in order to remove noises [221]. The typical view of the LII signals are showed in Fig. 2.10. Finally the measured LII signals were evaluated in terms of particle size, by fitting the calculated light flux arriving at the detector surface to the experimental profiles using a least-squares method by Levenberg and Marquardt algorithm [211].

For comparison purposes, physical samples of the floating particles were collected at the outlet of each open-ended tube. Sampling was conducted by introducing copper grids at the positions where the LII signals were recorded. The copper grids were withdrawn after being exposed to the gas outlet for five seconds and used for TEM observation.

## 2.3 CONCLUSION

In this chapter, the experimental procedure of FCCVD process was first illustrated, including materials and equipments used in this research. And then *in-situ/ex-situ* characterization methods has been presented, specially, the setup of the LII detection system. The procedure of LII signal measurement and processing were emphasized. Table 2.4 below presents a summary for the

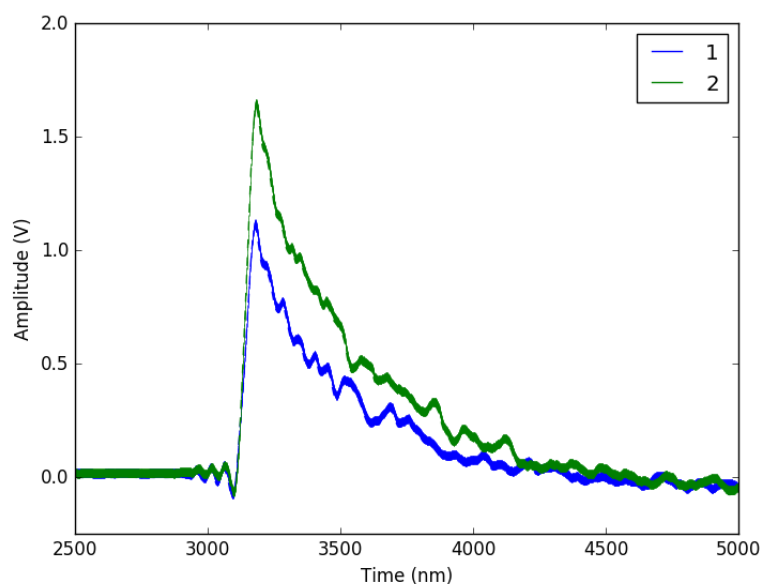


**Figure 2.10.** Typical view of incandescence signals. 1. 694 nm. 2. 492 nm.

mentioned characterization methods used in this study.

**Table 2.4.** List of the different characterization techniques in this research.

Techniques	Measured factors	Comments
LII	Suspended nanoparticle size	<i>In-situ</i>
SEM	CNT morphology	<i>Ex-situ</i>
TEM	Nanoparticle size, component and structure	<i>Ex-situ</i>
	CNT diameter	
TGA/DTG	CNT crystallization and yield	<i>Ex-situ</i>
Raman	CNT crystallization	<i>Ex-situ</i>

# 3

## Nanoparticles in the gas phase

In this Chapter, an *in-situ* diagnostic technique LII was applied for nanoparticle sizing during the FCCVD synthesis of CNTs. The theoretical LII signal was simulated by taking into account the nanoparticle nature, density, heat capacity and size distribution etc. A detailed sensitivity and uncertainty of the key parameters on the evaluated particle size for this model has also been estimated. And the model was validated by TEM. Using the developed approach, the evolution of the nanoparticles in the gas phase along the reactor axis was investigated at different CVD conditions.

### 3.1 IMPLEMENTATION OF LII

#### 3.1.1 MATERIAL PROPERTIES AND KEY PARAMETERS

##### NANOPARTICLE NATURE

The samples of nanoparticles were collected in the gas phase at the center of the reactor P5 at 850 °C with 0.2 mL/min of ferrocene dissolved into xylene

at 0.05 g/mL. The gas flow was composed of a mixture of 0.78 L/min Ag, 0.2 L/min H<sub>2</sub> and 0.02 L/min C<sub>2</sub>H<sub>2</sub>. The CVD process lasted for 12 min. And then nanoparticles were collected by putting TEM grid directly at the outlet of the small open-ended tubes for about 5 s. Then the samples were analyzed. The typical TEM image of nanoparticles are shown in Fig. 3.1a. In the TEM image the spherical particles 5-30 nm in size are found. The nanoparticles contain 3-10 graphite layers. And they exhibit a core-shell structure with an iron core and a carbon shell. For many particles, lattice fringes of the core material are visible, showing that they are crystals (Fig. 3.1b). The selected area electron diffraction patterns (EDP) analysis (Fig. 3.1a inset) indicates that the iron core is  $\alpha$ -Fe (ferrite, BCC,  $a=0.287$  nm).

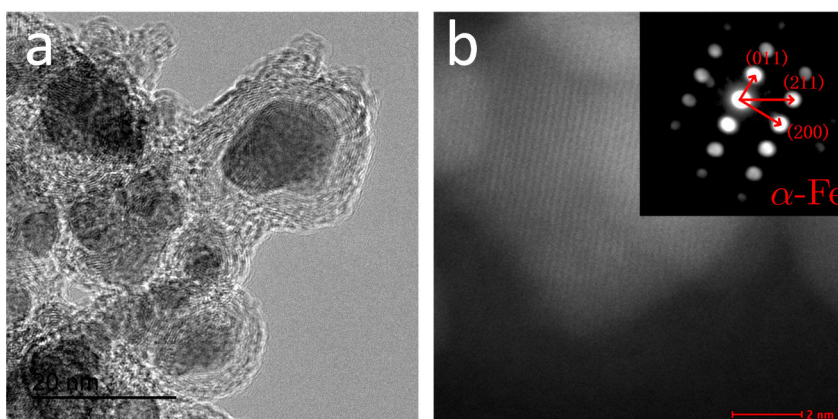


**Figure 3.1.** (a) High resolution TEM image of nanoparticles the center of heated zone (P5). (b) STEM image shows the lattice fringes of the iron core of nanoparticles at P5. (Selected area electron diffraction patterns (EDP) in the iron core region is shown in inset.)

In addition, the elemental analysis of nanoparticles in the samples was carried out by EDS. The spectrum of chemical elements and the map distribution of the elements in nanoparticles are presented in Fig. 3.2. From the spectrum of elements (Fig. 3.2a), it can be seen that copper, silicon, iron and carbon

### 3.1. IMPLEMENTATION OF LII

---

elements are detected. The peaks around 1.0 and 8.0 and 9.0 keV correspond to copper, resulting from the copper grid used for nanoparticle support. The peak around 1.8 keV, corresponding to silicon element, is probably related to impurities from the quartz during sampling. The weak peak intensity shows that silicon element is in low quantity. The peaks around 0.6 and 6.4 keV correspond to iron element, which comes from the iron core of nanoparticles. The high angle annular dark field scanning transmission electron microscopy (HAADF STEM) was also performed. The STEM image is shown in Fig. 3.2b, and the map of spatial distribution of iron and carbon elements in the samples is presented in Fig. 3.2c,d. We can see a high concentration of iron element, which distributes mainly in the center of nanoparticles. Owing to the TEM grid covered by the thin carbon layer for nanoparticle support. The presence of carbon element peak in all samples is presumably related to the carbon cover on copper TEM grids or graphite layers around iron core. However, according to the map of spatial distribution of iron and carbon, there are always some carbon elements around the iron core at suspended region in the sample. This is the direct evidence of the presence of amount of carbon content in the nanoparticles, which is in a good agreement with TEM image (see Fig. 3.1a).

The histogram of particle size distribution is presented in Fig. 3.3b. It was fitted by a log-normal size distribution by the least-squares method. The obtained count median diameter  $CMD$  and standard deviation  $\sigma_g$  in this case are found to be 11.7 nm and 1.31 correspondingly. In the present model standard deviation  $\sigma_g$  is assumed to be constant at 1.31. Since the evaluated mean particle diameter is only slightly biased by the choice of the standard deviation [31, 222].

According to above observations, a majority of nanoparticles formed in the

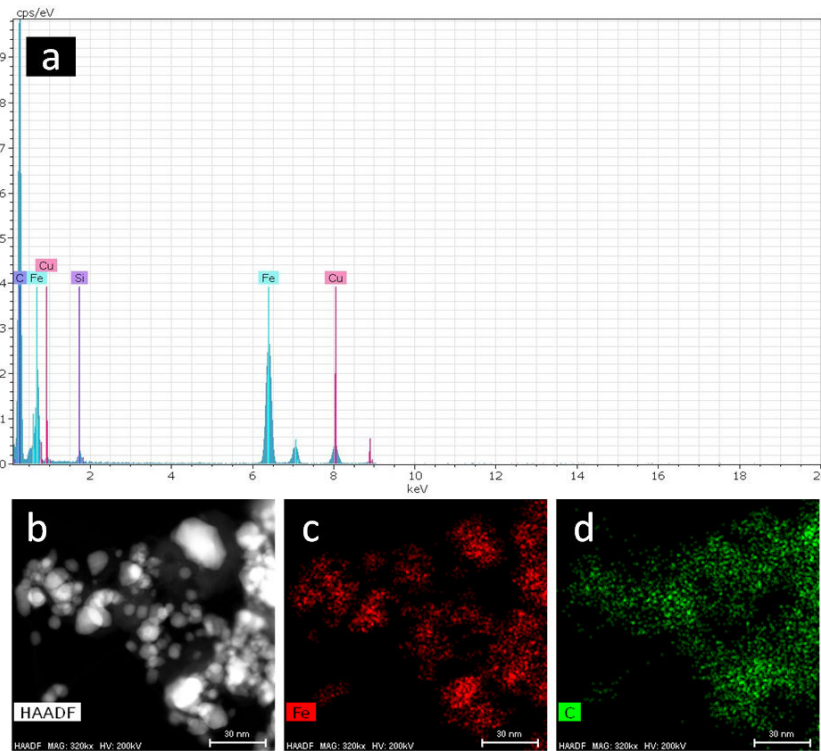


**Figure 3.2.** (a) Spectrum, (b) STEM image and (c,d) map distribution of chemical elements in the sample of nanoparticles obtained at the center of the heated zone (P5).

gas phase during CVD process exhibit a core-shell structure with an iron core and a carbon shell. Therefore, for implementation of LII sizing to binary particles, the procedure of the calculation of the theoretical LII signal was adjusted relatively to that applied to monocomposite nanoparticles. It is a quite complicated task to take into account the effect of thermo-physical properties of nanoparticles by the carbon layers in the LII model. The investigation of the thermo-physical properties of this kind of nanoparticles is out of the goal of this study. Therefore, we simply use the density ( $\rho_p=7700 \text{ kg/m}^3$ ) and heat capacity ( $c_p=0.65 \text{ J/gK}$ ) of bulk iron in this model [31, 223, 224], since the total mass of nanoparticles presumably comes from the iron core. According the TEM images, for a nanoparticle with 60% iron core in diameter, the mass

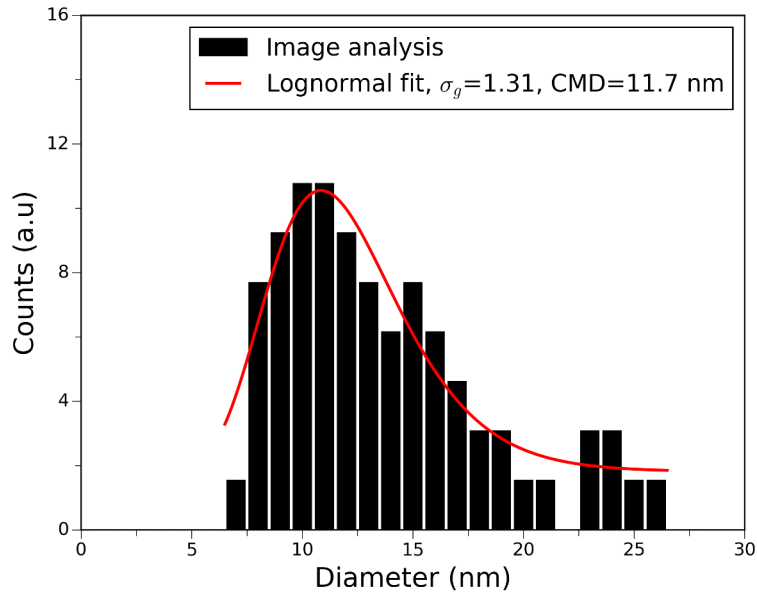


**Figure 3.3.** Nanoparticle size distribution in the gas phase at the center of the heated zone in the CVD reactor P5 at 850 °C.

ratio of the iron core to that of the carbon shell is estimated to be about 1:1.

#### PEAK PARTICLE TEMPERATURE MEASUREMENTS

The heat-up temperature of nanoparticles  $T_p^0$ , which is equal to the nanoparticle temperature at the beginning of the cooling process, were measured by Two-color Pyrometry. The heat-up temperatures in dependence on laser fluence are presented in Fig. 3.4. As can be seen, the particle heat-up temperature increases with the increase of the laser fluence. As mentioned before, Q-Switch Delay was fixed at 350  $\mu\text{s}$ , corresponding to a laser fluence of about 190  $\text{mJ}/\text{cm}^2$  in our experiments. Therefore, the measured particle heat-up temperature is about 2946 K. It is lower than the sublimation temperature of graphite (around 3900 K) and the boiling temperature of bulk iron (around 3100 K) [225]. So the contribution of evaporation is neglected in this model [206, 226, 227]. In

addition, Bougie et al. found little sensitivity of inferred best-fit soot particle diameters when changing the assumed initial soot particle temperature [228]. Therefore, evaluations were done with an initial temperature of 2946 K as a fixed parameter in the model.

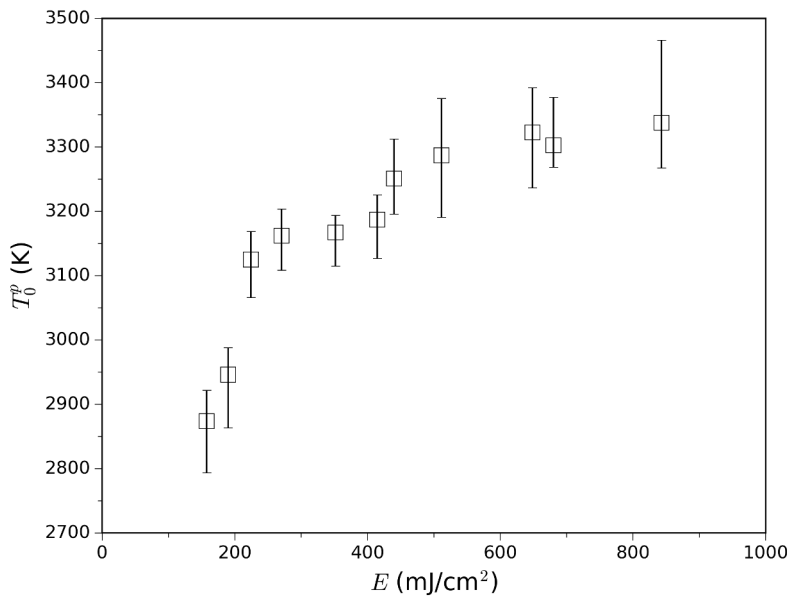


**Figure 3.4.** Particle heat-up temperature  $T_p^0$  of laser heated particles obtained at different laser fluences.

#### THERMAL ACCOMMODATION COEFFICIENT (TAC)

TAC  $\alpha_T$  is the main parameter for an evaluation of the nanoparticle size [229]. A commonly used way to obtain the value of  $\alpha_T$  is comparing the evaluated results with the ones obtained by a reliable sizing technique, such as TEM. Another approach is the variation of  $\alpha_T$  as an additional fit parameter together with  $CMD$  during the fitting process. Fig. 3.5a shows a typical example of the normalised  $\chi^2$  (maximum likelihood estimator) as a function of  $CMD$  and  $\alpha_T$ . As can be seen, a valley of minimum values is reached at the two input pa-

### 3.1. IMPLEMENTATION OF LII

---

rameters. It confirms the uniqueness of the two-parameter data-fit procedure for this case. The best fit in the present case was obtained at  $\alpha_T=0.99$  and  $CMD=12.0$  nm. Fig. 3.5b shows the normalized  $\chi^2$  at different values of  $\alpha_T$  near the minimum values of normalized  $\chi^2$ . The  $CMD$  values associated to  $\alpha_T$  are not presented in the graph. As been observed, The  $\chi^2$  first decreases with  $\alpha_T$  ranging from 0.03 to 0.09, where the minimum  $\chi^2$  are reached. And then the  $\chi^2$  gradually increases with further increase of  $\alpha_T$ . However, it should be note that  $\chi^2$  for  $\alpha_T$  ranging from 0.07 to 0.17 are very close.

To further determine the value of  $\alpha_T$ , TEM was also performed. Fig. 3.6 is plot of the normalized  $\chi^2$  as a function of  $\alpha_T$  with  $CMD$  fixed at 11.7 nm (TEM measurements). As depicted, the minimum  $\chi^2$  value was established at  $\alpha_T=0.09$ . Fig. 3.7 shows a measured cooling curve and three best fits for three different values of  $\alpha_T$  with  $CMD$  fixed at 11.7 nm. It can clearly be seen that the best fit is found for  $\alpha_T=0.09$ . According to above results,  $\alpha_T=0.09$  is applied in the present model.

#### 3.1.2 SENSITIVITY AND UNCERTAINTY ANALYSIS

With the knowledge of  $\alpha_T$  it is possible to evaluate the particle sizes from the measured cooling curves. However, it is important to note that the value of  $\alpha_T$ , the nanoparticles density  $\rho_p$  and the nanoparticle heat capacity  $c_p$  depend on the carbon shell structure, which introduces additional uncertainties. Variations in the assumed properties and also the experimental conditions may cause systematic errors of the evaluated particle sizes. Uncertainty of the nanoparticle density  $\rho_p$  depends on the Fe/C mass ratio in the particles. According to the TEM results, in the case of Fe/C mass ratio at 1:1, the uncertainty of the nanoparticle density is between -38% and 5%. While in the case of Fe/C mass

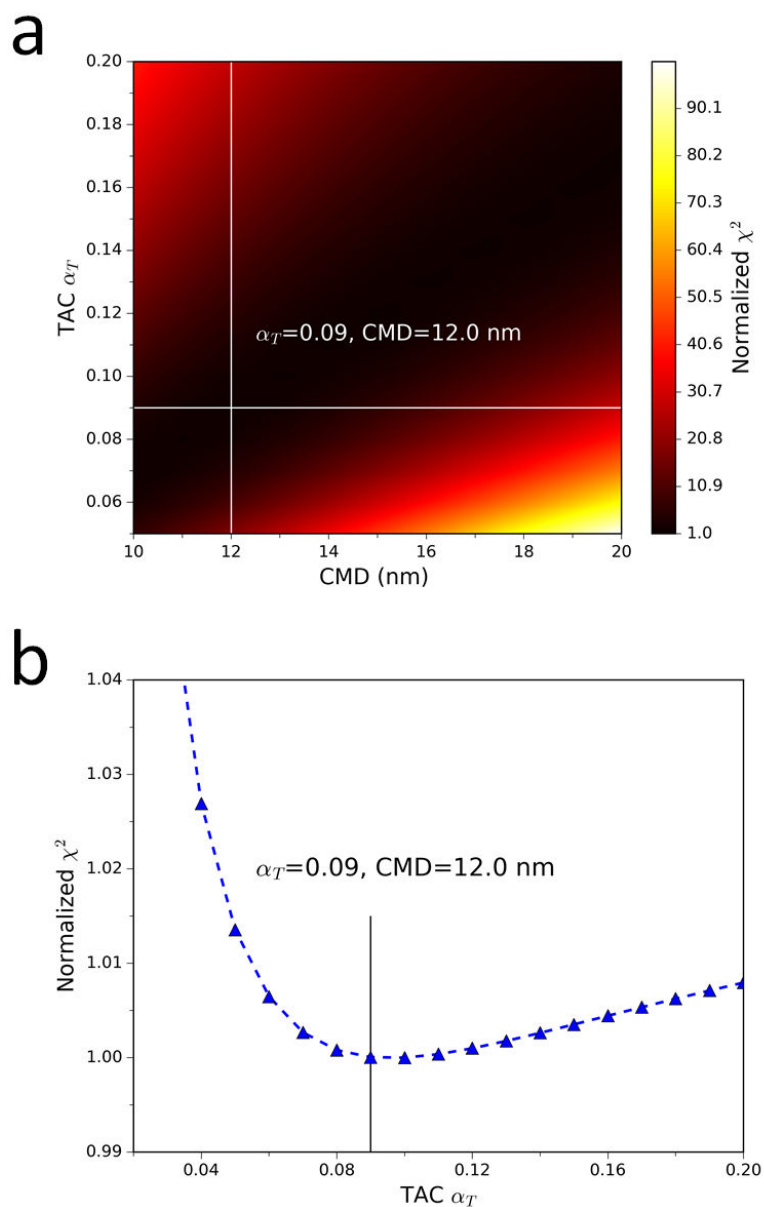


**Figure 3.5.** (a) Least-squares error  $\chi^2$  as a function of thermal accommodation coefficient  $\alpha_T$  and  $CMD$ . (b) Least-squares error  $\chi^2$  as a function of thermal accommodation coefficient  $\alpha_T$  (The  $CMD$  values associated to  $\alpha_T$  are not presented in the graph).

### 3.1. IMPLEMENTATION OF LII

---

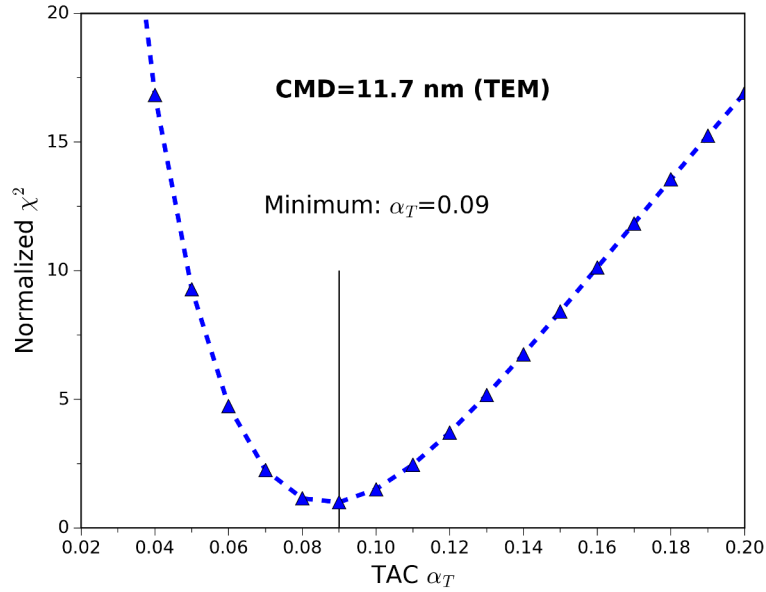


**Figure 3.6.** Least-squares error  $\chi^2$  as a function of thermal accommodation coefficient  $\alpha_T$  with  $CMD$  fixed at 11.7 nm (TEM measurement).

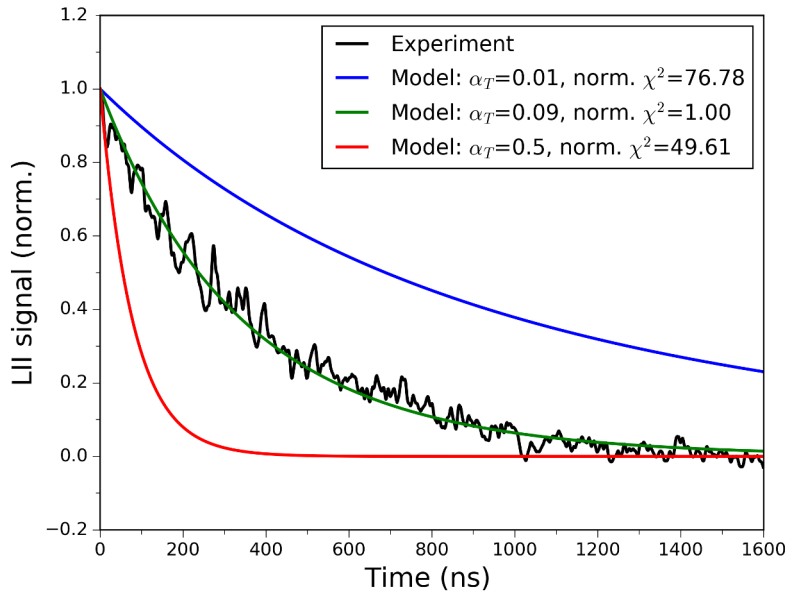


**Figure 3.7.** Measured LII signal of nanoparticles in the gas phase and the best fit curve of calculated LII signals for  $\alpha_T=0.01$ ,  $\alpha_T=0.09$  and  $\alpha_T=0.5$  with  $CMD$  fixed at 11.7 nm (TEM measurement).

ratio 5:1, the uncertainty of nanoparticle density is ranging from -13% to 5%. The carbon shell structure has a more profound influence on the nanoparticle heat capacity. For nanoparticles with a Fe/C mass ratio at 1:1, the maximum possible uncertainty of the nanoparticle heat capacity reaches +119%, which is the difference between the pure iron heat capacity value and the value for nanoparticles with Fe/C mass ratio 1:1. The value of  $\alpha_T$  is determined by comparing the LII measurements with TEM results, which relies on other parameters. Hence the real uncertainty can not be estimated. Since the differences of  $\chi^2$  for  $\alpha_T$  from 0.07 to 0.17 are very small during the two-parameter data-fit procedure (Fig. 3.5b), the possible value of  $\alpha_T$  is from 0.07 to 0.17. The molecular weight of ambient gas  $\mu_g$  and the ratio of the heat capacities of the gas  $\gamma$  are related to the gas composition. The gas composition will change with the CVD conditions.  $\mu_g$  can be in the range of 28.74 (for air) to 39.39 (for argon). While,  $\gamma$  is ranging from 1.39 (for air) to 1.667 (for argon). The deviation of the gas temperature  $T_g$  and the heat-up temperature  $T_0^p$  are set to be  $\pm 5\%$ .

Sensitivity analysis is a widely used method to understand how the solution of a model is dependent on the model parameters [230–232]. In the present study Sobol’s method was used to perform a detailed sensitivity analysis for our LII model by considering each parameter’s contributions (the first-order index  $S_i$ ) and the total contribution (the total-order index  $S_{Ti}$ ) [233]. The greater the sensitivity indices are, the more critical parameters are for the model. An input factor will be considered to be important if it explains more than  $1/k$  ( $k$  is the number of the estimated parameters) of the output variance. For a given factor, a notable difference between  $S_{Ti}$  and  $S_i$  flags an important role of interactions for that factor in the output. A detailed sensitive analysis of these

### 3.1. IMPLEMENTATION OF LII

---

influences  $(\rho_p, c_p, \alpha_T, \gamma, \mu_g, T_g, T_0^p)$  on the evaluated particle size for our model at different Fe/C mass ratios is presented in Fig. 3.8a,b. Results show that the relative sensitive is related to the Fe/C mass ratio in the nanoparticles. In the case of nanoparticles with 1:1 Fe/C mass ratio,  $c_p$  is the most important parameter. It explains 45.3% of the output variance. Followed by  $\alpha_T$  and  $\rho_p$ , the total-order index for  $\alpha_T$  and  $\rho_p$  are 0.338 and 0.182, both larger than 0.143. Thus,  $\alpha_T$  and  $\rho_p$  are also important variables. Furthermore, all the input factors explain 97.8% of the output variance singly. The small difference between the total-order index and the first-order index for each parameter stands for the weak interactions between the parameters, which proves their independence. For nanoparticles with a Fe/C mass ratio at 5:1, the Sobol sensitivity index for  $\rho_p$  and  $c_p$  decrease to 0.04 and 0.173, respectively. Thus  $\rho_p$  and  $c_p$  becomes less important with the increase in the Fe/C mass ratio. More attention should be paid to the parameter  $\alpha_T$  in the experimental application since it become the most important parameter, accounting for 85.6% of the variance of the response variable. The sum of the first-order index reaches 0.93, which means that the variance of the response variable can be well explained by the uncertainty from the individual parameter.

The uncertainty of the key parameters resulted in deviations of particle size extracted in our model at different Fe/C mass ratios are is presented in Fig. 3.9a,b. The results show the uncertainty is strongly depending on the structure of nanoparticles. The possible deviation for nanoparticles with a Fe/C mass ratio at 1:1 caused by the  $\rho_p$  and  $c_p$  are 61.1% and -54.4%. But for nanoparticles with a Fe/C mass ratio at 5:1, the uncertainty resulted from  $\rho_p$  and  $c_p$  decrease to -28.4% and 14.4%. Furthermore, among all the parameters,  $\rho_p, c_p, \alpha_T, \gamma$  exhibit a strong influence on the calculated particle diameter.

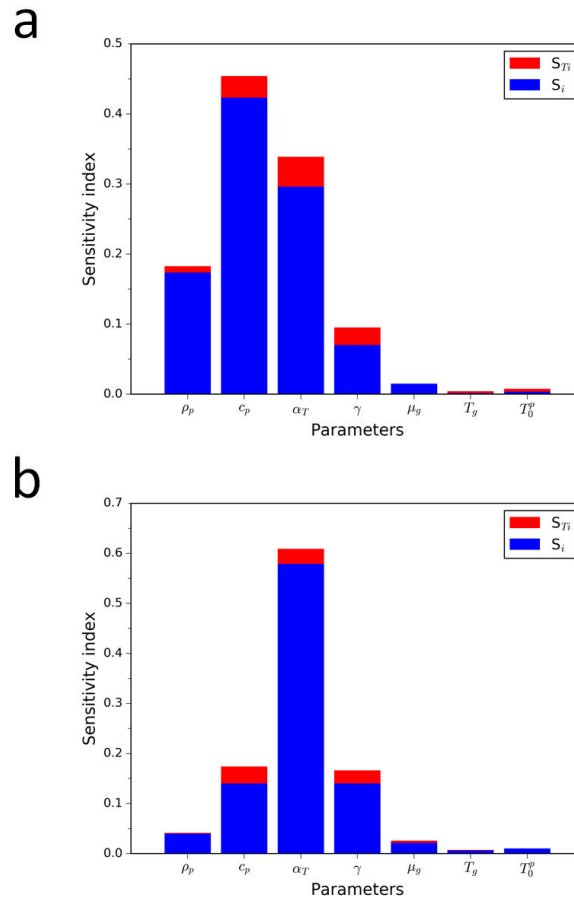


**Figure 3.8.** The first-order  $S_i$  and the total-order  $S_{T_i}$  Sobol sensitivity index of the main parameters in the LII model at the Fe/C mass ratio (a) 1:1 and (b) 5:1.

The maximum deviation reaches 67% when  $\alpha_T = 0.17$  is chosen in the present model. Whereas  $T_0^p$  has a very weak influence on the evaluated particle diameter.  $\pm 5\%$  deviations in  $T_0^p$  only cause 0.39% and -0.14% uncertainty on the resulted particle diameter.

### 3.1.3 COMPARISON OF LII AND TEM PARTICLE-SIZING

LII model was validated by a comparison of the evaluated results with TEM measurements. Two different cases have been conducted: case 1, nanoparticles

### 3.1. IMPLEMENTATION OF LII

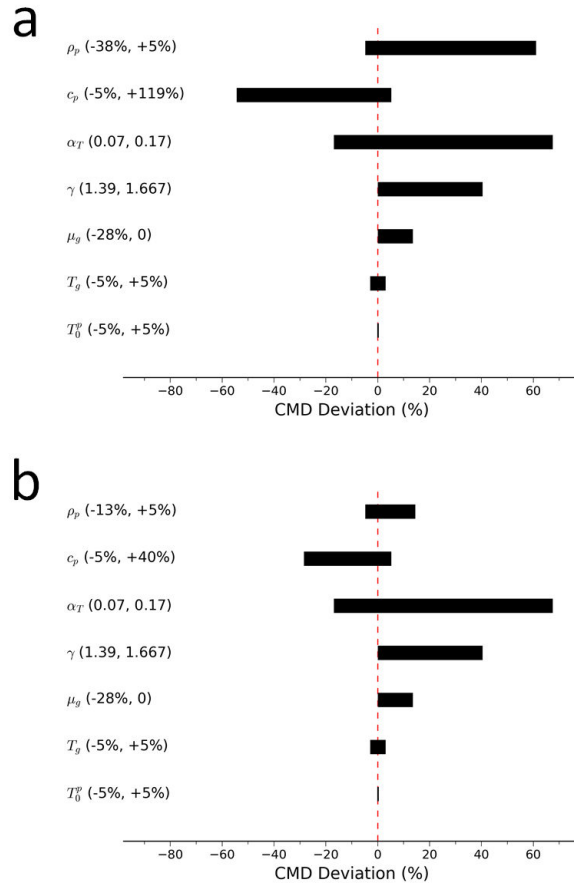


**Figure 3.9.** Uncertainties in particle sizing by LII at the Fe/C mass ratio (a) 1:1 and (b) 5:1.

at the center of the reactor P5 at 750 °C. Case 2, nanoparticles at rear of the reactor P7 at 850 °C. For both cases, nanoparticle size was determined by high resolution TEM and by LII technique separately. In case 1, Fig. 3.10a presents a measured cooling curve and its best fitting curve with  $\sigma_g=1.31$ . It can clearly be seen that the best fit is found at  $CMD=5.9$  nm. And the  $\sigma_g$  and  $CMD$  extracted by approximating the particle size distributions by log-normal function are 1.28 and 5.9 nm (see Fig. 3.10c). It suggests that the evaluated  $CMD$  by LII is in good agreement of TEM measurements. Since  $\sigma_g$  is extracted to be 1.28 by TEM measurements (see Fig. 3.10d),  $CMD$  is

also evaluated by LII model with  $\sigma_g=1.28$ . The resulted value of  $CMD$  is 6.1 nm, which is close to the one with  $\sigma_g = 1.31$ . It indicates that the evaluated  $CMD$  does not strongly rely on the variation of  $\sigma_g$ . In case 2, as can be seen in Fig. 3.10b, the evaluated values of  $CMD$  are 11.1 nm and 11.9 nm with  $\sigma_g=1.31$  and  $\sigma_g=1.26$ , respectively. For both selected  $\sigma_g$ , the predicted  $CMD$  by LII is in good agreement with the TEM analyse, by which the  $CMD$  is measured to be 10.3 nm. It is also found that  $CMD$  by LII only slightly changed by the choice of  $\sigma_g$ . According to these results, it is found that LII can be an useful tool for *in-situ* detection of nanoparticles in the gas phase with an acceptable accuracy.

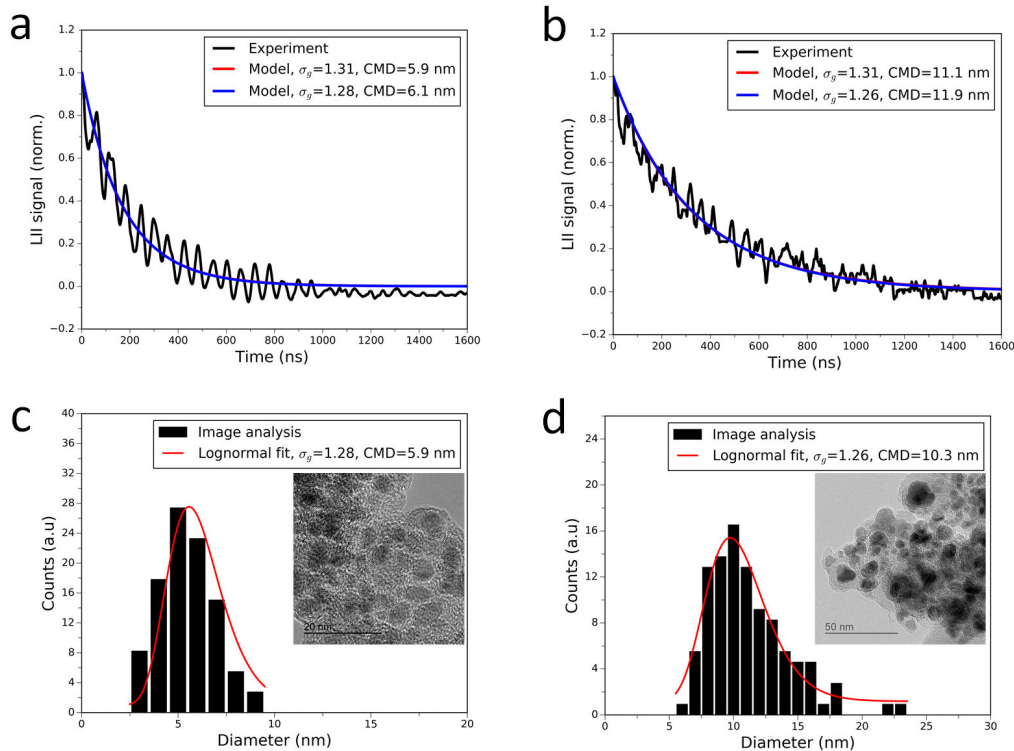


**Figure 3.10.** Measured LII signals of nanoparticles in the gas phase and the best fit curves of calculated LII signal for (a) case 1 (750 °C, P5 ) and (b) case 2 (850 °C, P7 ). The corresponding size distribution of nanoparticles in (c) case 1 and (d) case 2.

## 3.2. NANOPARTICLE EVOLUTION IN THE GAS PHASE

---

### 3.2 NANOPARTICLE EVOLUTION IN THE GAS PHASE

#### 3.2.1 NANOPARTICLES ALONG THE REACTOR

As mentioned in Chapter 1, homogeneous nucleation is proposed as one possible mechanism for iron nanoparticle formation in the gas phase. Based on the homogeneous nucleation hypothesis, CFD simulations predicted that the size of catalytic iron nanoparticles will increase along the reactor axis [172–174]. In order to verify this prediction, the nanoparticle size was examined *in-situ* by LII at different positions along the reactor at 850 °C. The ferrocene/xylene solution with the concentration of 0.05 g/mL was fed at 0.2 mL/min. And a mixture of 0.78 L/min argon, 0.2 L/min H<sub>2</sub>, 0.02 L/min C<sub>2</sub>H<sub>2</sub> were also provided as the carried gas. We did not detect any LII signals at P1. And at P2 the LII signals were too weak to be analyzed for particle sizing. It indicates that few nucleation of nanoparticles take place in the gas phase. From P3 to P7 we can obtain strong LII signals. Fig. 3.11 shows the evaluated nanoparticle size at locations from P3 to P7. The nanoparticle size at position P3, P4, P5, P6 and P7 are 10.7, 10.3, 12.5, 12.2 and 11.0 nm, respectively. It is found that the nanoparticle size does not show obvious difference along the reactor.

The evolution of nanoparticles along the reactor axis was also investigated by TEM at the same CVD conditions. At P1 we did not observe any NPs at all, which is in accordance with the LII results. It indicates that nanoparticles do not nucleate at P1 in the gas phase. Whereas we successfully detected nanoparticles in the gas phase from P2 to P7. The typical TEM images of nanoparticles obtained in the gas phase at different positions (from P2 to P7) are shown in Fig. 3.12. In the TEM images, the spherical particles of 5-30 nm in size are found. In addition, particle agglomerates are observed. As

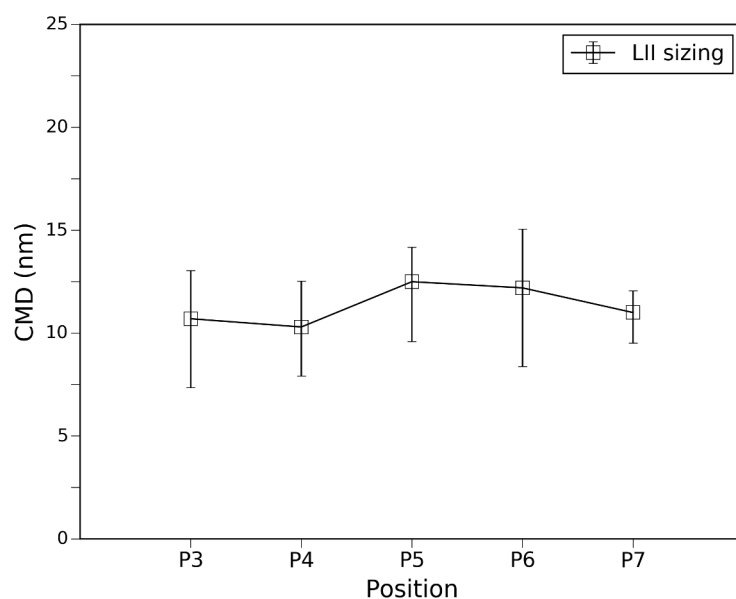


**Figure 3.11.** Nanoparticle size evolution in the gas phase at different positions in the CVD reactor at 850 °C.

aforementioned, nanoparticles at the center of the heated zone P5 are identified to be carbon-encapsulated iron nanoparticles with the size of about 5-30 nm (see Fig. 3.1 and Fig. 3.2).

Noteworthy, at the front of the reactor (P3), a large number of nanoparticles exhibit another kind of structure, as depicted in Fig. 3.13. No obvious graphite shell or very thin layer of carbon around iron core is found in these particles. In addition, the samples of nanoparticles at the front of the heated zone P3 were also analyzed by EDS. The typical spectrum of NPs is presented in Fig. 3.14a, Similar to the results for nanoparticles at P5, copper, silicon, iron and carbon elements were detected. While it is interesting to note that oxygen element was found in nanoparticles at P3. The HAADF STEM was also performed. The STEM image is shown in Fig. 3.14b, and the map of spatial distribution of iron and carbon elements in the sample are presented in Fig. 3.14c-e. It can be observed that oxygen elements are distributed on the

### 3.2. NANOPARTICLE EVOLUTION IN THE GAS PHASE

---

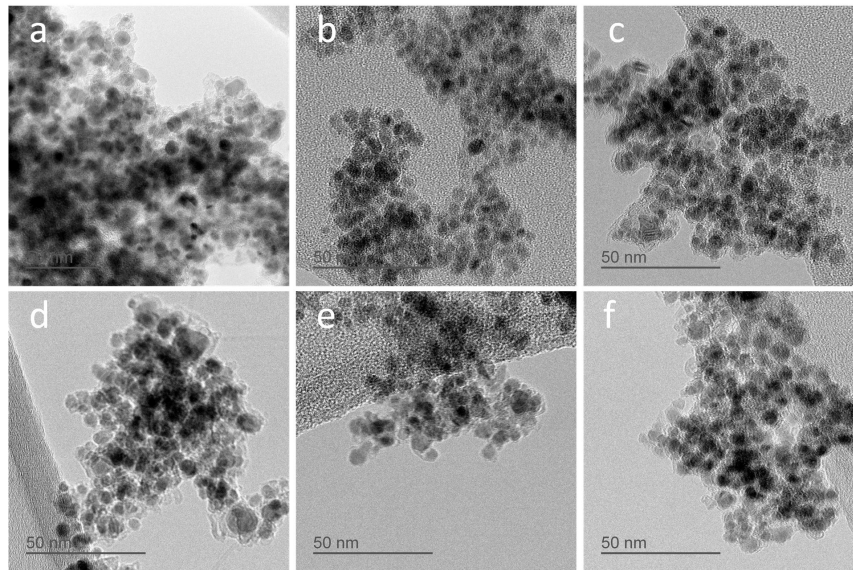


**Figure 3.12.** Typical TEM images of nanoparticles with low resolution obtained in the gas phase at the different positions (a) P2, (b) P3, (c) P4, (d) P5 (e) P6 and (f) P7.

edge of nanoparticles, indicating that nanoparticle surface is oxidized. In our CVD conditions, iron nanoparticles are protected from being oxidized in argon in the reactor. Therefore, oxidation must take place at the outlet of small tubes along the reactor. However, oxygen element is not found in nanoparticles at P5. These results indicate that iron nanoparticles have been encapsulated by the graphite layer inside the reactor at P5. The graphite layer can effectively prevent nanoparticles from being oxidized. Hence no oxygen element is found in nanoparticles at P5. While, the surface of some nanoparticles at P3 is not completely covered by carbon atoms, there are still some active iron atoms on the surfaces of nanoparticles. They will be oxidized in the oxygen environment. Therefore, we find the presence of oxygen in nanoparticles at P3. These observations indicate that some nanoparticles display the structure change from iron nanoparticles to carbon-encapsulated iron ones in the reactor.

The size evolution of nanoparticles along the reactor axis was also inves-

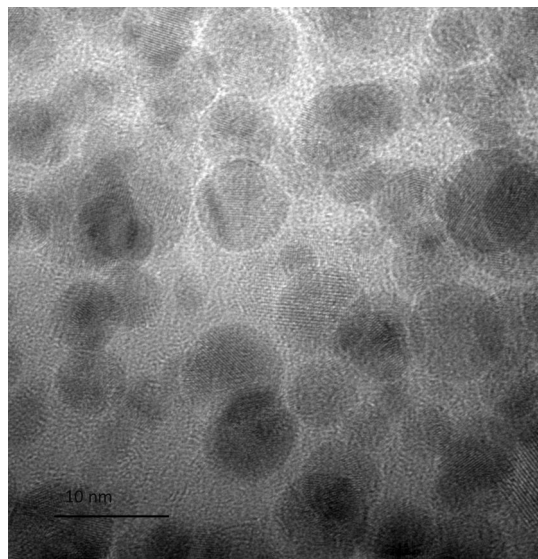


**Figure 3.13.** High resolution TEM image of nanoparticles at the front of the heated zone P3.

tigated by TEM. Since both iron nanoparticles and carbon-encapsulated iron nanoparticles are observed in the TEM images and iron nanoparticles are commonly considered to be catalytic active for hydrocarbon decomposition, only the size distribution of the iron core was taken into account. The size distribution of the iron core in the reactor is presented by the histogram in Fig. 3.15. The *CMD* of nanoparticles is obtained by fitting size distribution by a log-normal function. The *CMD* of the iron nanoparticles at position P2, P3, P4, P5, P6 and P7 are 4.2, 5.6, 6.2, 7.1, 8.2 and 7.6 nm, respectively. In the front of the reactor, the mean diameter of nanoparticles is found to increase from 4.2 nm at P3 to 7.1 nm at P5 along the reactor. The bigger nanoparticles are found closer to the center of the furnace. However, nanoparticle size distribution does not show obvious difference from P5 to P7.

The formation process and the growth rate of nanoparticles from thermal decomposition of ferrocene were predicted by CFD simulations in previous works [172–174]. In these models, the nanoparticle growth process in an argon at-

### 3.2. NANOPARTICLE EVOLUTION IN THE GAS PHASE

---

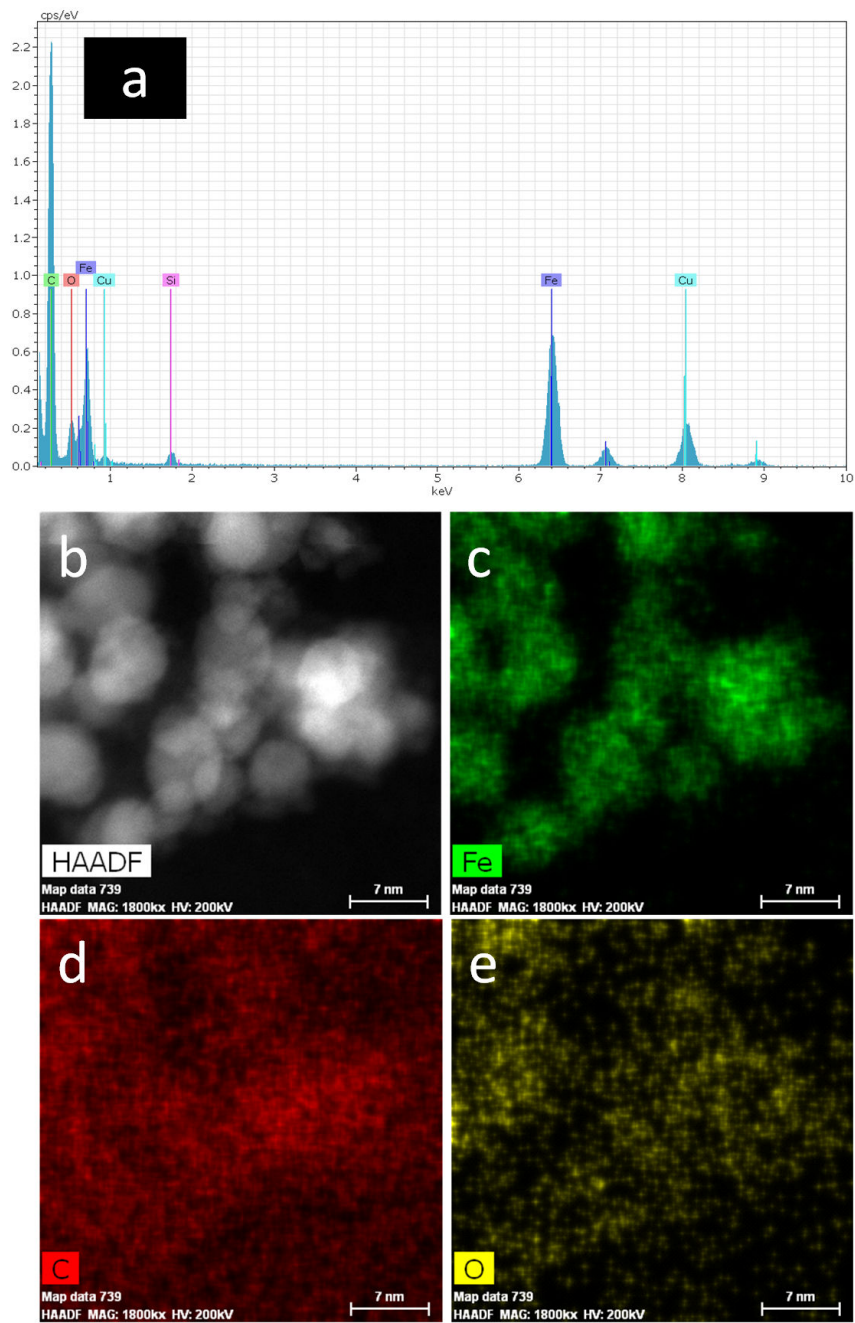


**Figure 3.14.** (a) Spectrum, (b) STEM image and (c-e) map distribution of chemical elements in the sample of nanoparticles obtained at the front of the heated zone P3.

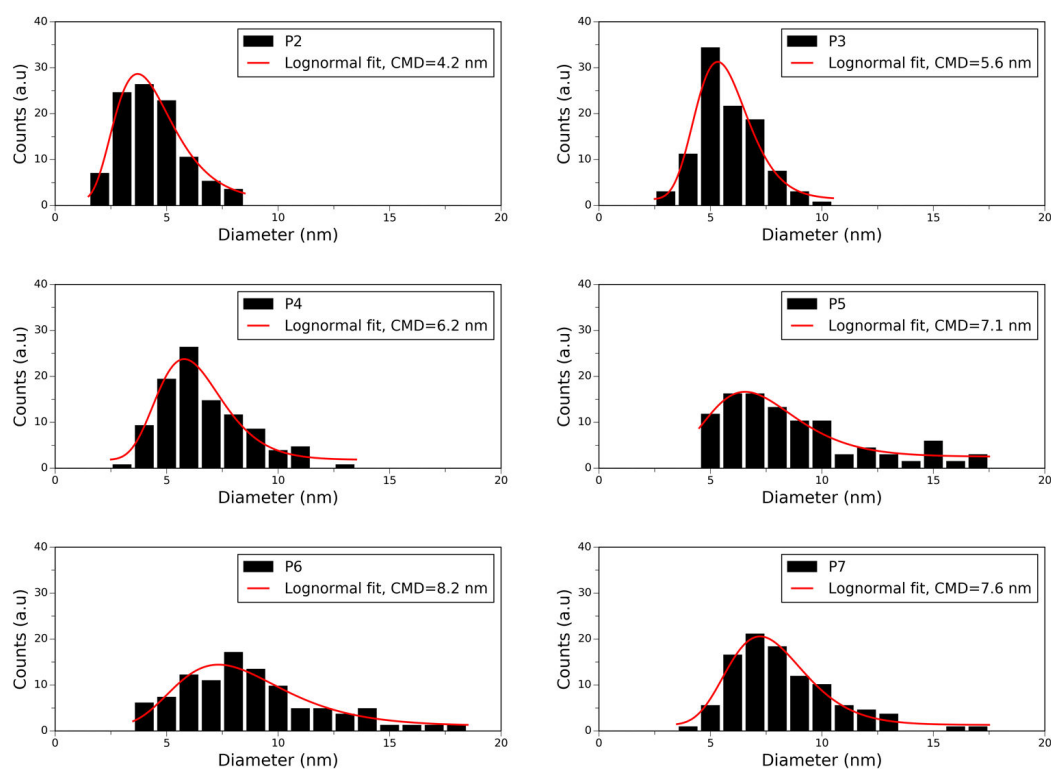


**Figure 3.15.** Nanoparticle size evolution in the gas phase at different positions in the CVD reactor at 850 °C.

mosphere was described by the homogeneous nucleation theory. Nanoparticles formed by homogeneous nucleation and then grew up by coalescence. CFD simulations predicted that the nanoparticle size increased along the reactor. As can be seen in Fig. 3.16 [172], at 1000 K the formation of particles with diameters about 7-8 nm only needs several seconds. It indicates that the nanoparticle nucleation and growth happen very quickly. Based on this prediction, we can make an rough estimation in our experiment conditions. In our experiment the gas flow rate is fixed at 1.0 L/min and the diameter of the reactor 45 mm, thus the speed of the gas in the reactor will be about 0.01 m/s. We simply assume that nanoparticles suspended in the gas phase has the same speed as the gas flow. And the temperature in our experiment is 1123 K, higher than

### 3.2. NANOPARTICLE EVOLUTION IN THE GAS PHASE

---

1000 K. Hence formation of a 7-8 nm nanoprticle will occur within 7-8 s. A 7-8 nm nanoparticle can only travel less than 7-8 cm along the reactor. It also means that iron nanoparticles can only survive within less than 7-8 s inside the reactor.

As observed in Fig. 3.15, the nanoparticle size increase from P1 to P5 in the front of the reactor, which is in good agreement with the prediction. However, nanoparticle size distribution does not show obvious difference form P5 to P7. This phenomenon contradicts the CFD prediction. It is worth emphasizing that nanoparticles are assumed to be pure iron nanoparticles and the effect of carbon element on the iron nanoparticles growth are not take into account in the CFD models. While in our experiments nanoparticles are not pure iron nanoparticles but carbon-encapsulated iron ones. The iron core is always covered by the carbon layer, as shown in Fig. 3.1a. Furthermore, according to the EDS, oxygen element is not found in the nanoparticles at P5, indicating that iron nanoparticles have been encapsulated by the graphite layer inside the reactor at the center of the heated zone P5. The graphite layer can effectively prevent nanoparticles from being oxidized. Whereas we can find the presence of oxygen in these nanoparticles at P3, implying that the surface of the nanoparticles are oxidized. According to the above discussions, we attribute the termination of the nanoparticle growth to the carbon encapsulation under the studied conditions. Iron atoms generate from thermal decomposition of ferrocene. Once the iron partial pressure is higher than its saturated vapor pressure, iron nanoparticles will form by homogenous nucleation. Since direct bond cleavage pyrolysis of hydrocarbon only happen at temperature much higher than 850 °C [34], it can be concluded that the carbon atoms mainly come from catalytic decomposition of hydrocarbon on iron NP surface. They dissolve into iron nanoparticles

during the growth process, finally precipitate from the iron nanoparticle surface. During the growth process, nanoparticles are pure iron nanoparticles or the carbon/iron mixture. Once nanoparticles are encapsulated by amount of carbon atoms, the growth will stop. Because the temperature at front of the reactor is lower than that in the center of the heated zone, the nanoparticles been found in the center of the heated zone are larger than those at the front of the furnace.

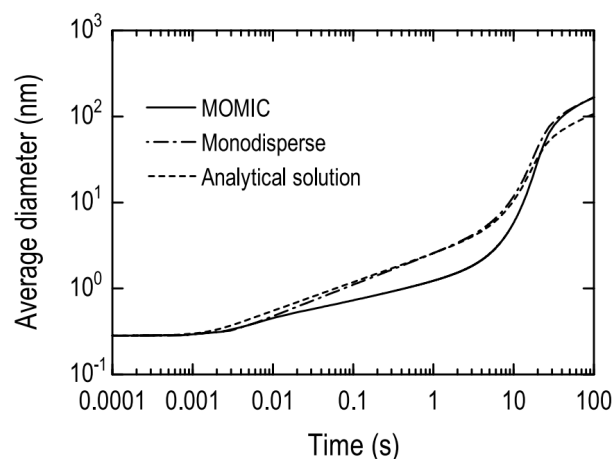


**Figure 3.16.** Comparison between MOMIC simulation and analytical solutions. The reaction temperature is 1000 K and the initial ferrocene concentration is 280 ppm [172].

### 3.2.2 NANOPARTICLES AT DIFFERENT CVD CONDITIONS

It is well known that the length of CNTs is strongly related to the CVD duration. A good understanding of the nanoparticle evolution with CVD duration is of paramount importance to elucidate the roles of nanoparticles in the gas phase during CNT growth. For this purpose, the mean size evolution of nanoparticles in the gas phase as a function of CVD duration was investigated by LII measurement at 650, 750 and 850 °C. CVD procedures were preformed

### 3.2. NANOPARTICLE EVOLUTION IN THE GAS PHASE

---

at 850 °C. 0.05 g/mL ferrocene/xylene solution was injected at the rate of 0.2 mL/min. 0.78 L/min argon, 0.2 L/min H<sub>2</sub>, 0.02 L/min C<sub>2</sub>H<sub>2</sub> were fed as the carrier gas. It is found that the temperature exhibits a pronounced effect on nanoparticle formation in gas phase. No LII signals were detected at 650 °C at all positions along the reactor. Whereas LII signals were detected successfully at 750 and 850 °C. Fig. 3.17 shows the mean size evolution of nanoparticles in the gas phase at the center of the reactor as a function of CVD duration. The *CMD* of nanoparticles are almost constant in all 60 min at both 750 and 850 °C. It means that the system reaches an equilibrium state during the FC-CVD process with the continuous injection of ferrocene and carbon sources. Furthermore, the evaluated *CMD* of nanoparticles in the gas phase by LII at 750 and 850 °C are about 5.1 nm and 12.5 nm in all the time, respectively. It indicates that the *CMD* of nanoparticle greatly increases with the temperature increasing from 750 to 850 °C. At high temperature, fast decomposition of ferrocene will result in a higher iron vapor pressure. It can promote the nucleation and coalescence of nanoparticles in the gas phase, finally leading to larger nanoparticles. It also can be seen that the evaluated *CMD* by LII is in good agreement with the one by TEM measurements.

As mentioned before, during the whole nanoparticle growth process free carbon atoms or clusters generate by catalytic decomposition of hydrocarbon on the iron nanoparticles surface, dissolve into nanoparticles and finally precipitate from the surface of nanoparticles. Once iron nanoparticles are encapsulated by the carbon layer, they stop growing up. So the final size of iron-based nanoparticles will depend on the competition between the rate of iron nanoparticle growth and carbon encapsulation. In order to investigate the effect of CVD conditions on the nanoparticle size, the size distribution of the iron core was

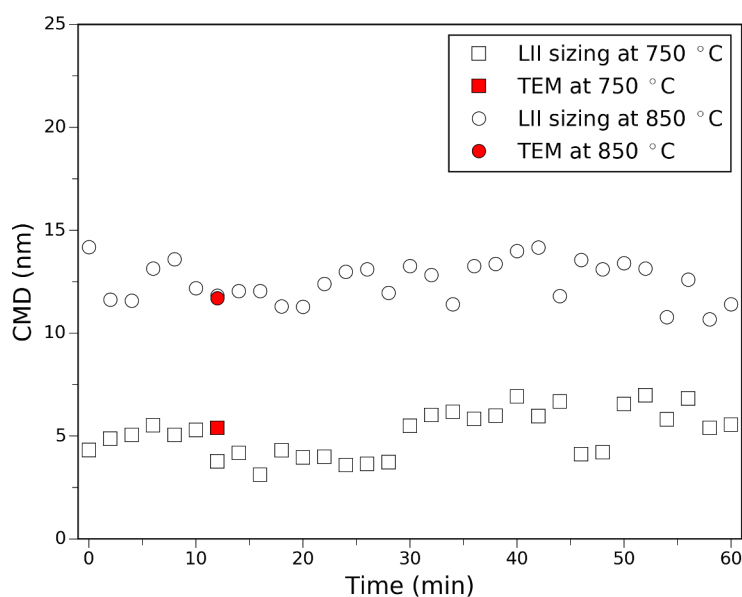


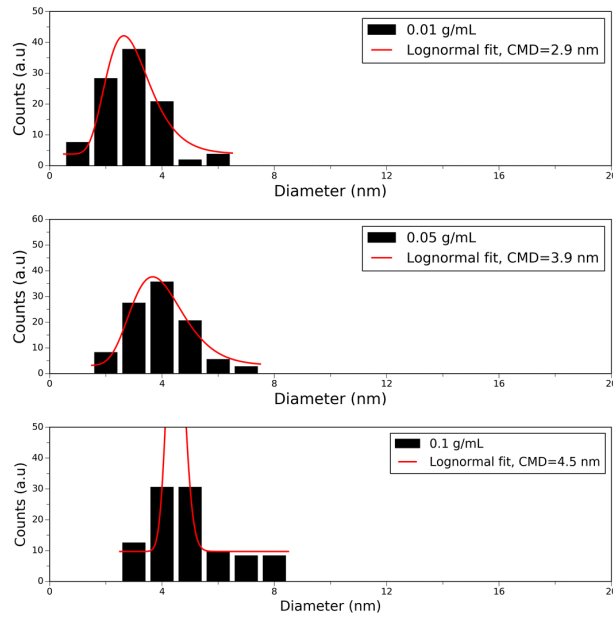
**Figure 3.17.** Nanoparticle size evolution in the gas phase at the center of the reactor as a function of CVD duration.

examined at different experiment conditions, such as ferrocene concentration,  $H_2$  flow rate and  $C_2H_2$  flow rate. Since nanoparticles at the center of the heated zone P5 are encapsulated by the carbon layer, in the following CVD runs, the nanoparticles at P5 were collected by TEM. For ferrocene concentration ranging from 0.01 to 0.05, 0.1 g/L at 750 °C, the mean nanoparticle diameters are 2.9, 3.9 and 4.5 nm, as depicted in Fig. 3.18. The mean diameter of nanoparticles increases with the ferrocene concentration. The increase of nanoparticle size can be attributed to the enhanced nucleation due to the higher iron concentration in the gas phase. High ferrocene concentration will result in a higher iron vapor pressure. It can promote the nucleation and coalescence of nanoparticles in the gas phase.

The nanoparticle size distributions at different  $H_2$  flow rates are demonstrated in Fig. 3.19. As can be seen, the mean nanoparticle diameters are 5.2, 3.9 and 4.9 nm with a  $H_2$  flow rate of 0 L/min, 0.2 L/min and 0.4 L/min,

### 3.2. NANOPARTICLE EVOLUTION IN THE GAS PHASE

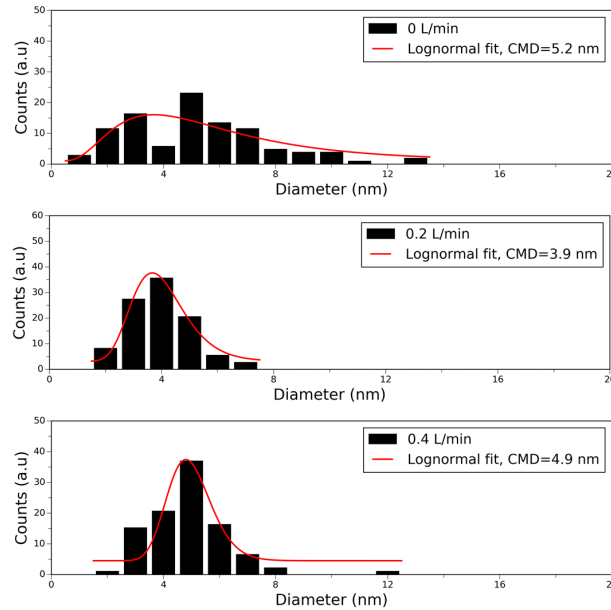
---



**Figure 3.18.** Nanoparticle size distribution at different ferrocene concentrations.

respectively. The mean nanoparticle diameter first increase with higher  $H_2$  up to 0.2 L/min and also the size distribution is noticeably narrowed. When the  $H_2$  flow rate increases further to 0.4 L/min, the mean nanoparticle diameter increases to 4.9 nm. It seems that  $H_2$  serves a dual role during the nanoparticle growth process in the gas phase. Therefore, the effect of  $H_2$  on nanoparticle growth can be both facilitating and inhibiting depending on the amount of  $H_2$  in the CVD conditions. It can be interpreted by the homogeneous nucleation hypothesis. At relatively low  $H_2$  flow rate (0.2 L/min), the replacement of 20 % Ar (molar mass: 40 g/mol) by a lighter gas  $H_2$  (molar mass: 2 g/mol) will change the nucleation rate though its influence on the collisions during the nanoparticle growth process in the gas phase. Since the energy exchange per collision is too small for too small molar masses [234–236]. 0.2 L/min  $H_2$  addition will increase the nucleation rate, finally results in the reduction of the size of nanoparticles. At higher flow rate (0.4 L/min), the etching effect of  $H_2$

becomes dominate.  $H_2$  can react with carbon and reduces the carbon deposition rate on the surface of iron nanoparticles [237]. Thus, the nanoparticle size increases with the increase of the  $H_2$  gas flow rate form 0.2 L/min to 0.4 L/min.



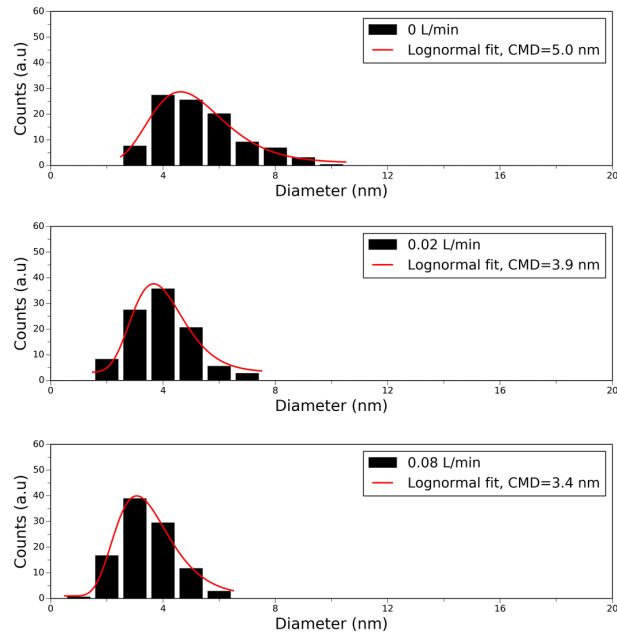
**Figure 3.19.** Nanoparticle size distribution at different  $H_2$  flow rates.

Fig. 3.20 shows the nanoparticle size distributions at the  $C_2H_2$  flow rate ranging from 0 L/min to 0.08 L/min. As can be observed, the *CMD* of nanoparticles is 5.0 nm when no  $C_2H_2$  is injected. The *CMD* diminish to 3.9 nm when 0.02 L/min  $C_2H_2$  is provided. Further increase in the  $C_2H_2$  flow rate will make the *CMD* decreases to 3.4 nm at a  $C_2H_2$  flow rate of 0.08 L/min. It suggests that carbon supply rate is enhanced at a higher  $C_2H_2$  flow rate. More carbon atoms will accumulate on the catalyst surface, iron-based nanoparticles will more easily be encapsulated before they grow up to larger ones.

Among all the CVD parameters, the temperature exhibits the strongest influence on the nucleation process. It is in accordance with CFD simulations that both nucleation and collision become important, while the surface growth

### 3.3. CONCLUSION

---



**Figure 3.20.** Nanoparticle size distribution at different  $C_2H_2$  flow rates.

is less important in our temperature range.

### 3.3 CONCLUSION

To sum up, an *in-situ* diagnostic technique LII was applied for nanoparticle sizing during the FCCVD process. High resolution TEM shows that nanoparticles in the gas phase exhibit a core-shell structure with an iron core and a carbon shell. Therefore, the theoretical LII signal was simulated by taking into account the carbon-encapsulated iron NP density, heat capacity and size distribution etc. A detailed sensitivity and uncertainty of the key parameters on the evaluated particle size for this model was also estimated. Using the developed approach, the evolution of nanoparticles in the gas phase was investigated. It was found that the mean nanoparticle size increase quickly at the front of the reactor while does not change during the downstream region in the reactor. In

addition, the CVD conditions, such as temperature, ferrocene concentration, gas flow rate, also exhibit a great influence on the mean nanoparticle size.

# 4

## CNTs on the substrate

In this Chapter, CNTs were synthesized on the substrate under different CVD conditions. The as-grown CNTs were characterized by SEM, Raman, TGA and high resolution TEM. By correlating the information on the axial nanoparticle evolution and the morphology of CNTs synthesized on the substrate along the reactor axis, the roles of nanoparticles in the gas phase during FCCVD synthesis of CNTs were also discussed.

### 4.1 CNT EVOLUTION ON THE SUBSTRATE

As discussed in Chapter 3, the mean nanoparticle size increase quickly at the front of the reactor while does not change during the downstream region in the reactor at 850 °C. To provide insight on the roles of nanoparticles in the gas phase during the CNT growth, CNTs were also synthesized on the substrate at the same CVD condition. CVD were performed at 850 °C with 0.2 mL/min of ferrocene dissolved into xylene at 0.05 g/mL under 0.78 L/min Ar,

0.2 L/min  $H_2$ , 0.02 L/min  $C_2H_2$  atmosphere. It was found that CNTs grew only in the front of the reactor (from P1 to P4) on the quartz plate; no CNTs were observed from P5 to P7. Fig. 4.1a-d display the typical morphology of CNTs synthesized on the quartz plate in the reactor at different axial locations (from P1 to P4) at 850 °C. As observed, the start of the CNT growth on the quartz plate occurs at the location P1 along the reactor. However, the as-synthesized CNTs exhibit a poor degree of alignment, short lengths (6  $\mu\text{m}$ ) and low density (Fig. 4.1a). From P2 to P4, the high dense well-aligned CNTs synthesized on the quartz plate (Fig. 4.1b-d). The obvious length change can be observed along the reactor. The length of CNTs at P2 increases to 24  $\mu\text{m}$ , then reaches its maximum 42  $\mu\text{m}$  at P3. When it is closer to the center of the reactor, the length of CNTs becomes shorter (33  $\mu\text{m}$ ) at P4. However, from the center of the reactor (P5) to the rear (P7), no CNTs were observed on the quartz plate.

Raman profiles of CNTs at different axial locations are presented in Fig. 4.1a. All specimens display two first-order peaks near 1330 and 1590  $\text{cm}^{-1}$ , assigned to the D-bands and G-bands, respectively. The G-band is the characteristic peak for the stretching vibration of carbon  $sp^2$  bonds in a hexagonal lattice, and the D-band corresponds to the disordered  $sp^2$  phase plus possible contributions of the scattering of  $sp^3$ -bonded carbon [219]. The intensity ratio of the G-band to the D-band ( $I_G/I_D$ ) is commonly invoked as a benchmark of the CNT crystallinity. Fig. 4.2b is a plot of the  $I_G/I_D$  ratio of CNTs at different locations. The  $I_G/I_D$  ratio first increases from 0.73 at P1, passing 0.87 at P2, to 1.05 at P3, where high dense well-aligned CNTs with long length are observed. Finally, The  $I_G/I_D$  ratio decreases again to 0.99 at P4. Comparing Fig. 4.2b with Fig. 4.1a-d, it can be found that the  $I_G/I_D$  ratio and the length of CNTs display the similar tendency. These results indicate that longer CNTs tend to

#### 4.1. CNT EVOLUTION ON THE SUBSTRATE

---

present higher crystalline quality, which is consistent with other studies [238].

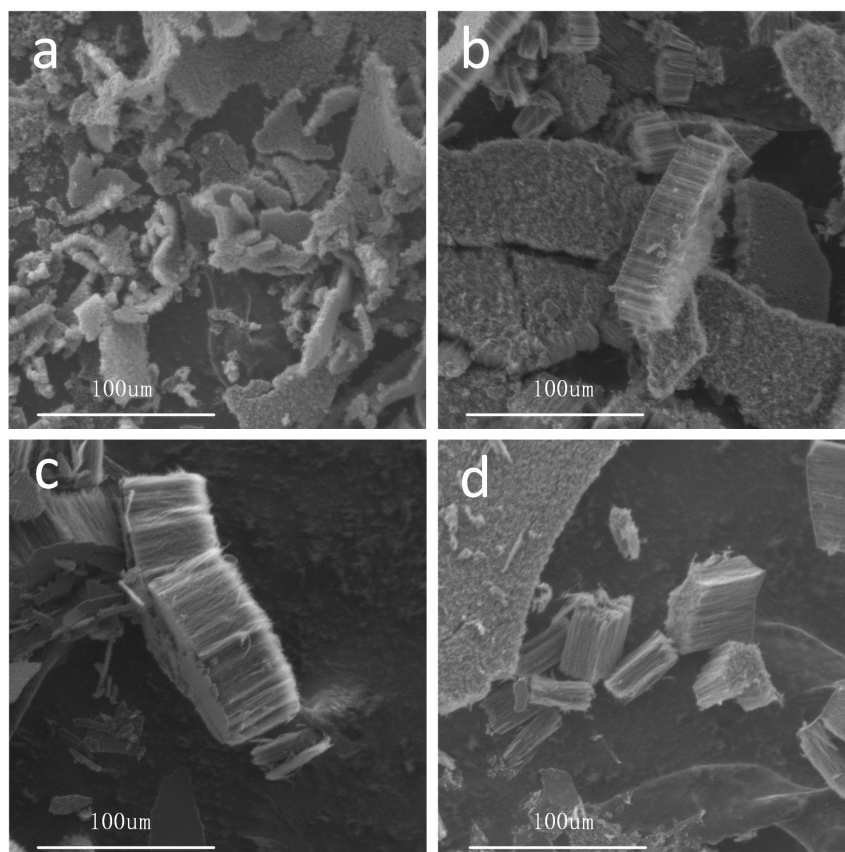


**Figure 4.1.** SEM images of CNTs grown on quartz plate in the reactor at different axial locations (a) P1, (b) P2, (c) P3 and (d) P4.

It should be noted that no nanoparticles were detected at P1 in the gas phase, as described previously. But CNTs were synthesized successfully at the same location on the substrate. It means that homogeneous nucleation is not the prerequisite for CNT growth on the substrate. In addition, the TEM image of CNTs on the quartz plate at the front of the heated zone (P3) is presented in Fig. 4.3. The typical structure of CNTs can be identified. The diameter of CNTs is about 20-40 nm. The interesting observation is the presence of nanoparticles decorated on the CNT wall. They are in size of about 4-15 nm, the sizes of which are similar to the nanoparticles in the gas phase. It

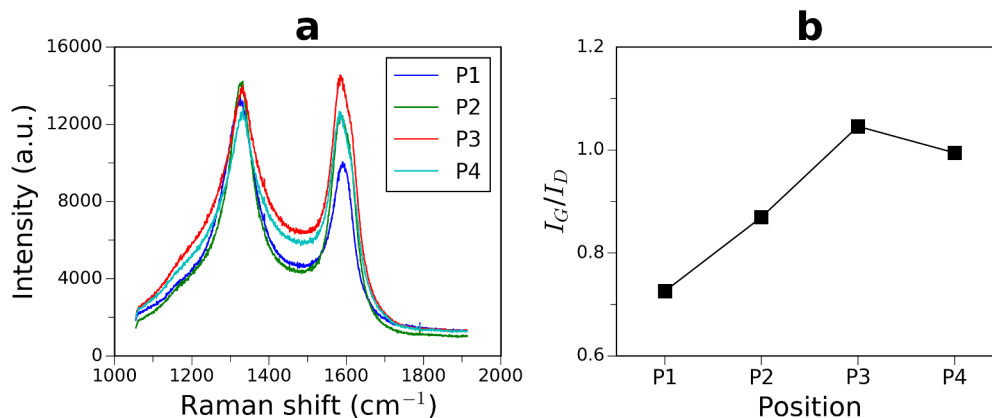


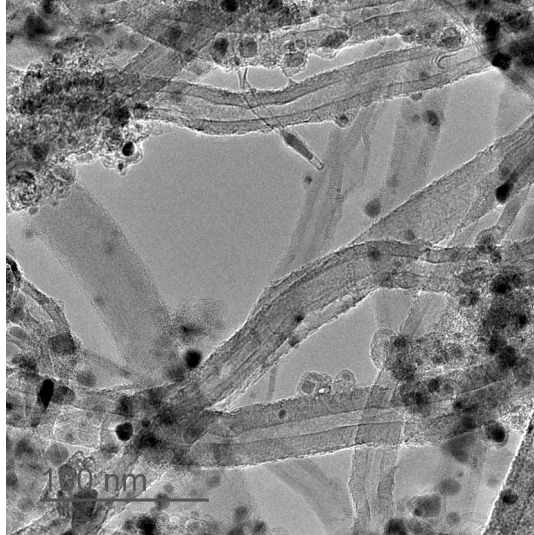
**Figure 4.2.** (a) Raman spectra and (b) the corresponding intensity ratio between D band and G band ( $I_G/I_D$ ) of CNTs grown on quartz plate in the reactor at different axial locations (from P1 to P4).

is reasonable to assumed that these nanoparticles nucleate in the gas phase. They attach to the CNTs synthesized on the substrate by the gas flow. It is also significant that the nanoparticle size detected in the gas phase is far from that measured on the substrate, revealing that nanoparticles in the gas phase do not directly attach to the substrate for CNT growth. It can be verified by the observation that the size of nanoparticles in the gas phase increases quickly along the reactor axis from P2 to P5 and keeps constant from P5 to P7, while nanoparticle evolution on the substrate does not exhibit the similar trend. If nanoparticles in the gas phase can further participate of CNT growth on the substrate, they must coalesce on the substrate. However, as depicted previously, iron nanoparticles are encapsulated by the graphite layers. Due to the graphite layer, carbon-encapsulated iron nanoparticles are very stable, they can not coalesce on the substrate to form large nanoparticles for CNT growth on the substrate. According to these discussions, it can be deduced that nanoparticles in the gas phase can not directly attach to the substrate for CNT growth or aggregate on the substrate to larger catalytic nanoparticles for

#### 4.1. CNT EVOLUTION ON THE SUBSTRATE

---

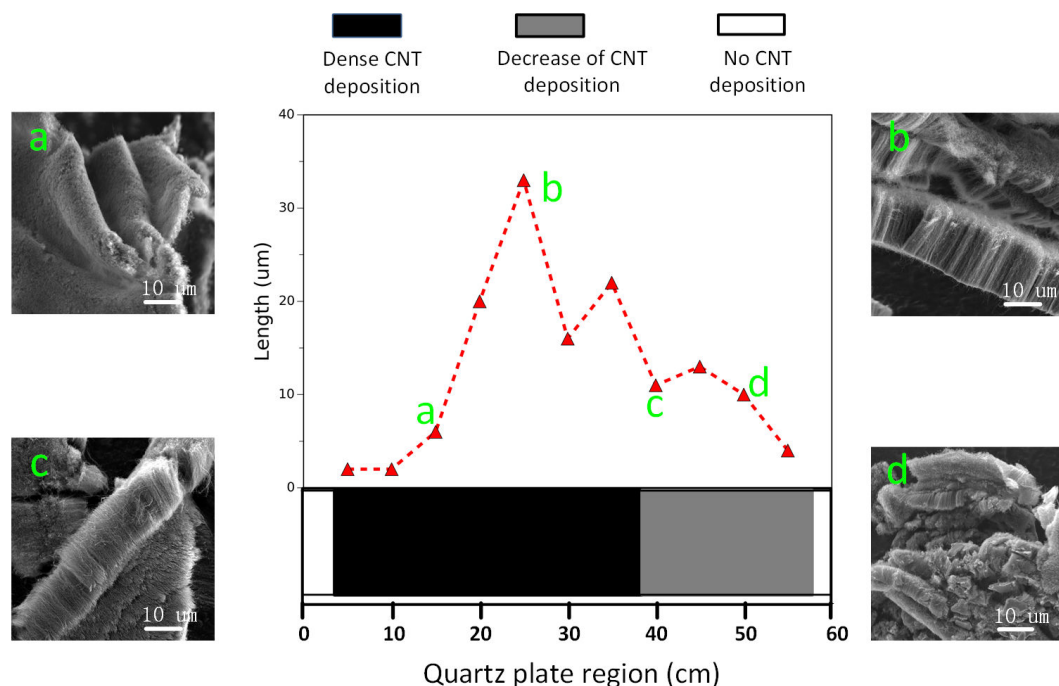
CNT growth once they are encapsulated by the graphite layer.



**Figure 4.3.** TEM image of CNTs grown on quartz plate at the front of the reactor (P3).

In addition, CNT evolution along the reactor on the quartz plate was also investigated at 650 °C. It is found that CNTs were observed in the all region of the heated zone except for the first 5 cm. Fig. 4.4 shows the distribution of CNTs obtained on the quartz plate. As indicated, the obvious change in the CNT density and length can be observed along the reactor. In the front of the reactor (10-15 cm) the very short CNTs with a poor degree of alignment are observed. The length of CNTs is less than 10  $\mu\text{m}$ . Toward to the center of the reactor, the CNTs become longer. From 20-35 cm, the high dense well-aligned CNTs with the length about 20-30  $\mu\text{m}$  are found on the quartz plate. From 35-60 cm, CNTs gradually become shorter and the CNT density also decreases.

As demonstrated in Chapter 2, when the furnace is set to 650 °C, the isothermal area ( $\pm 10$  °C) is found from 20 to 40 cm. CNTs in the isothermal area were also analyzed by Raman spectroscopy. The Raman spectra and the corresponding intensity ratio between D band and G band ( $I_G/I_D$ ) are presented in



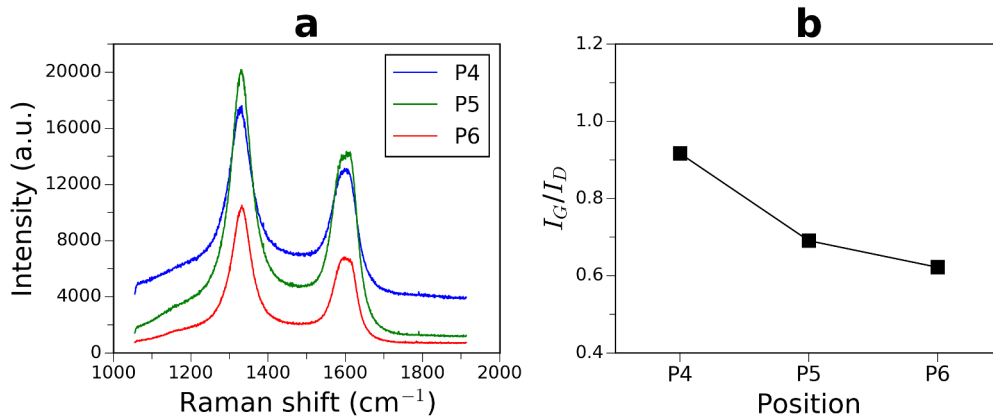
**Figure 4.4.** Schematic of CNT deposition on quartz plate at 650 °C. The typical SEM images of CNTs grown at (a) 5-20 cm, (b) 20-35 cm, (c) 35-45 cm and (d) 45-60 cm. Note: P1 is put at the position of 0 cm, P5 is at 30 cm.

Fig. 4.5. The disorder induced D-band and the graphite like G-band is clearly visible at near 1330 and 1590  $\text{cm}^{-1}$  in all three cases. As seen in Fig. 4.5b, from P4 to P6,  $I_G/I_D$  continuously decreases from 0.92 at P4, passing 0.69 at P5, to 0.62 at P6. It indicates that the crystalline quality of CNTs become worse along the reactor in the isothermal area. Furthermore, the typical TEM images and the diameter distribution of CNTs obtained in the isothermal area on the quartz plate are shown in Fig. 4.6 and Fig. 4.7. The typical structure of CNTs can be found in TEM images. The mean diameter of CNTs at P4, P5 and P6 are 13.7, 13.0 and 13.3 nm, respectively, which shows that the mean diameter of CNTs in the isothermal area are almost the same. It has been recognized that the diameter of CNTs is directly proportional to the size of catalytic particles [18, 19]. Hence the mean diameter of catalytic nanoparticles

#### 4.1. CNT EVOLUTION ON THE SUBSTRATE

---

in the isothermal area should be almost the same. According to the above results, it demonstrates that the substrate acts as the 'templet' for anchoring nanoparticles. Only nanoparticles with a certain size are thermal stable on the substrate.



**Figure 4.5.** (a) Raman spectra and (b) the corresponding intensity ratio between D band and G band ( $I_G/I_D$ ) of CNTs grown on quartz plate in the isothermal area at 650 °C.

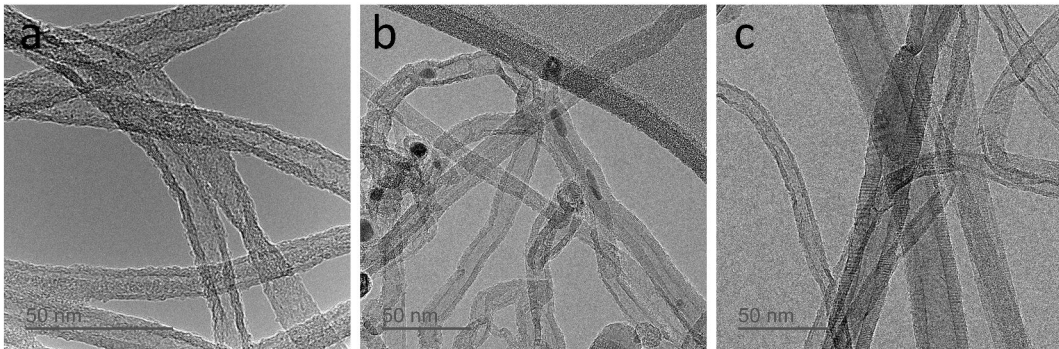


**Figure 4.6.** Typical TEM images of CNTs obtained on the quartz plate at (a) P4, (b) P5 and (c) P6.

CNTs were also synthesized on  $\mu\text{Al}_2\text{O}_3$  at different temperatures. As can be observed in Fig. 4.8a, at 650 °C the highly dense CNTs are found to be well aligned and perpendicular to the  $\mu\text{Al}_2\text{O}_3$  surface at the center of the heated zone (P5). The length of CNTs reaches up to 10-15  $\mu\text{m}$ . When increasing the

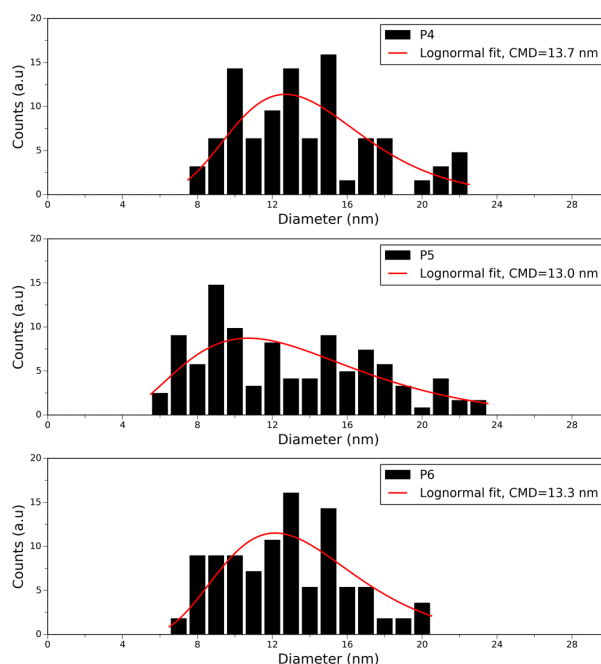


**Figure 4.7.** CNT diameter distribution on quartz plate in the isothermal area.

temperature to 750 °C, less CNTs are observed on the substrate at P5. And they exhibit a poor degree of alignment, short lengths and low density (Fig. 4.8b). At 850 °C, no CNT growth are observed on  $\mu\text{Al}_2\text{O}_3$  at P5 (Fig. 4.8c). Moreover, the yield of CNTs at the center of the heated zone (P5) measured by TGA exhibits a good correlation with observations in the SEM images, as shown in Fig. 4.9. The oxidation temperature for the as-synthesized CNTs is in the range of 400-650 °C. The yield of CNTs declines from 24.4 wt.% to 6.8 wt.% when the temperature increases from 650 °C to 750 °C. Further increase in the temperature to 850 °C, the yield drops to 2.1 wt.%. The output of CNTs on the substrate follows an opposite trend with the mean diameters of nanoparticles in the gas phase. The poor alignment and low yield of CNTs on the substrate at high temperature can be explained as follows. At high temperature, more carbon-encapsulated iron nanoparticles form in the gas phase, which will consume a large number of iron atoms and carbon atoms. Since carbon-encapsulated iron nanoparticles are not

#### 4.1. CNT EVOLUTION ON THE SUBSTRATE

---

responsible for CNT growth on the substrate, the effective iron and carbon are greatly reduced. Less iron will participate in the formation of catalytic iron nanoparticles on the substrate, resulting in the poor alignment and low yield of CNTs on the substrate. It is also emphasized that nanoparticles are not detected at any place in the gas phase at 650 °C. But vertically-aligned CNTs synthesized successfully on the substrate. It further confirms that homogeneous nucleation is not the prerequisite for CNT growth on the substrate. Therefore, there must be another nanoparticle formation mechanism for CNT growth on the substrate.

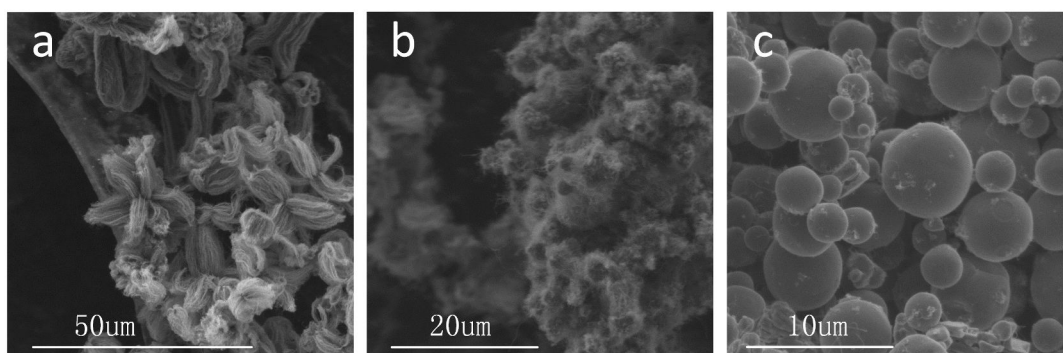


**Figure 4.8.** SEM images of CNTs grown on  $\mu\text{Al}_2\text{O}_3$  at the center of the heated zone (P5) at (a) 650 °C , (b) 750 °C and (c) 850 °C.

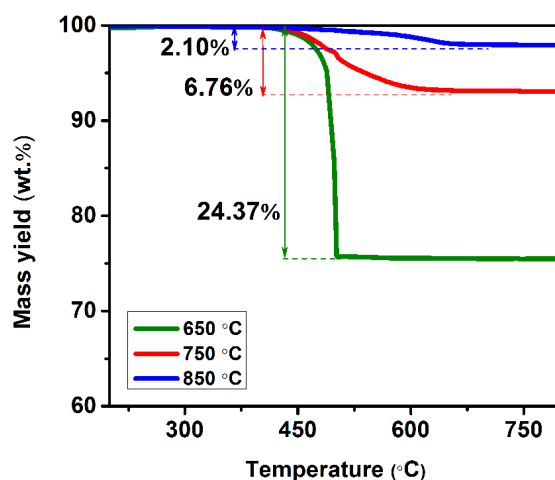


**Figure 4.9.** TGA curves of CNTs synthesized on  $\mu\text{Al}_2\text{O}_3$  at different temperatures.

## 4.2 TWO KINDS OF NANOPARTICLE FORMATION MECHANISMS

According to the above results and discussions, we can deduce that there are two kinds of nanoparticle nucleation mechanisms in FCCVD process (Fig. 4.10). One kind of nanoparticle formation mechanism is homogenous nucleation, which occurs directly in gas phase. Nanoparticles formed by homogenous nucleation are about 4-12 nm. They always are encapsulated by the carbon layer. Another kind of nanoparticle formation mechanism happens on the substrate by heterogeneous nucleation. Nanoparticles formed by heterogeneous nucleation are about 20-35 nm, which are much larger than those in the gas phase at the same position along the reactor. They are utilized as catalysts for the vertical-aligned CNT growth on the substrate in the studied conditions. The different sizes of nanoparticles in gas phase and on the substrate can be explained by the thermodynamics of the nanoparticle nucleation [239]. The relationship between the free energy change to form nanoparticles from the vapour by heterogeneous

## 4.2. TWO KINDS OF NANOPARTICLE FORMATION MECHANISMS

---

nucleation and by homogeneous nucleation can be described by the following equation:

$$G_{hetero} = \frac{1}{4}(1 - \cos\theta)^2(2 + \cos\theta) \cdot G_{homo} \quad (4.1)$$

where  $G_{hetero}$  is the energy needed for forming critical nucleus for heterogeneous nucleation.  $G_{homo}$  is the energy needed for forming critical nucleus for homogenous nucleation.  $\theta$  is the contact angle between the critical nucleus and the substrate. According to Eq. (4.1),  $G_{hetero} < G_{homo}$ . The heterogeneous nucleation can lower the energy barrier. Therefore, the heterogeneous nucleation is always easier than the homogeneous nucleation, which means nanoparticles have a higher opportunity to form on the substrate than in the gas phase. In previous studies, Lu et al. and Elliott et al. observed that the morphology of CVD product strongly depends on the carbon feeding rate [240, 241]. Therefore, In our CVD conditions, a supply of carbon in the initial feedstock with a C/Fe molar ratio of 284 always lets the smaller iron nanoparticles to be encapsulated in the gas phase, but allows the larger nanoparticles to be utilized as the catalysts for CNT growth on the substrate.

As aforementioned, a moderate carbon feeding rate is necessary for CNT growth [240]. Therefore, the C/Fe molar ratio in the initial feedstock is expected to have a great influence on the nanoparticle morphology both in the gas phase and on the substrate. To valid this speculation, CVD was preformed at a low C/Fe molar ratio and a high C/Fe molar ratio, respectively. At a low C/Fe molar of 132, when no  $C_2H_2$  was provided and ferrocene concentration was fixed at 0.1 g/mL. The temperature of the furnace was set to be 750 °C. Interestingly, CNTs directly grow in the gas phase as shown in Fig. 4.11a. The diameter of CNTs is about 11.5 nm (Fig. 4.11b), comparable to the diameters of the iron nanoparticles located at tube ends, but larger than the diameters of

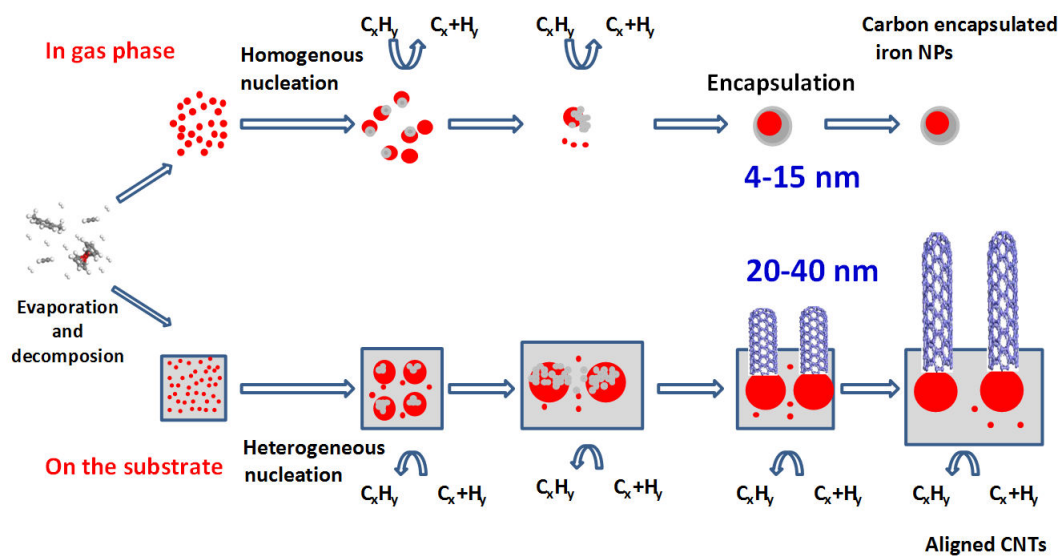


**Figure 4.10.** Proposed models for nanoparticle formation in the gas phase and on the substrate under FCCVD condition.

the abundant carbon encapsulated iron nanoparticles. These lightweight CNTs are easily carried away with the gas flow and deposit at the end of the quartz tube. The results are in agreement with the previous observations [176, 177].

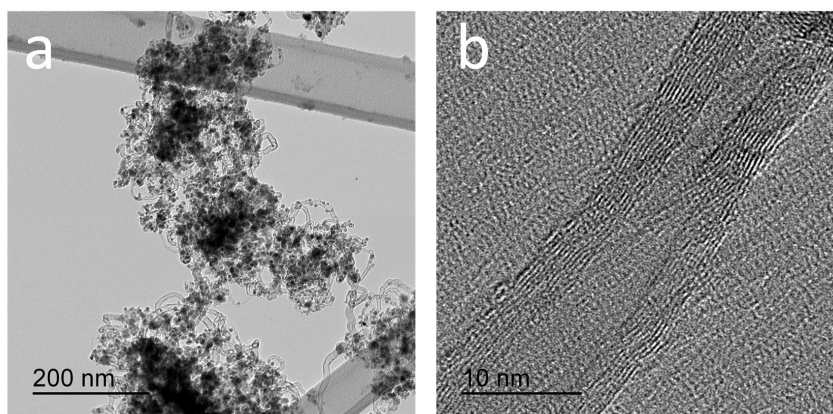


**Figure 4.11.** TEM images of products collected directly in the gas phase under FCCVD condition at a C/Fe molar ratio of 132.

In contrast, the products were also collected on the quartz substrate at a much higher C/Fe molar ratio of 4356. In order to avoid the effect of homoge-

### 4.3. CONCLUSION

---

nous nucleation in the gas phase, CVD was conducted at 650 °C. A solution of 0.01 g/mL ferrocene/xylene was injected into the reactor. Meanwhile, the injection of acetylene as the carbon source was performed at a flow rate 0.4 L/min. The corresponding C/Fe molar ratio is about 4356. The SEM and TEM micrographs of collected powder on the quartz substrate are shown in Fig. 4.12. As can be seen in Fig. 4.12a, no vertically-aligned CNTs were found in the collected powder. TEM results show that the collected powder consists of iron NPs, which are confined by carbon layers (Fig. 4.12b). The diameter of iron NPs is about 8.1 nm, which is much smaller than that of NPs on the substrate at lower C/Fe molar ratio. In addition, the samples were also analyzed by EDS. The typical spectrum is presented in Fig. 4.13a. It indicates that the powder is composed of mainly iron, carbon and copper elements. The HAADF STEM was also performed. The STEM image is shown in Fig. 4.13b, and the map of spatial distribution of iron element in the sample are presented in Fig. 4.13c. It demonstrates that iron nanoparticles on the substrate will also be encapsulated by the carbon layer at a high C/Fe molar ratio in the initial feedstock,. These results confirm our speculation of the two kinds of iron-based NPs nucleation mechanisms in the gas phase and on the substrate.

### 4.3 CONCLUSION

In this chapter, CNTs were synthesized on the substrate at different CVD conditions. According to the morphology of CNTs synthesized on the substrate along the reactor axis, the roles of nanoparticles in the gas phase during CNT synthesis process were discussed. It is found that nanoparticle in the gas phase could not directly contribute to the CNT growth on the substrate. And the

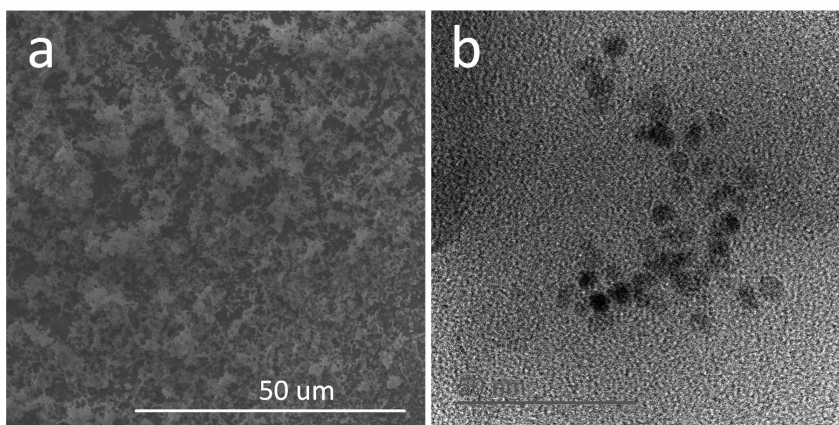


**Figure 4.12.** (a) SEM and (b) TEM image of the products collected on the quartz substrate under FCCVD condition at C/Fe molar ratio of 4356.

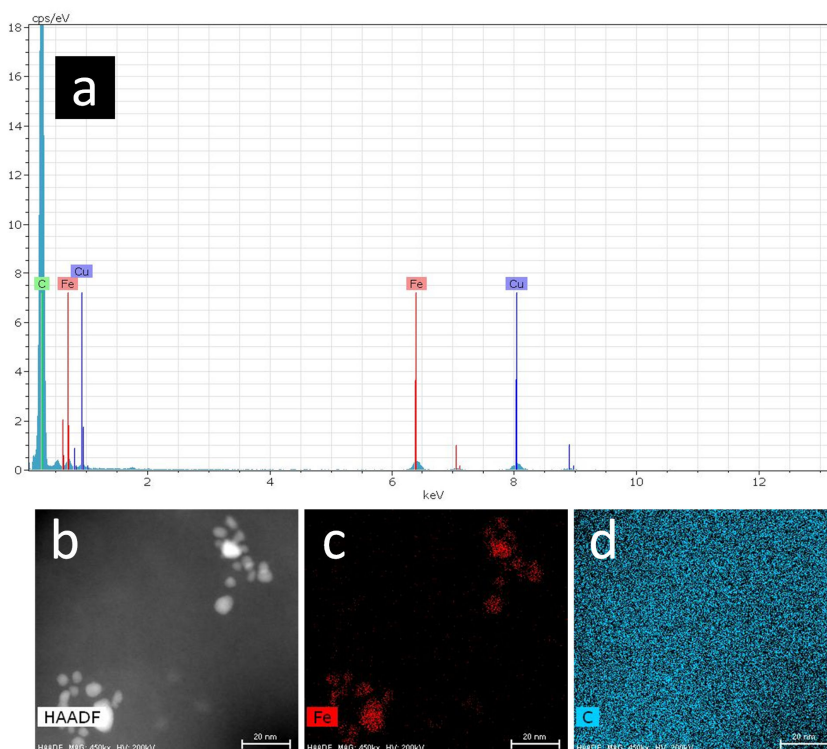


**Figure 4.13.** (a) Spectrum, (b) STEM image and (c) map distribution of chemical elements in the sample of the power.

### 4.3. CONCLUSION

---

different morphology of CVD product in the gas phase and on the substrate can be well explained by the thermodynamics of the nanoparticles nucleation.

# 5

## Conclusions

### 5.1 GENERAL CONCLUSIONS

In the present work, we have provided some contributions to *in-situ* detection of nanoparticles by LII technique during the FCCVD synthesis of CNTs. The main results are concluded as follows:

- **LII technique for *in-situ* monitoring**      An *in-situ* diagnostic technique LII was applied for nanoparticle sizing during the FCCVD synthesis of CNTs. High resolution TEM shows that nanoparticles in the gas phase exhibit a core-shell structure with an iron core and a carbon shell. Therefore, the procedure of calculation of the theoretical LII signal was developed for implementation of LII sizing to carbon-encapsulated iron nanoparticles. A detailed sensitivity and uncertainty of the key parameters on the evaluated particle size for this model was estimated. The results show a strong dependence of the sensitivity and uncertainty on the structure of nanoparticles. In the case of nanoparticles with 1:1 Fe/C mass ratio, according to Sobol sensitivity index,

## 5.1. GENERAL CONCLUSIONS

---

the heat capacity of nanoparticles  $c_p$ , TAC  $\alpha_T$  and the density of nanoparticles  $\rho_p$  are important parameters. The possible deviations caused by the  $\rho_p$  and  $c_p$  are 61.1% and -54.4%. While for nanoparticles with 5:1 Fe/C mass ratio,  $c_p$  and  $\rho_p$  become less important.  $\alpha_T$  becomes the most important parameter. And the uncertainty resulted from  $\rho_p$  and  $c_p$  also decrease to -28.4% and 14.4%. Then the model was also validate by TEM measurements. It is found that the evaluated CMD by LII is in good agreement with the one obtained by TEM measurements. Therefore, LII can be an useful tool for *in-situ* detection of nanoparticles in the gas phase with an acceptable accuracy.

• **Nanoparticle evolution in the gas phase**      The evolution of iron-based nanoparticles in gas phase during the CVD process for CNT synthesis was investigated by combining *in-situ* LII particle sizing and TEM measurements. It was found that homogeneous nucleation really occurs in the gas phase at temperature above 750 °C under the conditions studied and the size of nanoparticles increases quickly in the front of the reactor and keeps constant during the downstream region in the reactor due to carbon encapsulation. The as-formed carbon encapsulated iron nanoparticles exhibit core-shell structures with an  $\alpha$ -Fe core and a carbon shell. And the CVD conditions, such as temperature, CVD duration, ferrocene concentration,  $C_2H_2$  gas flow and  $H_2$  gas flow, have a great influence on the nanoparticle size.

• **Roles of nanoparticles in the gas phase**      By correlating information on the axial nanoparticle evolution and the morphology of CNTs synthesized on the substrate along the reactor axis, the roles of nanoparticles in the gas phase during CNT synthesis process were also discussed. As observed, the nanoparticles in the gas phase are carbon-encapsulated iron particles and their

sizes are far from those on the substrate. In addition, in some situations no nanoparticles formed in the gas phase, but CNTs synthesized successfully at the same location on the substrate. Therefore, it is reasonable to hypothesize that homogeneous nucleation is the dominant mechanism for nanoparticle formation in the gas phase when the saturated vapor pressure was archived, but they could not directly contribute to CNT growth on the substrate. While nanoparticles on the substrate form by heterogeneous nucleation. The substrate plays a key role in promoting nanoparticle nucleation, which results in much larger iron nanoparticles than those in the gas phase. Therefore, In our CVD conditions, a supply of carbon always lets the smaller iron nanoparticles to be encapsulated in the gas phase, but allows the larger NPs to be utilized as the catalysts for CNT growth on the substrate.

## 5.2 PERSPECTIVES

There are many potential extension and perspectives to this work. The following questions would be very interesting for the future research.

- **Laser-induced florescence (LIF)** As mentioned in the thesis, LII is limited to the detection of nanoparticles with the size larger than serval nm. The whole nanoparticle nucleation concerns some fundamental processes, such as decomposition of ferrocene and atoms collision. Thus in order to investigate the early stage of nanoparticle nucleation, another diagnostic technique, by which an atom or selective species could be detected *in-situ*, is highly desired. In this respect, LIF can be very useful for the study of the early stage of the particle nucleation process. The presence of iron atoms and carbon radicals in

the gas phase would confirm the nanoparticle nucleation mechanism.

• **Nanoparticle volume density**      A quantitative analysis for the nanoparticle volume density is critical to understand the ferrocene decomposition and nanoparticle nucleation in the gas phase. LII should be extended to measure the nanoparticle volume density evolution during the CVD process. The LII maximum intensity has been proved to be positively related to the volume density of nanoparticles. Therefore, it is possible to perform a quantitative analysis for the nanoparticles volume density by LII after a calibration.

• **Nanoparticle aggregation**      In Chapter 3 the agglomeration of suspended nanoparticles in the gas phase was observed in the high resolution TEM images. But it is admitted that the particle aggregation was not taken into account in our LII model. Therefore, the size of nanoparticles are overestimated by our LII model. When the point contacts between particles transformed to dense contact, the carbon shells around the whole aggregate represent the resulting particle surface. The particle surface area is responsible for its cooling by collisions with surrounding gas molecules. Hence, the particle cooling process became slower. As a result, LII will overestimate the size of nanoparticles. Hence, the nanoparticle aggregation should be taken into account in the new LII model to decrease the uncertainty.

• **Nanoparticle structure**      The sensitivity and uncertainty of the key parameters in the LII model are strongly depending on the structure of nanoparticles. But the effect of the carbon layer on the thermo-physical properties of nanoparticles was ignored in our LII model and we simply used the density and heat capacity of the bulk iron, which introduces additional uncertainties.

Therefore, the thermo-physical properties of carbon encapsulated iron nanoparticles should be investigated to determine the accurate values of the density and heat capacity in the LII model. Also the C/Fe ratio varies according to the CVD conditions. Thus the effect of CVD parameters on the C/Fe ratio should be studied. It is helpful to elucidate the nanoparticle nucleation mechanism.

• **Gas composition**      In the LII model, the thermal conduction part has the dominant influence on the heat loss. Hence it is important to determine the molecular weight of ambient gas molecules  $\mu_g$  and the ratio of the heat capacity of the gas  $\gamma$ . According to sensitivity and uncertainty analysis, we should pay more attention to  $\gamma$ , because it is more important than  $\mu_g$ . And the maximum deviation caused by  $\gamma$  can reach 40%. In our situation,  $\mu_g$  is in the range of 28.74 (for air) to 39.39 (for argon). While,  $\gamma$  is ranging from 1.39 (for air) to 1.667 (for argon). The exact values vary according to the gas composition and temperature. Therefore, the gas composition should be taken into consideration in the LII model, which can be determined by Mass Spectrometry. The temperature can be accurately measured by the thermocouple.

• **Early stage of the 'real' catalytic nanoparticles**      As proposed in this study, iron nanoparticles in the gas phase generate by homogeneous nucleation from decomposition of ferrocene. Since they will quickly be covered by carbon layer, they do not directly attach to the substrate for CNT growth or aggregate into larger ones for CNT growth. The possible early state of catalyst should be small iron atoms or clusters which were hidden in the ferrocene gas. But they are thermodynamic instability in the studied conditions. They can survive for only a very short time ( $< 1$  ms). Therefore, it is deduced that the real 'catalyst' on the substrate should come from the continuous decomposition

## 5.2. PERSPECTIVES

---

of ferrocene. Along the reactor, ferrocene is gradually consumed. The density of CNTs becomes smaller. And at the rear of the reactor, no ferrocene left. We did not observe the CNT growth. This speculation can be confirmed by detecting ferrocene along the reactor.



# References

- [1] Dong-ming Sun, Marina Y Timmermans, Ying Tian, Albert G Nasibulin, Esko I Kauppinen, Shigeru Kishimoto, Takashi Mizutani, and Yutaka Ohno. Flexible high-performance carbon nanotube integrated circuits. *Nature nanotechnology*, 6(3):156–161, 2011.
- [2] Yongye Liang, Yanguang Li, Hailiang Wang, and Hongjie Dai. Strongly coupled inorganic/nanocarbon hybrid materials for advanced electrocatalysis. *Journal of the American Chemical Society*, 135(6):2013–2036, 2013.
- [3] Stefan Frank, Philippe Poncharal, ZL Wang, and Walt A De Heer. Carbon nanotube quantum resistors. *science*, 280(5370):1744–1746, 1998.
- [4] Phaedon Avouris, Marcus Freitag, and Vasili Perebeinos. Carbon-nanotube photonics and ipoelectronics. *Nature photonics*, 2(6):341–350, 2008.
- [5] Rodrigo V Salvatierra, Carlos E Cava, Lucimara S Roman, and Aldo JG Zarbin. ITO-free and flexible organic photovoltaic device based on high transparent and conductive polyaniline/carbon nanotube thin films. *Advanced Functional Materials*, 23(12):1490–1499, 2013.
- [6] Neetu Jha, Palanisamy Ramesh, Elena Bekyarova, Xiaojuan Tian, Feihu Wang, Mikhail E Itkis, and Robert C Haddon. Functionalized single-walled carbon nanotube-based fuel cell benchmarked against US DOE 2017 technical targets. *Scientific reports*, 3, 2013.
- [7] Anthony B Dichiara, Jinkai Yuan, Shenghong Yao, Alain Sylvestre, Laurent Zimmer, and Jinbo Bai. Effective synergistic effect of  $\text{Al}_2\text{O}_3$  and SiC microparticles on the growth of carbon nanotubes and their application in high dielectric permittivity polymer composites. *Journal of Materials Chemistry A*, 2(21):7980–7987, 2014.
- [8] Albert G Nasibulin, Antti Kaskela, Kimmo Mustonen, Anton S Anisimov, Virginia Ruiz, Samuli Kivisto, Simas Rackauskas, Marina Y Timmermans, Marko Pudas, Brad Aitchison, et al. Multifunctional free-standing single-walled carbon nanotube films. *Acs Nano*, 5(4):3214–3221, 2011.
- [9] Maryam Ahmadzadeh Tofghy and Toraj Mohammadi. Salty water desalination using carbon nanotube sheets. *Desalination*, 258(1):182–186, 2010.

- 
- [10] Weikang Li, Anthony Dichiara, and Jinbo Bai. Carbon nanotube–graphene nanoplatelet hybrids as high-performance multifunctional reinforcements in epoxy composites. *Composites Science and Technology*, 74:221–227, 2013.
- [11] Qiang Zhang, Jia-Qi Huang, Wei-Zhong Qian, Ying-Ying Zhang, and Fei Wei. The road for nanomaterials industry: A review of carbon nanotube production, post-treatment, and bulk applications for composites and energy storage. *Small*, 9(8):1237–1265, 2013.
- [12] Sumio Iijima. Helical microtubules of graphitic carbon. *Nature*, 354(6348):56, 1991.
- [13] Andreas Thess, Roland Lee, Pavel Nikolaev, Hongjie Dai, Pierre Petit, Jerome Robert, Chunhui Xu, Young Hee Lee, Seong Gon Kim, Andrew G Rinzler, et al. Crystalline ropes of metallic carbon nanotubes. *Science*, 273(5274):483–487, 1996.
- [14] M José-Yacamán, M Miki-Yoshida, L Rendon, and JG Santiesteban. Catalytic growth of carbon microtubules with fullerene structure. *Applied physics letters*, 62(6):657–659, 1993.
- [15] Hongjie Dai. Carbon nanotubes: opportunities and challenges. *Surface Science*, 500(1-3):218–241, 2002.
- [16] Roberto Guzmán de Villoria, A John Hart, and Brian L Wardle. Continuous high-yield production of vertically aligned carbon nanotubes on 2D and 3D substrates. *ACS nano*, 5(6):4850–4857, 2011.
- [17] Takeo Yamada, Alan Maigne, Masako Yudasaka, Kouhei Mizuno, Don N Futaba, Motoo Yumura, Sumio Iijima, and Kenji Hata. Revealing the secret of water-assisted carbon nanotube synthesis by microscopic observation of the interaction of water on the catalysts. *Nano letters*, 8(12):4288–4292, 2008.
- [18] Albert G Nasibulin, Peter V Pikhitsa, Hua Jiang, and Esko I Kauppinen. Correlation between catalyst particle and single-walled carbon nanotube diameters. *Carbon*, 43(11):2251–2257, 2005.
- [19] Yiming Li, Woong Kim, Yuegang Zhang, Marco Rolandi, Dunwei Wang, and Hongjie Dai. Growth of single-walled carbon nanotubes from discrete catalytic nanoparticles of various sizes. *The Journal of Physical Chemistry B*, 105(46):11424–11431, 2001.
- [20] Cheol-Hun Lee, Jaegeun Lee, Sunmog Yeo, Sung-Hyun Lee, Teawon Kim, Hyeon-Gu Cha, Youngmoo Eun, Hyun Jin Park, Seung Min Kim, and Kun-Hong Lee. Evolution of implanted Fe ions in SiO<sub>2</sub>/Si wafer into uniformly sized catalyst particles for carbon nanotube forest growth. *Carbon*, 123:122–128, 2017.

## REFERENCES

---

- [21] Fei Yu, Mingxuan Yang, Fanglin Li, Chang Su, Buyong Ma, Zhiwen Yuan, Junhong Chen, and Jie Ma. The growth mechanism of single-walled carbon nanotubes with a controlled diameter. *Physica E: Low-dimensional Systems and Nanostructures*, 44(10):2032–2040, 2012.
- [22] Gilbert D Nessim, A John Hart, Jin S Kim, Donatello Acquaviva, Jihun Oh, Caitlin D Morgan, Matteo Seita, Jeffrey S Leib, and Carl V Thompson. Tuning of vertically-aligned carbon nanotube diameter and areal density through catalyst pre-treatment. *Nano Letters*, 8(11):3587–3593, 2008.
- [23] Randy L Vander Wal, Thomas M Ticich, and A Brock Stephens. Can soot primary particle size be determined using laser-induced incandescence? *Combustion and flame*, 116(1-2):291–296, 1999.
- [24] Lynn A Melton. Soot diagnostics based on laser heating. *Applied optics*, 23(13):2201–2208, 1984.
- [25] Stefan Will, Stephan Schraml, and Alfred Leipertz. Two-dimensional soot-particle sizing by time-resolved laser-induced incandescence. *Optics letters*, 20(22):2342–2344, 1995.
- [26] Stefan Will, Stephan Schraml, and Alfred Leipert. Comprehensive two-dimensional soot diagnostics based on laser-induced incandescence (LII). *Symposium (International) on Combustion*, 26(2):2277 – 2284, 1996.
- [27] Boris F Kock, Benjamin Tribalet, Christof Schulz, and Paul Roth. Two-color time-resolved LII applied to soot particle sizing in the cylinder of a diesel engine. *Combustion and Flame*, 147(1-2):79–92, 2006.
- [28] Christof Schulz, Boris F Kock, Max Hofmann, Hope Michelsen, Stefan Will, Bas Bougie, Rainer Suntz, and Greg Smallwood. Laser-induced incandescence: recent trends and current questions. *Applied Physics B*, 83(3):333, 2006.
- [29] Alfred Leipertz and Stefan Dankers. Characterization of nano-particles using laser-induced incandescence. *Particle & Particle Systems Characterization*, 20(2):81–93, 2003.
- [30] Randall L Vander Wal, Thomas M Ticich, and Joseph R West. Laser-induced incandescence applied to metal nanostructures. *Applied optics*, 38(27):5867–5879, 1999.
- [31] R Starke, B Kock, and Paul Roth. Nano-particle sizing by laser-induced-incandescence (LII) in a shock wave reactor. *Shock waves*, 12(5):351–360, 2003.
- [32] A Eremin, E Gurentsov, and Ch Schulz. Influence of the bath gas on the condensation of supersaturated iron atom vapour at room temperature. *Journal of Physics D: Applied Physics*, 41(5):055203, 2008.

- 
- [33] AV Eremin, EV Gurentsov, and SA Musikhin. Synthesis of binary iron-carbon nanoparticles by UV laser photolysis of  $\text{Fe}(\text{CO})_5$  with various hydrocarbons. *Materials Research Express*, 3(10):105041, 2016.
- [34] AV Eremin, EV Gurentsov, and SA Musikhin. Temperature influence on the properties of carbon-encapsulated iron nanoparticles forming in pyrolysis of gaseous precursors. *Journal of Alloys and Compounds*, 727:711–720, 2017.
- [35] Peter Harris. On charcoal. *Interdisciplinary Science Reviews*, 24(4):301–306, 1999.
- [36] John Emsley. *Nature's building blocks: an AZ guide to the elements*. Oxford University Press, 2011.
- [37] Michael J O'connell. *Carbon nanotubes: properties and applications*. CRC press, 2006.
- [38] FP Bundy, WA Bassett, MS Weathers, RJ Hemley, HU Mao, and AF Goncharov. The pressure-temperature phase and transformation diagram for carbon; updated through 1994. *Carbon*, 34(2):141–153, 1996.
- [39] Lanhua Wei, PK Kuo, RL Thomas, TR Anthony, and WF Banholzer. Thermal conductivity of isotopically modified single crystal diamond. *Physical Review Letters*, 70(24):3764, 1993.
- [40] John Walker. Optical absorption and luminescence in diamond. *Reports on Progress in Physics*, 42(10):1605, 1979.
- [41] Harold W Kroto, James R Heath, Sean C O'Brien, Robert F Curl, and Richard E Smalley.  $\text{C}_{60}$ : Buckminsterfullerene. *Nature*, 318(6042):162, 1985.
- [42] Wolfgang Krätschmer, Lowell D Lamb, K Fostiropoulos, and Donald R Huffman. Solid  $\text{C}_{60}$ : a new form of carbon. *Nature*, 347(6291):354, 1990.
- [43] DS Bethune, Ch H Kiang, MS De Vries, G Gorman, R Savoy, J Vazquez, and R Beyers. Cobalt-catalysed growth of carbon nanotubes with single-atomic-layer walls. *Nature*, 363(6430):605, 1993.
- [44] Sumio Iijima and Toshinari Ichihashi. Single-shell carbon nanotubes of 1-nm diameter. *Nature*, 363(6430):603, 1993.
- [45] Jeroen WG Wilder, Liesbeth C Venema, Andrew G Rinzler, Richard E Smalley, and Cees Dekker. Electronic structure of atomically resolved carbon nanotubes. *Nature*, 391(6662):59, 1998.
- [46] Morinobu Endo, Michael S Strano, and Pulickel M Ajayan. Potential applications of carbon nanotubes. In *Carbon nanotubes*, pages 13–62. Springer, 2007.

## REFERENCES

---

- [47] Riichiro Saito, Mitsutaka Fujita, Gene Dresselhaus, and Mildred S Dresselhaus. Electronic structure of graphene tubules based on  $C_{60}$ . *Physical Review B*, 46(3):1804, 1992.
- [48] Min Ouyang, Jin-Lin Huang, and Charles M Lieber. Fundamental electronic properties and applications of single-walled carbon nanotubes. *Accounts of chemical research*, 35(12):1018–1025, 2002.
- [49] Sander J Tans, Michel H Devoret, Hongjie Dai, Andreas Thess, Richard E Smalley, LJ Geerligs, and Cees Dekker. Individual single-wall carbon nanotubes as quantum wires. *Nature*, 386(6624):474, 1997.
- [50] Stefano Sanvito, Young-Kyun Kwon, David Tománek, and Colin J Lambert. Fractional quantum conductance in carbon nanotubes. *Physical Review Letters*, 84(9):1974, 2000.
- [51] C Berger, Y Yi, ZL Wang, and WA De Heer. Multiwalled carbon nanotubes are ballistic conductors at room temperature. *Applied Physics A*, 74(3):363–365, 2002.
- [52] DH Robertson, DW Brenner, and JW Mintmire. Energetics of nanoscale graphitic tubules. *Physical Review B*, 45(21):12592, 1992.
- [53] MM JEBBESSEN Treacy, TW Ebbesen, and JM Gibson. Exceptionally high young’s modulus observed for individual carbon nanotubes. *Nature*, 381(6584):678, 1996.
- [54] RL Jacobsen, TM Tritt, JR Guth, AC Ehrlich, and DJ Gillespie. Mechanical properties of vapor-grown carbon fiber. *Carbon*, 33(9):1217–1221, 1995.
- [55] A Krishnan, E Dujardin, TW Ebbesen, PN Yianilos, and MMJ Treacy. Young’s modulus of single-walled nanotubes. *Physical review B*, 58(20):14013, 1998.
- [56] Eric W Wong, Paul E Sheehan, and Charles M Lieber. Nanobeam mechanics: elasticity, strength, and toughness of nanorods and nanotubes. *science*, 277(5334):1971–1975, 1997.
- [57] Min-Feng Yu, Bradley S Files, Sivaram Arepalli, and Rodney S Ruoff. Tensile loading of ropes of single wall carbon nanotubes and their mechanical properties. *Physical review letters*, 84(24):5552, 2000.
- [58] Min-Feng Yu, Oleg Lourie, Mark J Dyer, Katerina Moloni, Thomas F Kelly, and Rodney S Ruoff. Strength and breaking mechanism of multiwalled carbon nanotubes under tensile load. *Science*, 287(5453):637–640, 2000.
- [59] Jean-Paul Salvetat-Delmotte and Angel Rubio. Mechanical properties of carbon nanotubes: a fiber digest for beginners. *Carbon*, 40(10):1729–1734, 2002.

- 
- [60] Jian Ping Lu. Elastic properties of carbon nanotubes and nanoropes. *Physical Review Letters*, 79(7):1297, 1997.
- [61] Boris I Yakobson, CJ Brabec, and J Bernholc. Nanomechanics of carbon tubes: instabilities beyond linear response. *Physical review letters*, 76(14):2511, 1996.
- [62] CF Cornwell and LT Wille. Elastic properties of single-walled carbon nanotubes in compression. *Solid State Communications*, 101(8):555–558, 1997.
- [63] E Hernandez, C Goze, P Bernier, and A Rubio. Elastic properties of C and  $B_xC_yN_z$  composite nanotubes. *Physical Review Letters*, 80(20):4502, 1998.
- [64] Daniel Sánchez-Portal, Emilio Artacho, José M Soler, Angel Rubio, and Pablo Ordejón. *Ab initio* structural, elastic, and vibrational properties of carbon nanotubes. *Physical Review B*, 59(19):12678, 1999.
- [65] W Yi, L Lu, Zhang Dian-Lin, ZW Pan, and SS Xie. Linear specific heat of carbon nanotubes. *Physical Review B*, 59(14):R9015, 1999.
- [66] Ari Mizel, Lorin X Benedict, Marvin L Cohen, Steven G Louie, A Zettl, Nasser K Budraa, and WP Beyermann. Analysis of the low-temperature specific heat of multiwalled carbon nanotubes and carbon nanotube ropes. *Physical Review B*, 60(5):3264, 1999.
- [67] J Hone, B Batlogg, Z Benes, AT Johnson, and JE Fischer. Quantized phonon spectrum of single-wall carbon nanotubes. *Science*, 289(5485):1730–1733, 2000.
- [68] Jean-Claude Lasjaunias, Katica Biljaković, Zdenek Benes, JE Fischer, and Pierre Monceau. Low-temperature specific heat of single-wall carbon nanotubes. *Physical Review B*, 65(11):113409, 2002.
- [69] James Hone, M Whitney, C Piskoti, and A Zettl. Thermal conductivity of single-walled carbon nanotubes. *Physical Review B*, 59(4):R2514, 1999.
- [70] Philip Kim, Li Shi, Arun Majumdar, and Paul L McEuen. Thermal transport measurements of individual multiwalled nanotubes. *Physical review letters*, 87(21):215502, 2001.
- [71] Lorin X Benedict, Steven G Louie, and Marvin L Cohen. Heat capacity of carbon nanotubes. *Solid State Communications*, 100(3):177–180, 1996.
- [72] Valentin N Popov. Low-temperature specific heat of nanotube systems. *Physical Review B*, 66(15):153408, 2002.
- [73] Young-Kyun Kwon, Susumu Saito, and David Tománek. Effect of intertube coupling on the electronic structure of carbon nanotube ropes. *Physical Review B*, 58(20):R13314, 1998.

## REFERENCES

---

- [74] Randall L Vander Wal, Thomas M Ticich, and Valerie E Curtis. Diffusion flame synthesis of single-walled carbon nanotubes. *Chemical Physics Letters*, 323(3-4):217–223, 2000.
- [75] Liming Yuan, Kozo Saito, Chunxu Pan, FA Williams, and AS Gordon. Nanotubes from methane flames. *Chemical physics letters*, 340(3-4):237–241, 2001.
- [76] Liming Yuan, Kozo Saito, Wenchong Hu, and Zhi Chen. Ethylene flame synthesis of well-aligned multi-walled carbon nanotubes. *Chemical physics letters*, 346(1-2):23–28, 2001.
- [77] WK Hsu, M Terrones, JP Hare, H Terrones, HW Kroto, and DRM Walton. Electrolytic formation of carbon nanostructures. *Chemical Physics Letters*, 262(1-2):161–166, 1996.
- [78] JB Bai, A-L Hamon, A Marraud, B Jouffrey, and V Zymla. Synthesis of SWNTs and MWNTs by a molten salt (NaCl) method. *Chemical physics letters*, 365(1-2):184–188, 2002.
- [79] John H Lehman, Mauricio Terrones, Elisabeth Mansfield, Katherine E Hurst, and Vincent Meunier. Evaluating the characteristics of multiwall carbon nanotubes. *Carbon*, 49(8):2581–2602, 2011.
- [80] Woo-Seok Cho, Etsuo Hamada, Yukihiro Kondo, and Kunio Takayanagi. Synthesis of carbon nanotubes from bulk polymer. *Applied physics letters*, 69(2):278–279, 1996.
- [81] YL Li, YD Yu, and Y Liang. A novel method for synthesis of carbon nanotubes: low temperature solid pyrolysis. *Journal of materials research*, 12(7):1678–1680, 1997.
- [82] Yoshinori Ando, Xinluo Zhao, Toshiki Sugai, and Mukul Kumar. Growing carbon nanotubes. *Materials today*, 7(10):22–29, 2004.
- [83] M Ishigami, John Cumings, A Zettl, and S Chen. A simple method for the continuous production of carbon nanotubes. *Chemical physics letters*, 319(5-6):457–459, 2000.
- [84] Xing Gang, Jia Shenli, Xing Jian, and Shi Zongqian. Analysis of the carbon nano-structures formation in liquid arcing. *Plasma Science and Technology*, 9(6):770, 2007.
- [85] Yahachi Saito, Keishi Nishikubo, Kenichiro Kawabata, and Takehisa Matsumoto. Carbon nanocapsules and single-layered nanotubes produced with platinum-group metals (Ru, Rh, Pd, Os, Ir, Pt) by arc discharge. *Journal of applied physics*, 80(5):3062–3067, 1996.

- [86] Ting Guo, Pavel Nikolaev, Andrew G Rinzler, David Tomanek, Daniel T Colbert, and Richard E Smalley. Self-assembly of tubular fullerenes. *The Journal of Physical Chemistry*, 99(27):10694–10697, 1995.
- [87] Ting Guo, Pavel Nikolaev, Andreas Thess, Daniel T Colbert, and Richard E Smalley. Catalytic growth of single-walled nanotubes by laser vaporization. *Chemical physics letters*, 243(1-2):49–54, 1995.
- [88] Jean-Philippe Tessonier and Dang Sheng Su. Recent progress on the growth mechanism of carbon nanotubes: a review. *ChemSusChem*, 4(7):824–847, 2011.
- [89] WZ Li, SS Xie, Li X Qian, BH Chang, BS Zou, WY Zhou, RA Zhao, and G Wang. Large-scale synthesis of aligned carbon nanotubes. *Science*, 274(5293):1701–1703, 1996.
- [90] Cheol Jin Lee, Jeunghee Park, Yoon Huh, and Jeong Yong Lee. Temperature effect on the growth of carbon nanotubes using thermal chemical vapor deposition. *Chemical Physics Letters*, 343(1-2):33–38, 2001.
- [91] R Andrews, D Jacques, AM Rao, F Derbyshire, D Qian, X Fan, EC Dickey, and J Chen. Continuous production of aligned carbon nanotubes: a step closer to commercial realization. *Chemical physics letters*, 303(5-6):467–474, 1999.
- [92] Jan Prasek, Jana Drbohlavova, Jana Chomoucka, Jaromir Hubalek, Ondrej Jasek, Vojtech Adam, and Rene Kizek. Methods for carbon nanotubes synthesis. *Journal of Materials Chemistry*, 21(40):15872–15884, 2011.
- [93] Emmanuel Flahaut, Achutharao Govindaraj, Alain Peigney, Ch Laurent, Abel Rousset, and Chintamani Nagesa Ramachandra Rao. Synthesis of single-walled carbon nanotubes using binary (Fe, Co, Ni) alloy nanoparticles prepared *in-situ* by the reduction of oxide solid solutions. *Chemical Physics Letters*, 300(1):236–242, 1999.
- [94] Chris Bower, Otto Zhou, Wei Zhu, DJ Werder, and Sungho Jin. Nucleation and growth of carbon nanotubes by microwave plasma chemical vapor deposition. *Applied Physics Letters*, 77(17):2767–2769, 2000.
- [95] HM Cheng, Feng Li, Ge Su, HY Pan, LL He, X Sun, and MS Dresselhaus. Large-scale and low-cost synthesis of single-walled carbon nanotubes by the catalytic pyrolysis of hydrocarbons. *Applied Physics Letters*, 72(25):3282–3284, 1998.
- [96] Vincent Jourdain and Christophe Bichara. Current understanding of the growth of carbon nanotubes in catalytic chemical vapour deposition. *Carbon*, 58:2–39, 2013.
- [97] Wilson Merchan-Merchan, Alexei V Saveliev, Lawrence Kennedy, and Walmy Cuello Jimenez. Combustion synthesis of carbon nanotubes and related

## REFERENCES

---

- nanostructures. *Progress in Energy and Combustion Science*, 36(6):696–727, 2010.
- [98] Yo-Sep Min, Eun Ju Bae, Byung Seok Oh, Donghun Kang, and Wanjun Park. Low-temperature growth of single-walled carbon nanotubes by water plasma chemical vapor deposition. *Journal of the American Chemical Society*, 127(36):12498–12499, 2005.
- [99] S Hofmann, C Ducati, J Robertson, and B Kleinsorge. Low-temperature growth of carbon nanotubes by plasma-enhanced chemical vapor deposition. *Applied Physics Letters*, 83(1):135–137, 2003.
- [100] CNR Rao and Rahul Sen. Large aligned-nanotube bundles from ferrocene pyrolysis. *Chemical Communications*, 0(15):1525–1526, 1998.
- [101] Pavel Nikolaev, Michael J Bronikowski, R Kelley Bradley, Frank Rohmund, Daniel T Colbert, KA Smith, and Richard E Smalley. Gas-phase catalytic growth of single-walled carbon nanotubes from carbon monoxide. *Chemical physics letters*, 313(1-2):91–97, 1999.
- [102] Guangfeng Hou, Ruitao Su, Anli Wang, Vianessa Ng, Weifeng Li, Yi Song, Lu Zhang, Murali Sundaram, Vesselin Shanov, David Mast, et al. The effect of a convection vortex on sock formation in the floating catalyst method for carbon nanotube synthesis. *Carbon*, 102:513–519, 2016.
- [103] Anastasiia Mikhalech, Zeng Fan, Thang Q Tran, Peng Liu, Vincent BC Tan, Tong-Earn Tay, and Hai M Duong. Continuous and scalable fabrication and multifunctional properties of carbon nanotube aerogels from the floating catalyst method. *Carbon*, 102:409–418, 2016.
- [104] Ming Su, Bo Zheng, and Jie Liu. A scalable cvd method for the synthesis of single-walled carbon nanotubes with high catalyst productivity. *Chemical Physics Letters*, 322(5):321–326, 2000.
- [105] A Kukovecz, Z Konya, N Nagaraaju, I Willems, A Tamasi, A Fonseca, JB Nagy, and I Kiricsi. Catalytic synthesis of carbon nanotubes over Co, Fe and Ni containing conventional and sol-gel silica-aluminas. *Physical Chemistry Chemical Physics*, 2(13):3071–3076, 2000.
- [106] Danielle K Smith, Doh C Lee, and Brian A Korgel. High yield multiwall carbon nanotube synthesis in supercritical fluids. *Chemistry of materials*, 18(14):3356–3364, 2006.
- [107] Rong Xiang, Guohua Luo, Zhou Yang, Qiang Zhang, Weizhong Qian, and Fei Wei. Large area growth of aligned CNT arrays on spheres: cost performance and product control. *Materials Letters*, 63(1):84–87, 2009.

- 
- [108] Mukul Kumar and Yoshinori Ando. Chemical vapor deposition of carbon nanotubes: a review on growth mechanism and mass production. *Journal of nanoscience and nanotechnology*, 10(6):3739–3758, 2010.
- [109] RS Wagner and WC Ellis. Vapor-liquid-solid mechanism of single crystal growth. *Applied Physics Letters*, 4(5):89–90, 1964.
- [110] RTK Baker, MA Barber, PS Harris, FS Feates, and RJ Waite. Nucleation and growth of carbon deposits from the nickel catalyzed decomposition of acetylene. *Journal of catalysis*, 26(1):51–62, 1972.
- [111] SB Sinnott, R Andrews, D Qian, Apparao M Rao, Z Mao, EC Dickey, and F Derbyshire. Model of carbon nanotube growth through chemical vapor deposition. *Chemical Physics Letters*, 315(1-2):25–30, 1999.
- [112] RTK Baker, PS Harris, RB Thomas, and RJ Waite. Formation of filamentous carbon from iron, cobalt and chromium catalyzed decomposition of acetylene. *Journal of catalysis*, 30(1):86–95, 1973.
- [113] Ki-Eun Kim, Kang-Jin Kim, Woo Sung Jung, Seung Yong Bae, Jeunghee Park, Junghyun Choi, and Jaebum Choo. Investigation on the temperature-dependent growth rate of carbon nanotubes using chemical vapor deposition of ferrocene and acetylene. *Chemical physics letters*, 401(4-6):459–464, 2005.
- [114] EL Evans, JM Thomas, PA Thrower, and PL Walker. Growth of filamentary carbon on metallic surfaces during the pyrolysis of methane and acetone. *Carbon*, 11(5):441–445, 1973.
- [115] Gary G Tibbetts. Why are carbon filaments tubular? *Journal of crystal growth*, 66(3):632–638, 1984.
- [116] Ming Lin, Joyce Pei Ying Tan, Chris Boothroyd, Kian Ping Loh, Eng Soon Tok, and Yong-Lim Foo. Dynamical observation of bamboo-like carbon nanotube growth. *Nano Letters*, 7(8):2234–2238, 2007.
- [117] Jing Kong, Alan M Cassell, and Hongjie Dai. Chemical vapor deposition of methane for single-walled carbon nanotubes. *Chemical Physics Letters*, 292(4-6):567–574, 1998.
- [118] Teresa de los Arcos, Michael Gunnar Garnier, Jin Won Seo, Peter Oelhafen, Verena Thommen, and Daniel Mathys. The influence of catalyst chemical state and morphology on carbon nanotube growth. *The Journal of Physical Chemistry B*, 108(23):7728–7734, 2004.
- [119] Vasile Heresanu, Celia Castro, Julien Cambedouzou, Mathieu Pinault, Odile Stephan, Cécile Reynaud, Martine Mayne-L’Hermite, and Pascale Launois. Nature of the catalyst particles in CCVD synthesis of multiwalled carbon nanotubes revealed by the cooling step study. *The Journal of Physical Chemistry C*, 112(19):7371–7378, 2008.

## REFERENCES

---

- [120] Daisuke Takagi, Yoshikazu Homma, Hiroki Hibino, Satoru Suzuki, and Yoshihiro Kobayashi. Single-walled carbon nanotube growth from highly activated metal nanoparticles. *Nano letters*, 6(12):2642–2645, 2006.
- [121] Santiago Esconjauregui, Caroline M Whelan, and Karen Maex. The reasons why metals catalyze the nucleation and growth of carbon nanotubes and other carbon nanomorphologies. *Carbon*, 47(3):659–669, 2009.
- [122] Mami Yamada, Masa-aki Kawana, and Mikio Miyake. Synthesis and diameter control of multi-walled carbon nanotubes over gold nanoparticle catalysts. *Applied Catalysis A: General*, 302(2):201–207, 2006.
- [123] Yong Qian, Chunyan Wang, Guangyuan Ren, and Bin Huang. Surface growth of single-walled carbon nanotubes from ruthenium nanoparticles. *Applied Surface Science*, 256(12):4038–4041, 2010.
- [124] Weiwei Zhou, Zuoyan Han, Jinyong Wang, Yan Zhang, Zhong Jin, Xiao Sun, Yawen Zhang, Chunhua Yan, and Yan Li. Copper catalyzing growth of single-walled carbon nanotubes on substrates. *Nano letters*, 6(12):2987–2990, 2006.
- [125] Bilu Liu, Wencai Ren, Libo Gao, Shisheng Li, Qingfeng Liu, Chuanbin Jiang, and Hui-Ming Cheng. Manganese-catalyzed surface growth of single-walled carbon nanotubes with high efficiency. *The Journal of Physical Chemistry C*, 112(49):19231–19235, 2008.
- [126] Yan Li, Rongli Cui, Lei Ding, Yu Liu, Weiwei Zhou, Yan Zhang, Zhong Jin, Fei Peng, and Jie Liu. How catalysts affect the growth of single-walled carbon nanotubes on substrates. *Advanced Materials*, 22(13):1508–1515, 2010.
- [127] Dongning Yuan, Lei Ding, Haibin Chu, Yiyu Feng, Thomas P McNicholas, and Jie Liu. Horizontally aligned single-walled carbon nanotube on quartz from a large variety of metal catalysts. *Nano letters*, 8(8):2576–2579, 2008.
- [128] Alicja Bachmatiuk, Felix Börrnert, Mandy Grobosch, Franziska Schäffel, Ulrike Wolff, Andrew Scott, Mujtaba Zaka, Jamie H Warner, Rüdiger Klingeler, Martin Knupfer, et al. Investigating the graphitization mechanism of SiO<sub>2</sub> nanoparticles in chemical vapor deposition. *Acs Nano*, 3(12):4098–4104, 2009.
- [129] Bilu Liu, Wencai Ren, Libo Gao, Shisheng Li, Songfeng Pei, Chang Liu, Chuanbin Jiang, and Hui-Ming Cheng. Metal-catalyst-free growth of single-walled carbon nanotubes. *Journal of the American Chemical Society*, 131(6):2082–2083, 2009.
- [130] Shaoming Huang, Qiran Cai, Jiangying Chen, Yong Qian, and Lijie Zhang. Metal-catalyst-free growth of single-walled carbon nanotubes on substrates. *Journal of the American Chemical Society*, 131(6):2094–2095, 2009.

- 
- [131] Fenglei Gao, Lijie Zhang, and Shaoming Huang. Zinc oxide catalyzed growth of single-walled carbon nanotubes. *Applied Surface Science*, 256(8):2323–2326, 2010.
- [132] Wei-Hung Chiang and R Mohan Sankaran. Linking catalyst composition to chirality distributions of as-grown single-walled carbon nanotubes by tuning  $\text{Ni}_x\text{Fe}_{1-x}$  nanoparticles. *Nature materials*, 8(11):882, 2009.
- [133] Hee Jin Jeong, Seung Yol Jeong, Young Min Shin, Jeong Ho Han, Seong Chu Lim, Sung Jin Eum, Cheol Woong Yang, Nam-gyun Kim, Chong-Yun Park, and Young Hee Lee. Dual-catalyst growth of vertically aligned carbon nanotubes at low temperature in thermal chemical vapor deposition. *Chemical Physics Letters*, 361(3-4):189–195, 2002.
- [134] Régis Philippe, Brigitte Caussat, Andrea Falqui, Yolande Kihn, Philippe Kalck, Serge Bordère, Dominique Plee, Patrice Gaillard, Daniel Bernard, and Philippe Serp. An original growth mode of MWCNTs on alumina supported iron catalysts. *Journal of Catalysis*, 263(2):345–358, 2009.
- [135] Renu Sharma, Edward Moore, Peter Rez, and Michael MJ Treacy. Site-specific fabrication of Fe particles for carbon nanotube growth. *Nano letters*, 9(2):689–694, 2009.
- [136] Christoph T Wirth, Bernhard C Bayer, Andrew D Gamalski, Santiago Esconjauregui, Robert S Weatherup, Caterina Ducati, Carsten Baehtz, John Robertson, and Stephan Hofmann. The phase of iron catalyst nanoparticles during carbon nanotube growth. *Chemistry of Materials*, 24(24):4633–4640, 2012.
- [137] Stefano Mazzucco, Ying Wang, Mihaela Tanase, Matthieu Picher, Kai Li, Zhi-jian Wu, Stephan Irle, and Renu Sharma. Direct evidence of active and inactive phases of Fe catalyst nanoparticles for carbon nanotube formation. *Journal of Catalysis*, 319:54–60, 2014.
- [138] Hideto Yoshida, Seiji Takeda, Tetsuya Uchiyama, Hideo Kohno, and Yoshikazu Homma. Atomic-scale *in-situ* observation of carbon nanotube growth from solid state iron carbide nanoparticles. *Nano letters*, 8(7):2082–2086, 2008.
- [139] QS Mei and K Lu. Melting and superheating of crystalline solids: From bulk to nanocrystals. *Progress in Materials Science*, 52(8):1175–1262, 2007.
- [140] M Audier, A Oberlin, and M Coulon. Crystallographic orientations of catalytic particles in filamentous carbon; case of simple conical particles. *Journal of Crystal Growth*, 55(3):549–556, 1981.
- [141] Stig Helveg, Carlos Lopez-Cartes, Jens Sehested, Poul L Hansen, Bjerne S Clausen, Jens R Rostrup-Nielsen, Frank Abild-Pedersen, and Jens K Nørskov. Atomic-scale imaging of carbon nanofibre growth. *Nature*, 427(6973):426, 2004.

## REFERENCES

---

- [142] Stephan Hofmann, Raoul Blume, Christoph T Wirth, Mirco Cantoro, Renu Sharma, Caterina Ducati, Michael Hövecker, Spiros Zafeiratos, Peter Schnorcher, Andreas Oestereich, et al. State of transition metal catalysts during carbon nanotube growth. *The Journal of Physical Chemistry C*, 113(5):1648–1656, 2009.
- [143] Stephan Hofmann, Renu Sharma, Caterina Ducati, Gaohui Du, Cecilia Mattevi, Cinzia Cepek, Mirco Cantoro, Simone Pisana, Atlus Parvez, Felipe Cervantes-Sodi, et al. *In situ* observations of catalyst dynamics during surface-bound carbon nanotube nucleation. *Nano letters*, 7(3):602–608, 2007.
- [144] Agnes Oberlin, M Endo, and T Koyama. Filamentous growth of carbon through benzene decomposition. *Journal of crystal growth*, 32(3):335–349, 1976.
- [145] RT Yang and JP Chen. Mechanism of carbon filament growth on metal catalysts. *Journal of Catalysis*, 115(1):52–64, 1989.
- [146] Hansoo Kim, Michael J Kaufman, Wolfgang M Sigmund, David Jacques, and Rodney Andrews. Observation and formation mechanism of stable face-centered-cubic fe nanorods in carbon nanotubes. *Journal of materials research*, 18(5):1104–1108, 2003.
- [147] S Hofmann, G Csanyi, AC Ferrari, MC Payne, and J Robertson. Surface diffusion: the low activation energy path for nanotube growth. *Physical review letters*, 95(3):036101, 2005.
- [148] Jean-Yves Raty, François Gygi, and Giulia Galli. Growth of carbon nanotubes on metal nanoparticles: a microscopic mechanism from *ab initio* molecular dynamics simulations. *Physical review letters*, 95(9):096103, 2005.
- [149] Ali Rinaldi, Jean-Philippe Tessonnier, Manfred E Schuster, Raoul Blume, Frank Girgsdies, Qiang Zhang, Timo Jacob, Sharifah Bee Abd Hamid, Dang Sheng Su, and Robert Schlögl. Dissolved carbon controls the initial stages of nanocarbon growth. *Angewandte Chemie International Edition*, 50(14):3313–3317, 2011.
- [150] Randall L Vander Wal, Thomas M Ticich, and Valerie E Curtis. Substrate-support interactions in metal-catalyzed carbon nanofiber growth. *Carbon*, 39(15):2277–2289, 2001.
- [151] I Willems, Z Konya, J-F Colomer, G Van Tendeloo, N Nagaraju, A Fonseca, and JB Nagy. Control of the outer diameter of thin carbon nanotubes synthesized by catalytic decomposition of hydrocarbons. *Chemical Physics Letters*, 317(1-2):71–76, 2000.
- [152] Li Qingwen, Yan Hao, Cheng Yan, Zhang Jin, and Liu Zhongfan. A scalable cvd synthesis of high-purity single-walled carbon nanotubes with porous MgO as support material. *Journal of Materials Chemistry*, 12(4):1179–1183, 2002.

- 
- [153] Soo-Hwan Jeong, Hee-Young Hwang, Kun-Hong Lee, and Yongsoo Jeong. Template-based carbon nanotubes and their application to a field emitter. *Applied physics letters*, 78(14):2052–2054, 2001.
- [154] V Ivanov, JB Nagy, Ph Lambin, A Lucas, XB Zhang, XF Zhang, D Bernaerts, G Van Tendeloo, S Amelinckx, and J Van Landuyt. The study of carbon nanotubules produced by catalytic method. *Chemical Physics Letters*, 223(4):329–335, 1994.
- [155] Yunyu Wang, Zhiquan Luo, Bin Li, Paul S Ho, Zhen Yao, Li Shi, Eugene N Bryan, and Robert J Nemanich. Comparison study of catalyst nanoparticle formation and carbon nanotube growth: support effect. *Journal of applied physics*, 101(12):124310, 2007.
- [156] Simone Pisana, Alain Jungen, Can Zhang, Arthur M Blackburn, Renu Sharma, Felipe Cervantes-Sodi, Christoph Stampfer, Caterina Ducati, Andrea C Ferrari, Christofer Hierold, et al. Flying and crawling modes during surface-bound single wall carbon nanotube growth. *The Journal of Physical Chemistry C*, 111(46):17249–17253, 2007.
- [157] J-F Colomer, G Bister, I Willems, Z Konya, A Fonseca, JB Nagy, and G Van Tendeloo. Synthesis of single-wall carbon nanotubes by catalytic decomposition of hydrocarbons. *Chemical communications*, 0(14):1343–1344, 1999.
- [158] Delong He, Hao Li, Weilong Li, Paul Haghi-Ashtiani, Pascal Lejay, and Jinbo Bai. Growth of carbon nanotubes in six orthogonal directions on spherical alumina microparticles. *Carbon*, 49(7):2273–2286, 2011.
- [159] Placidus B Amama, Cary L Pint, Laura McJilton, Seung Min Kim, Eric A Stach, P Terry Murray, Robert H Hauge, and Benji Maruyama. Role of water in super growth of single-walled carbon nanotube carpets. *Nano letters*, 9(1):44–49, 2008.
- [160] Yoshikazu Homma, Yoshiro Kobayashi, Toshio Ogino, Daisuke Takagi, Roichi Ito, Yung Joon Jung, and Pulickel M Ajayan. Role of transition metal catalysts in single-walled carbon nanotube growth in chemical vapor deposition. *The Journal of Physical Chemistry B*, 107(44):12161–12164, 2003.
- [161] Goo-Hwan Jeong, Akira Yamazaki, Satoru Suzuki, Yoshihiro Kobayashi, and Yoshikazu Homma. Behavior of catalytic nanoparticles during chemical vapor deposition for carbon nanotube growth. *Chemical physics letters*, 422(1-3):83–88, 2006.
- [162] Ming Su, Yan Li, Benjamin Maynor, Alper Buldum, Jian Ping Lu, and Jie Liu. Lattice-oriented growth of single-walled carbon nanotubes. *The Journal of Physical Chemistry B*, 104(28):6505–6508, 2000.

## REFERENCES

---

- [163] Mireille Maret, Karine Hostache, Marie-Claude Schouler, Bernadette Marcus, Francine Roussel-Dherbey, Manfred Albrecht, and Patrice Gadelle. Oriented growth of single-walled carbon nanotubes on a MgO (001) surface. *Carbon*, 45(1):180–187, 2007.
- [164] Murray J Height, Jack B Howard, Jefferson W Tester, and John B Vander Sande. Carbon nanotube formation and growth via particle-particle interaction. *The Journal of Physical Chemistry B*, 109(25):12337–12346, 2005.
- [165] MingHui Kuang, Zhong Lin Wang, XD Bai, JD Guo, and EG Wang. Catalytically active nickel {110} surfaces in growth of carbon tubular structures. *Applied Physics Letters*, 76(10):1255–1257, 2000.
- [166] ZL Wang and ZC Kang. Growth of spiral carbon tubes by a mixed-valent oxide-catalytic carbonization process. *Philosophical Magazine B*, 74(1):51–69, 1996.
- [167] Kai Liu, Kaili Jiang, Chen Feng, Zhuo Chen, and Shoushan Fan. A growth mark method for studying growth mechanism of carbon nanotube arrays. *Carbon*, 43(14):2850–2856, 2005.
- [168] Anna Moisala, Albert G Nasibulin, and Esko I Kauppinen. The role of metal nanoparticles in the catalytic production of single-walled carbon nanotubes—a review. *Journal of Physics: condensed matter*, 15(42):S3011, 2003.
- [169] C Castro, M Pinault, S Coste-Leconte, D Porterat, Nedjma Bendiab, C Reynaud, and M Mayne-L’Hermite. Dynamics of catalyst particle formation and multi-walled carbon nanotube growth in aerosol-assisted catalytic chemical vapor deposition. *Carbon*, 48(13):3807–3816, 2010.
- [170] Qiang Zhang, Jia-Qi Huang, Meng-Qiang Zhao, Wei-Zhong Qian, and Fei Wei. Modulating the diameter of carbon nanotubes in array form via floating catalyst chemical vapor deposition. *Applied Physics A: Materials Science & Processing*, 94(4):853–860, 2009.
- [171] Celia Castro, Mathieu Pinault, Dominique Porterat, Cécile Reynaud, and Martine Mayne-L’Hermite. The role of hydrogen in the aerosol-assisted chemical vapor deposition process in producing thin and densely packed vertically aligned carbon nanotubes. *Carbon*, 61:585–594, 2013.
- [172] Kazunori Kuwana and Kozo Saito. Modeling ferrocene reactions and iron nanoparticle formation: Application to CVD synthesis of carbon nanotubes. *Proceedings of the combustion institute*, 31(2):1857–1864, 2007.
- [173] Devin Conroy, Anna Moisala, Silvana Cardoso, Alan Windle, and John Davidson. Carbon nanotube reactor: Ferrocene decomposition, iron particle growth, nanotube aggregation and scale-up. *Chemical Engineering Science*, 65(10):2965–2977, 2010.

- 
- [174] SI Futko, BG Shulitskii, VA Labunov, and EM Ermolaeva. Simulation of the kinetics of growth of iron nanoparticles in the process of chemical vapor deposition of hydrocarbons with injection of ferrocene for the synthesis of carbon-nanotube arrays. *Journal of Engineering Physics and Thermophysics*, 88(6):1432–1441, 2015.
- [175] Delong He, Hao Li, and Jinbo Bai. Experimental and numerical investigation of the position-dependent growth of carbon nanotube–alumina microparticle hybrid structures in a horizontal CVD reactor. *Carbon*, 49(15):5359–5372, 2011.
- [176] Vyacheslav O Khavrus, EMM Ibrahim, Albrecht Leonhardt, Silke Hampel, Steffen Oswald, Christine Täschner, and Bernd Büchner. Conditions of simultaneous growth and separation of single- and multiwalled carbon nanotubes. *The Journal of Physical Chemistry C*, 114(2):843–848, 2009.
- [177] Hongyuan Chen, Minghai Chen, Yongyi Zhang, and Qingwen Li. Rational control on floating catalysts for the growth of carbon nanotube assemblies: From vertically aligned carbon nanotube arrays to carbon nanotube films. *Applied Surface Science*, 353:651–661, 2015.
- [178] R. W. Weeks and W. W. Duley. Aerosol-particle sizes from light emission during excitation by TEA CO<sub>2</sub> laser pulses. *Journal of Applied Physics*, 45(10):4661–4662, 1974.
- [179] Alan C Eckbreth. Effects of laser-modulated particulate incandescence on raman scattering diagnostics. *Journal of Applied Physics*, 48(11):4473–4479, 1977.
- [180] P Roth and AV Filippov. *In-situ* ultrafine particle sizing by a combination of pulsed laser heatup and particle thermal emission. *Journal of aerosol science*, 27(1):95–104, 1996.
- [181] AV Filippov, MW Markus, and Paul Roth. *In-situ* characterization of ultrafine particles by laser-induced incandescence: sizing and particle structure determination. *Journal of Aerosol Science*, 30(1):71–87, 1999.
- [182] Randy L Vander Wal and Mun Y Choi. Pulsed laser heating of soot: morphological changes. *Carbon*, 37(2):231–239, 1999.
- [183] Boman Axelsson, Robert Collin, and Per-Erik Bengtsson. Laser-induced incandescence for soot particle size measurements in premixed flat flames. *Applied Optics*, 39(21):3683–3690, 2000.
- [184] Henrik Bladh and P-E Bengtsson. Characteristics of laser-induced incandescence from soot in studies of a time-dependent heat-and mass-transfer model. *Applied physics b*, 78(2):241–248, 2004.

## REFERENCES

---

- [185] DR Snelling, KA Thomson, F Liu, and GJ Smallwood. Comparison of LII derived soot temperature measurements with LII model predictions for soot in a laminar diffusion flame. *Applied Physics B*, 96(4):657–669, 2009.
- [186] Hope A Michelsen, Peter O Witze, David Kayes, and Simone Hochgreb. Time-resolved laser-induced incandescence of soot: the influence of experimental factors and microphysical mechanisms. *Applied optics*, 42(27):5577–5590, 2003.
- [187] Hope A Michelsen. Understanding and predicting the temporal response of laser-induced incandescence from carbonaceous particles. *The Journal of chemical physics*, 118(15):7012–7045, 2003.
- [188] David R Snelling, Gregory J Smallwood, Ömer L Gülder, William D Bachalo, and Subramanian Sankar. Soot volume fraction characterization using the laser-induced incandescence detection method. In *Proceedings of the 10th International Symposium on Applications of Laser Techniques to Fluid Mechanics, Lisbon*, 2000.
- [189] Stefan Dankers, Alfred Leipertz, Stefan Will, Jorg Arndt, Karl Vogel, Stephan Schraml, and Annegret Hemm. *In-situ* measurement of primary particle sizes during carbon black production. *Chemical engineering & technology*, 26(9):966–969, 2003.
- [190] Randy L Vander Wal, Gordon M Berger, Thomas M Ticich, and Premal D Patel. Application of laser-induced incandescence to the detection of carbon nanotubes and carbon nanofibers. *Applied optics*, 41(27):5678–5690, 2002.
- [191] David R Snelling, Gregory J Smallwood, Robert A Sawchuk, W Stuart Neill, Daniel Gareau, Daniel J Clavel, Wallace L Chippior, Fengshan Liu, Ömer L Gülder, and William D Bachalo. *In-situ* real-time characterization of particulate emissions from a diesel engine exhaust by laser-induced incandescence. Technical report, SAE Technical Paper, 2000.
- [192] David R Snelling, Gregory J Smallwood, Fengshan Liu, Ömer L Gülder, and William D Bachalo. A calibration-independent laser-induced incandescence technique for soot measurement by detecting absolute light intensity. *Applied optics*, 44(31):6773–6785, 2005.
- [193] M. Cau, N. Dorval, B. Attal-Trétout, J.-L. Cochon, A. Foutel-Richard, A. Loiseau, V. Krüger, M. Tsurikov, and C. D. Scott. Formation of carbon nanotubes: *In situ* optical analysis using laser-induced incandescence and laser-induced fluorescence. *Phys. Rev. B*, 81:165416, Apr 2010.
- [194] S Yatom, J Bak, A Khrabryi, and Y Raitsts. Detection of nanoparticles in carbon arc discharge with laser-induced incandescence. *Carbon*, 117:154–162, 2017.

- 
- [195] Boris F Kock, Th Eckhardt, and Paul Roth. In-cylinder sizing of diesel particles by time-resolved laser-induced incandescence (TR-LII). *Proceedings of the Combustion Institute*, 29(2):2775–2782, 2002.
- [196] H Bockhorn, H Geitlinger, B Jungfleisch, Th Lehre, A Schön, Th Streibel, and R Suntz. Progress in characterization of soot formation by optical methods. *Physical Chemistry Chemical Physics*, 4(15):3780–3793, 2002.
- [197] Fengshan Liu, Gregory J Smallwood, and David R Snelling. Effects of primary particle diameter and aggregate size distribution on the temperature of soot particles heated by pulsed lasers. *Journal of Quantitative Spectroscopy and Radiative Transfer*, 93(1-3):301–312, 2005.
- [198] Evgeniy Valer’evich Gurentsov and Aleksandr Viktorovich Eremin. Size measurement of carbon and iron nanoparticles by laser induced incandescence. *High Temperature*, 49(5):667, 2011.
- [199] A Eremin, E Gurentsov, E Popova, and K Priemchenko. Size dependence of complex refractive index function of growing nanoparticles. *Applied Physics B*, 104(2):285–295, 2011.
- [200] HA Michelsen, MA Linne, Boris F Kock, Max Hofmann, B Tribalet, and C Schulz. Modeling laser-induced incandescence of soot: enthalpy changes during sublimation, conduction, and oxidation. *Applied Physics B*, 93(2-3):645, 2008.
- [201] Fengshan Liu, KJ Daun, David R Snelling, and Gregory J Smallwood. Heat conduction from a spherical nano-particle: status of modeling heat conduction in laser-induced incandescence. *Applied physics B*, 83(3):355–382, 2006.
- [202] Boris F Kock, Can Kayan, Jörg Knipping, Hans R Orthner, and Paul Roth. Comparison of LII and TEM sizing during synthesis of iron particle chains. *Proceedings of the Combustion Institute*, 30(1):1689–1697, 2005.
- [203] Hope A Michelsen, Fengshan Liu, Boris F Kock, Hendrik Bladh, Andrei Boïarciuc, Marcus Charwath, Thomas Dreier, Redjem Hadeif, Max Hofmann, Joerg Reimann, et al. Modeling laser-induced incandescence of soot: a summary and comparison of LII models. *Applied physics B*, 87(3):503–521, 2007.
- [204] HR Leider, OH Krikorian, and DA Young. Thermodynamic properties of carbon up to the critical point. *Carbon*, 11(5):555–563, 1973.
- [205] Francesco Cignoli, Silvana De Iuliis, Vittorio Manta, and Giorgio Zizak. Two-dimensional two-wavelength emission technique for soot diagnostics. *Applied Optics*, 40(30):5370–5378, 2001.
- [206] S De Iuliis, F Migliorini, F Cignoli, and G Zizak. Peak soot temperature in laser-induced incandescence measurements. *Applied Physics B*, 83(3):397, 2006.

## REFERENCES

---

- [207] Thilo Lehre, Beate Jungfleisch, Rainer Suntz, and Henning Bockhorn. Size distributions of nanoscaled particles and gas temperatures from time-resolved laser-induced-incandescence measurements. *Applied optics*, 42(12):2021–2030, 2003.
- [208] David R Snelling, Fengshan Liu, Gregory J Smallwood, and Ömer L Gülder. Determination of the soot absorption function and thermal accommodation coefficient using low-fluence LII in a laminar coflow ethylene diffusion flame. *Combustion and Flame*, 136(1-2):180–190, 2004.
- [209] TC Fang, CM Megaridis, WA Sowa, and GS Samuelsen. Soot morphology in a liquid-fueled, swirl-stabilized combustor. *Combustion and flame*, 112(3):312–328, 1998.
- [210] MM Maricq. Size and charge of soot particles in rich premixed ethylene flames. *Combustion and Flame*, 137(3):340–350, 2004.
- [211] Donald W Marquardt. An algorithm for least-squares estimation of nonlinear parameters. *Journal of the society for Industrial and Applied Mathematics*, 11(2):431–441, 1963.
- [212] Amelia Barreiro, Silke Hampel, Mark H Rummeli, Christian Kramberger, Alexander Grüneis, Kati Biedermann, Albrecht Leonhardt, Thomas Gemming, Bernd Büchner, Adrian Bachtold, et al. Thermal decomposition of ferrocene as a method for production of single-walled carbon nanotubes without additional carbon sources. *The Journal of Physical Chemistry B*, 110(42):20973–20977, 2006.
- [213] Yang Ma, Anthony B Dichiara, Delong He, Laurent Zimmer, and Jinbo Bai. Control of product nature and morphology by adjusting the hydrogen content in a continuous chemical vapor deposition process for carbon nanotube synthesis. *Carbon*, 107:171–179, 2016.
- [214] Johannes Vanpaemel, Marleen H van der Veen, Daire J Cott, Masahito Sugiura, Inge Asselberghs, Stefan De Gendt, and Philippe M Vereecken. Dual role of hydrogen in low temperature plasma enhanced carbon nanotube growth. *The Journal of Physical Chemistry C*, 119(32):18293–18302, 2015.
- [215] BC Satishkumar, A Govindaraj, Rahul Sen, and CNR Rao. Single-walled nanotubes by the pyrolysis of acetylene-organometallic mixtures. *Chemical Physics Letters*, 293(1):47–52, 1998.
- [216] Rong Xiang, Erik Einarsson, Jun Okawa, Yuhei Miyauchi, and Shigeo Maruyama. Acetylene-accelerated alcohol catalytic chemical vapor deposition growth of vertically aligned single-walled carbon nanotubes. *The Journal of Physical Chemistry C*, 113(18):7511–7515, 2009.

- [217] Delong He and Jinbo Bai. Acetylene-enhanced growth of carbon nanotubes on ceramic microparticles for multi-scale hybrid structures. *Chemical Vapor Deposition*, 17(4-6):98–106, 2011.
- [218] Yang Ma. *Study on the formation and catalytic activity of nanoparticles in early stages of carbon nanotubes growth under aerosol-assisted chemical vapor deposition*. PhD thesis, Université Paris-Saclay, 2016.
- [219] MS Dresselhaus, A Jorio, and R Saito. Characterizing graphene, graphite, and carbon nanotubes by raman spectroscopy. *Annu. Rev. Condens. Matter Phys.*, 1(1):89–108, 2010.
- [220] Dong-Hau Kuo and Mei-Yun Su. The effects of hydrogen and temperature on the growth and microstructure of carbon nanotubes obtained by the  $\text{Fe}(\text{CO})_5$  gas-phase-catalytic chemical vapor deposition. *Surface and Coatings Technology*, 201(22-23):9172–9178, 2007.
- [221] Abraham Savitzky and Marcel JE Golay. Smoothing and differentiation of data by simplified least squares procedures. *Analytical chemistry*, 36(8):1627–1639, 1964.
- [222] R Ryser, T Gerber, and T Dreier. Soot particle sizing during high-pressure diesel spray combustion via time-resolved laser-induced incandescence. *Combustion and Flame*, 156(1):120–129, 2009.
- [223] EV Gurentsov, AV Eremin, P Roth, and R Starke. Formation of iron-carbon nanoparticles behind shock waves. *Kinetics and catalysis*, 46(3):309–318, 2005.
- [224] SC Graham, JB Homer, and JJJ Rosenfield. The formation and coagulation of soot aerosols generated by the pyrolysis of aromatic hydrocarbons. *Proc. R. Soc. Lond. A*, 344(1637):259–285, 1975.
- [225] A Eremin, E Gurentsov, E Mikheyeva, and K Priemchenko. Experimental study of carbon and iron nanoparticle vaporisation under pulse laser heating. *Applied Physics B*, 112(3):421–432, 2013.
- [226] Gregory D Yoder, Prasoon K Diwakar, and David W Hahn. Assessment of soot particle vaporization effects during laser-induced incandescence with time-resolved light scattering. *Applied optics*, 44(20):4211–4219, 2005.
- [227] Henrik Bladh, Jonathan Johnsson, Jenny Rissler, H Abdulhamid, N-E Olofsson, Mehri Sanati, Joakim Pagels, and P-E Bengtsson. Influence of soot particle aggregation on time-resolved laser-induced incandescence signals. *Applied Physics B*, 104(2):331–341, 2011.
- [228] B. Bougie, L.C. Ganippa, A.P. van Vliet, W.L. Meerts, N.J. Dam, and J.J. ter Meulen. Laser-induced incandescence particle size measurements in a heavy-duty diesel engine. *Combustion and Flame*, 145(3):635 – 637, 2006.

## REFERENCES

---

- [229] KJ Daun. Thermal accommodation coefficients between polyatomic gas molecules and soot in laser-induced incandescence experiments. *International Journal of Heat and Mass Transfer*, 52(21-22):5081–5089, 2009.
- [230] Tamás Turányi. Sensitivity analysis of complex kinetic systems. tools and applications. *Journal of mathematical chemistry*, 5(3):203–248, 1990.
- [231] Alison S Tomlin. The use of global uncertainty methods for the evaluation of combustion mechanisms. *Reliability Engineering & System Safety*, 91(10-11):1219–1231, 2006.
- [232] Alison S Tomlin and Tamás Turányi. Investigation and improvement of reaction mechanisms using sensitivity analysis and optimization. In *Cleaner Combustion*, pages 411–445. Springer, 2013.
- [233] Ilya M Sobol. Sensitivity estimates for nonlinear mathematical models. *Mathematical modelling and computational experiments*, 1(4):407–414, 1993.
- [234] Chihiro Kaito. Coalescence growth of smoke particles prepared by a gas-evaporation technique. *Japanese Journal of Applied Physics*, 17(4):601, 1978.
- [235] Richard H Heist, Junaid Ahmed, and Muhammed Janjua. Effects of background gases on the homogeneous nucleation of vapors. 2. *J. Phys. Chem.*, 99(1):375–383, 1995.
- [236] S Braun, F Römer, and T Kraska. Influence of the carrier gas molar mass on the particle formation in a vapor phase. *J. Chem. Phys.*, 131(6):064308, 2009.
- [237] Jean-Charles Arnault, David Eon, Clément Hébert, Davy Carole, Franck Omnes, and Etienne Gheeraert. Etching mechanism of diamond by ni nanoparticles for fabrication of nanopores. *Carbon*, 59:448–456, 2013.
- [238] Hao Zhang, Gaoping Cao, Zhiyong Wang, Yusheng Yang, Zujin Shi, and Zhenan Gu. Influence of ethylene and hydrogen flow rates on the wall number, crystallinity, and length of millimeter-long carbon nanotube array. *The Journal of Physical Chemistry C*, 112(33):12706–12709, 2008.
- [239] Xiulan Zhao, Yu Liu, Rongli Cui, and Yan Li. Nucleation of copper nanoparticles on quartz as catalysts to grow single-walled carbon nanotube arrays. *Carbon*, 110:390–395, 2016.
- [240] Chenguang Lu and Jie Liu. Controlling the diameter of carbon nanotubes in chemical vapor deposition method by carbon feeding. *The Journal of Physical Chemistry B*, 110(41):20254–20257, 2006.
- [241] BR Elliott, JJ Host, VP Dravid, MH Teng, and JH Hwang. A descriptive model linking possible formation mechanisms for graphite-encapsulated nanocrystals to processing parameters. *Journal of materials research*, 12(12):3328–3344, 1997.

**Titre :** Détection *quasi-in situ* de nanoparticules par incandescence induite par laser pendant la synthèse par dépôt chimique en phase vapeur de nanotubes de carbone

**Mots clés :** Nanoparticules, Détection *quasi-in situ*, Incandescence induite par laser, Nanotubes de carbone

**Résumé :** Ce travail contribue à la *quasi-in-situ* détection des nanoparticules par la technique d'incandescence induite par laser (LII) pendant le dépôt chimique en phase vapeur avec catalyseur flottant (FCCVD) de nanotubes de carbone.

Premièrement, la microscopie électronique en transmission (MET) à haute résolution était utilisé pour caractériser la nature et la taille des nanoparticules. Le signal théorique de LII a été simulé en considérant la densité des nanoparticules, la capacité thermique et la distribution de taille, etc. La sensibilité et l'incertitude concrètes des paramètres clés sur la taille évaluée des particules pour ce modèle ont été estimées. Le modèle LII a été validé par la comparaison des résultats évalués avec ceux obtenus par la MET. Ensuite, la technique mature LII combinée avec MET a été appliquée pour étudier l'évolution des nanoparticules dans la phase gazeuse le long de l'axe du réacteur. L'influence de la température, de la concentration de ferrocène, de la source de carbone et de la proportion hydrogène sur la taille des nanoparticules a également été démontrée. En-

fin, les rôles des nanoparticules dans la phase gazeuse au cours du processus de synthèse des NTC ont été discutés en corrélant les informations sur l'évolution axiale des nanoparticules et la morphologie des NTC synthétisés sur le substrat le long de l'axe du réacteur. Un modèle basé sur la thermodynamique de la nucléation des nanoparticules a été proposé pour décrire le processus de formation des nanoparticules au cours du processus DCVCF. Il est constaté que les nanoparticules as-formé en phase gazeuse présentent des structures coeur-coquille avec un noyau de  $\alpha$ -Fe et la coque de carbone. Ainsi, les nanoparticules de fer en phase gazeuse ne pourraient pas contribuer à la croissance de NTC sur le substrat à cause de l'encapsulation de carbone. En même temps, la taille des nanoparticules évaluée par LII est en bon accord avec celle-ci déterminée par MET. Cette étude, montrant les relations potentielles entre les nanoparticules flottantes et les NTCs sur le substrat, révèle une perspective importante de l'application de LII pour comprendre et améliorer le processus DCVCF.

**Title :** *Quasi-in-situ* detection of nanoparticles by laser-induced incandescence during chemical vapor deposition synthesis of carbon nanotubes

**Keywords :** Nanoparticles, *Quasi-in-situ* detection, Laser induced incandescence, Carbon nanotubes

**Abstract :** This work contributes to the *quasi-in-situ* detection of nanoparticles by laser induced incandescence (LII) technique during the floating catalytic chemical vapor deposition (FCCVD) synthesis of Carbon nanotubes.

First, high resolution transmission electron microscopy (TEM) was used to characterize the nanoparticle nature and size. The theoretical LII signal was simulated by considering the nanoparticle density, heat capacity and size distribution, etc. A detailed sensitivity and uncertainty of the key parameters on the evaluated particle size for this model was estimated. The LII model was validated by a comparison of the evaluated results with the ones obtained by TEM measurements. Then, the developed LII technique combined with TEM was applied to investigate the evolution of nanoparticles in the gas phase along the reactor axis. The influence of the temperature, ferrocene concentration, carbon source and hydrogen ratio on the nanoparticle size was also demonstrated. Fi-

nally, the roles of nanoparticles in the gas phase during CNT synthesis process were discussed by correlating information on the axial nanoparticle evolution and the morphology of CNTs synthesized on the substrate along the reactor axis. And a model based on the thermodynamics of the nanoparticle nucleation was proposed to describe the nanoparticle formation process during the FCCVD process. It is found that the as-formed nanoparticles in the gas phase exhibit core-shell structures with an  $\alpha$ -Fe core and a carbon shell. Hence iron nanoparticles in the gas phase could not contribute to the CNT growth on the substrate because of the carbon encapsulation. Meanwhile the evaluated size of nanoparticles by LII is in good agreement with the TEM determined one. This study, showing potential relations between the floating nanoparticles and the CNTs on the substrate, reveals the important LII application prospect to understand and to improve the FCCVD process.

